



## 저작자표시-비영리-변경금지 2.0 대한민국

이용자는 아래의 조건을 따르는 경우에 한하여 자유롭게

- 이 저작물을 복제, 배포, 전송, 전시, 공연 및 방송할 수 있습니다.

다음과 같은 조건을 따라야 합니다:



저작자표시. 귀하는 원저작자를 표시하여야 합니다.



비영리. 귀하는 이 저작물을 영리 목적으로 이용할 수 없습니다.



변경금지. 귀하는 이 저작물을 개작, 변형 또는 가공할 수 없습니다.

- 귀하는, 이 저작물의 재이용이나 배포의 경우, 이 저작물에 적용된 이용허락조건을 명확하게 나타내어야 합니다.
- 저작권자로부터 별도의 허가를 받으면 이러한 조건들은 적용되지 않습니다.

저작권법에 따른 이용자의 권리는 위의 내용에 의하여 영향을 받지 않습니다.

이것은 [이용허락규약\(Legal Code\)](#)을 이해하기 쉽게 요약한 것입니다.

[Disclaimer](#)

공학박사학위논문

의료용 바늘 조향을 위한 비등방성  
패터닝을 활용한 가변강성 메커니즘

Variable Stiffness Mechanism using Anisotropic  
Patterning for Needle Steering

2019 년 2 월

서울대학교 대학원

기계항공공학부

김 종 우

## **Abstract**

# **Variable Stiffness Mechanism using Anisotropic Patterning for Needle Steering**

Jongwoo Kim

Department of Mechanical and Aerospace Engineering

The Graduate School

Seoul National University

Robot-assisted surgeries enabled more accurate operations and less unreachable areas than conventional methods by human surgeons. Especially, from the advent of da Vinci robots, minimally invasive surgery (MIS) is becoming more popular as it has many advantages compared to traditional open surgery, such as smaller incision and faster recovery time. In MIS, continuum robots are widely used thanks to their scalability and compactness. However, the smaller the space, the more difficult it is to control the motion of the continuum robots due to smaller moment arm and the lack of adequate micro-actuators. Variable stiffness can be utilized to provide motion control for the continuum robots under interactions with nearby tissues in anatomically confined space.

I proposed a continuously variable stiffness mechanism for scalable continuum robots. The mechanism consists of multiple coaxial nitinol or stainless steel tubes, and each tube has an anisotropic distribution of flexural stiffness created by non-uniform through-hole patterning. The stiffness of the mechanism is varied by relative rotation and translation among the tubes, resulting in flexural stiffness

difference up to 7.2 times or more in the direction of load. Its flexural stiffnesses along principal axes are independently controlled by the suggested counter rotation algorithm. The stiffness change is validated through analytical modeling, FEM simulation, and the experiments. Thanks to its physically embodied intelligence, the mechanism has a simple scalable structure and the response time is immediate. Additionally, the optimization and the parametric study for the patterns are studied to design the degree and the range of variable stiffness. Also, the bending and twist buckling conditions were analyzed. The pattern is able to be customized according to required stiffness while satisfying the constraints to avoid buckling.

I applied this variable stiffness mechanism to control the stiffness of the steerable needle. Varying the stiffness grants the additional degree of freedom to control needle's trajectory. The kinematic bi-cycle nonholonomic model was built to determine the curvature of the needle's trajectory according to the needle's rotational configuration. Finally, the stiffness-controlled steerable needle increases safety while limiting the needle's insertion and rotation speed, and reduces unreachable area as well as invasiveness compared to current steerable needles. Additionally, the mechanism has hollow space that can provide a conduit through which to deliver a wide variety of therapies, e.g. drugs, radioactive seeds, and thermal ablation. The proposed needle can be applied for prostate brachytherapy and liver/lung tumor ablation and is expected to be used in various continuum needlescopic surgical instruments.

**Keywords:** Variable Stiffness Mechanism, Anisotropic Patterning, Steerable Needle, Minimally Invasive Surgery, Physically Embodied Intelligence, Medical Robots and System

**Student Number:** 2013-20659

# Contents

<b>Abstract</b>	<b>i</b>
<b>Contents</b>	<b>iii</b>
<b>List of Tables</b>	<b>vi</b>
<b>List of Figures</b>	<b>vii</b>
<b>Nomenclature</b>	<b>xii</b>

<b>Chapter 1 Introduction</b>	<b>1</b>
1.1 Motivation	1
1.2 Research Objectives and Contributions	3
1.3 Research Overview	4

<b>Chapter 2 Continuously Variable Stiffness Mechanism using Asymmetric Patterns on Coaxial Tubes</b>	<b>6</b>
2.1 Design and Modeling of the Mechanism	6
2.1.1 The Concept and the Design of the Mechanism	6
2.1.2 Analytic Modeling of the stiffness of the Mechanism	14
2.1.3 Decoupling $I_{xx}$ and $I_{xy}$	21
2.1.4 Pattern Design to Customize the Stiffness Range	22
2.2 Finite Element Method Simulation	26
2.3 Fabrication and 3-point Bending Experiment	29
2.3.1 Ultra Violet Laser Machining	29
2.3.2 Three-point Bending Test	32
2.3.3 Comparison of the Flexural Stiffness Change	35

2.3.4	Demonstration of Continuously Variable Stiffness .	37
2.4	The Feasibility of Stiffness-Controlled Steerable Needle	39

## **Chapter 3 Parametric Study of the Patterns for Variable Stiffness .....44**

3.1	The Topology Optimization of the Pattern .....	44
3.2	Design Parameters of Pattern.....	52
3.3	The Variation of Flexural Stiffness.....	54
3.3.1	The Analytic Modeling for Flexural Stiffness .....	54
3.3.2	The FEM Simulation for Flexural Stiffness .....	55
3.4	Buckling Analysis.....	58
3.4.1	Mechanics Model of the Steerable Needle .....	58
3.4.2	Bending and Torsional Buckling Analysis .....	61
3.5	Experimental Verification.....	66
3.6	Pattern Optimization Process according to Application ...	71

## **Chapter 4 Stiffness-controlled Steerable Needle .....73**

4.1	The Current Steerable Needle Mechanisms .....	73
4.2	The Mechanism of Stiffness-Controlled Steerable Needle	76
4.3	Steerable Needle Control.....	79
4.3.1	The Radius of Curvature of Needle's Trajectory.....	79
4.3.2	Bi-cycle Nonholonomic Model for Steerable Needle	79
4.4	The Customization on Stiffness and the Range of Variable Stiffness.....	89
4.5	Stiffness-controlled Steerable Needle's Applications .....	95

<b>Chapter 5 Discussion and Conclusion .....</b>	<b>98</b>
<b>Bibliography .....</b>	<b>102</b>

## List of Tables

Table 2.1	The specification of the inner and outer tubes .....	8
Table 2.2	The flexural stiffness change and its ratio (times) comparison among the analytic modeling, the FEM simulation, and the three point bending experiment .....	36
Table 3.1	The topology optimization cases for variable stiffness.....	47
Table 3.2	The optimized patterns for Type A and B .....	51
Table 3.3	The pattern design parameters for the experiment.....	67
Table 3.4	The comparison of three point bending test between the FEM simulation and the experiment.....	70
Table 4.1	The coefficients for bi-cycle nonholonomic kinematic model ...	87
Table 4.2	The comparison of stiffness-controlled needle with other steering methods.....	97



## List of Figures

- Figure 2.1 Variable stiffness is able to assist motion control of continuum robots in anatomically confined space. Under the same external force,  $F$ , the deflection of the given structure increases as the stiffness decreases as  $EI_a > EI_b > EI_c$ ..... 9
- Figure 2.2 The principles and the design parameters ( $l_1, l_2, m_1, m_2, \theta, n$ ) of the pattern for variable stiffness mechanism. The inner and outer tubes are assembled coaxially, and each tube rotates and translates independently. The cross section view demonstrates how the through-hole patterns are engraved on the tubes of type A ( $60^\circ$  per half) and B ( $120^\circ$  per half). ..... 10
- Figure 2.3 The flexural stiffness change according to translational configuration of the inner and outer tubes. The black parts stand for the patterned region while the grey parts stand for the unpatterned region. a) In view of the longitudinal direction, when the patterned parts of the outer tube overlap with the unpatterned of the inner tube. The structure is relatively rigid. b) On the other hand, when the patterned parts of the outer tube overlap the patterned of the inner. The structure is relatively flexible. ... 12
- Figure 2.4 a) The cross section of the single patterned tube at the initial state (left) and rotated by  $\omega$  from the initial state (right) where the dashed represents the patterned and the non-dashed represents the unpatterned. The relative rotation configuration of the inner and outer tubes results in the continuously variable stiffness of the structure. The inner and outer tubes are assembled coaxially and each tube rotates independently.  $\omega_1$  and  $\omega_2$  are the rotational angle for inner and outer tube, respectively, and  $(\omega_1, \omega_2)$  is an element of  $\{(0^\circ, 0^\circ), (60^\circ, 0^\circ), (90^\circ, 0^\circ), (90^\circ, 90^\circ)\}$  from the left for b) Type A and c) Type B..... 13
- Figure 2.5 a) The Mohr's circle (blue) for the inner tube for the rotated angle,  $\omega_1$ ,

	b) the Mohr's circle (green) for the outer tube for the rotated angle, $\omega_2$ . .....	19
Figure 2.6	As the inner and outer tubes rotate, the graph describes the change in the flexural stiffness ( $K_{xx}$ ) ratio of a) Type A and b) Type B structure according to the analytic modeling.....	20
Figure 2.7	The flexural stiffness ratio of the single patterned tube according to the central angle for the patterned area, $\theta_p$ . The stiffness ratio is the maximum when $\theta_p = 128.9^\circ$ .....	25
Figure 2.8	Three-point bending test by a) the diagram, b) the experimental set-ups using Instron 5900 series, and c) FEM simulation results of three-point bending test by Abaqus 6.14.....	27
Figure 2.9	The FEM simulation results of Type A (upper) and Type B (lower) structure when $(\omega_1, \omega_2) \in \{(0^\circ, 0^\circ), (60^\circ, 0^\circ), (90^\circ, 0^\circ), (90^\circ, 90^\circ)\}$ . .....	28
Figure 2.10	. a) The UV laser machining set-ups, b) the microscopic image of the engraved tube surface, c) the laser patterned nitinol tube of Type A and d) Type B .....	31
Figure 2.11	The load-deflection plots from three-point bending experiment. The plots of the first column (the inner tube) and the second column (the outer tube) compare the flexural stiffnesses between the rotated angles of $0^\circ$ and $90^\circ$ . The third column plots compare the stiffness of the structure where $(\omega_1, \omega_2) \in \{(0^\circ, 0^\circ), (60^\circ, 0^\circ), (90^\circ, 0^\circ), (90^\circ, 90^\circ)\}$ . .....	34
Figure 2.12	The cantilever load test was performed for the variable stiffness structure. The tip position demonstrated continuous deflections while both the inner and outer tubes had rotational angles varying with continuous sinusoidal wave. ....	38
Figure 2.13	a) The stiffness-controlled steerable needle consists of the bevel-tip inner tube and the non-uniform patterned outer tube, b) the experimental	

	set-ups for the insertion of the stiffness-controlled steerable needle. The comparison of the needle's distal tip position at c) $(\omega_1, \omega_2) = (0^\circ, 90^\circ)$ and d) $(0^\circ, 0^\circ)$ . ....	42
Figure 2.14	The workspace comparison between a) the needle with constant insertion speed and b) the stiffness-controlled needle with the constant insertion speed. c) and d) demonstrate the cross section of a) and b), respectively. ....	43
Figure 3.1	The material-properties distribution of the topology optimized pattern for various cases of Table 3.1. The optimized pattern has the shape of rectangular shape along the longitudinal direction. ....	48
Figure 3.2	a) The cross section of the patterned tubes of Type A and Type B, b) the optimized patterns according to the constraints where $\beta \in \{0.2, 0.4, 0.6, 0.8\}$ . The white part stands for the non-patterned section while the black part stands for the patterned section. ....	50
Figure 3.3	The change of $I_{yy}/I_{xx}$ ratio according to $\theta_1$ and $\theta_2$ values when $\beta = 0.6$ . ....	51
Figure 3.4	The design parameters for the pattern of the variable stiffness mechanism. ....	53
Figure 3.5	a) From the left, the deflection map along x direction, the deflection map along y direction, and the stiffness ratio $I_{xx}/I_{yy}$ map according to the design parameters, $L_h$ and $\theta_h$ , b) The stiffness ratio $I_{xx}/I_{yy}$ according to $L_h$ when $\theta_h \in \{30^\circ, 60^\circ, 90^\circ, 120^\circ\}$ from the left.. ....	57
Figure 3.6	a) The mechanics of steerable needle inserting into elastic medium, b) the free body diagram at the distal tip [50].....	60
Figure 3.7	The buckling of the patterned tube caused by a) twist moment ( $M_z$ ) and b) bending moment ( $M_y$ ) .....	63
Figure 3.8	The map of $M_y$ (bending moment) and $M_z$ (twist moment) thresholds to avoid buckling according to $\theta_h$ and $L_h$ for A) the nitinol inner tube, B)	

	the nitinol outer tube, and C) the stainless steel inner tube. ....	64
Figure 3.9	The stable and unstable area of the design parameters, $\theta_h$ and $L_h$ , according to the given bending/twist moment values for a) the nitinol inner tube, b) the nitinol outer tube, and c) the stainless steel inner tube. ....	65
Figure 3.10	a) The picosecond UV laser machining system to manufacture the patterned tubes, b) the glass jig installation for precise alignment during the manufacturing process of the tubes with diameters of 1 mm or less. ....	68
Figure 3.11	The patterned tubes by picosecond UV laser machining according to design parameters, $\theta_h$ and $L_h$ .....	69
Figure 3.12	a) The experiment on three point bending test using Instron 5900 series and b) the FEM simulation of three point bending test using Abaqus 6.14. ....	70
Figure 3.13	The flow chart to determine pattern design parameters for the variable stiffness mechanism according to the target application and the constraints. ....	72
Figure 4.1	The outer tube with the bevel-tip (upper) and the inner tube with the patterns (lower) of the steerable needle. ....	78
Figure 4.2	The diagram of the bi-cycle nonholonomic modeling for the trajectory of the stiffness-controlled steerable needle, derived from [1] ....	81
Figure 4.3	The insertion experiment set-ups for the stiffness-controlled steerable needle.....	85
Figure 4.4	The results of the stiffness-controlled steerable needle's insertion with variable stiffness. The rotational configuration of the inner tube is 0°, 30°, 60°, and 90° to vary the needle's flexural stiffness along its bending direction .....	87
Figure 4.5	The needle's trajectory from the bi-cycle nonholonomic model and the standard deviation bar of the experimental results when $\theta_R$ is a) 0°, b)	

	30°, c) 60°, and d) 90° .....	88
Figure 4.6	The linearly fitting graph between the needle's flexural stiffness and the reciprocal of the square of the the needle trajectory curvature...	93
Figure 4.7	The relationship between the inner tube rotation, $\theta_i$ , and the curvature of the needle's trajectory, $\kappa$ .....	94
Figure 4.8	The obstacle avoiding test using continuously stiffness-controlled steerable needle. The needle started from the green circle and approached the yellow circle while avoiding red regions by varying the curvature of the needle's trajectory.....	97

## Nomenclature

$K$	Flexural stiffness
$I$	Second moment of inertia
$E$	Young's modulus
$E_p$	“Effective” Young's modulus of the patterned section
$E_u$	“Effective” Young's modulus of the unpatterned section
$d_i$	The diameter of the inner tube
$d_o$	The diameter of the outer tube
$r_i$	The radius of the inner tube
$r_o$	The radius of the outer tube
$\omega_1$	The rotated angle of the inner tube
$\omega_2$	The rotated angle of the outer tube
$n$	Repeated numbered of the unit pattern
$V$	The volume of the tubular structure
$\theta_h$	The central angle of the pattern
$\theta_n$	The central angle of the unpatterned section
$L_s$	The length of the segment
$L_h$	The length of the pattern
$L_o$	The length of the offset between the patterns
$\beta$	The coefficient of the minimum stiffness constraint
$U_B$	The pure needle bending energy

$U_P$	The bending energy due to axial load
$U_c$	The energy due to compression of the elastic medium at tip
$U_T$	The energy due to interaction of the elastic medium along the shaft
$W_Q$	The work done by transverse tip load
$W_P$	The work done by axial tip load
$W_R$	The work done to rupture the elastic medium
$G_c$	Rupture toughness
$C_{10}$	The tissue's nonlinear material property
$\mu$	The coefficient of friction
$a$	The amount of tear
$\alpha$	The angle of the bevel tip
$M_y$	The bending moment
$M_z$	The twist moment
$u_1$	The needle insertion speed
$u_2$	The needle rotation speed
$\kappa$	The curvature of the needle's trajectory
$V_1$	The spatial velocity of the pure needle insertion
$V_2$	The spatial velocity of the pure needle rotation
$l_1$	The length between the centers of the two wheels
$l_2$	The length between the needle tip and the first wheel's center
$n(t)$	The position vector of the needle tip according to time $t$

# Chapter 1 Introduction

## 1.1 Motivation

Minimally invasive surgery (MIS) is becoming more popular as it has several advantages compared to traditional open surgery, such as smaller incision and faster recovery time. In MIS, continuum robots are widely used thanks to their scalability and compactness. However, the smaller the space, the more difficult it is to control the motion of the continuum robots due to smaller moment arm and the lack of adequate micro-actuators. Variable stiffness can be utilized to provide motion control for the continuum robots under interactions with nearby tissues in anatomically confined space. In Fig. 2.1, under the same load, the deflection of the same-length red beam increases as flexural stiffness decreases like  $EI_a > EI_b > EI_c$ .

Without activating any actuators or additional load, the motion of the beam is changed. In confined space where additional actuator is not feasible, the variable stiffness can be an efficient solution for controlling small and delicate surgical instruments. Additionally, low stiffness is preferred for safety inside the human body and high stiffness is required to avoid buckling or in medical environments. Thus, this motivates the development of a variable stiffness mechanism which can adjust its stiffness to meet the needs imposed by varying conditions for the manipulation of meso/microscale surgical instruments. However, the stiffness control in continuum robots have been very challenging so far.

Many different variable stiffness mechanisms have been studied: some mechanisms employed shape memory alloys [2]–[4], shape memory polymers [5]–[8], fluidic flexible matrix composite [9], the combination of electrostatic force and



pneumatic force [10], anisotropic pneumatic force [11], tendon-drive mechanism [12], [13], tendon + fluidics mechanisms [14]–[17], variable neutral-line mechanism [18], layer jamming [19]–[22], granular jamming [23]–[32], low melting point alloy [33]–[35], low melting point polymer [36], magnetorheological elastomers [37]–[42], glass transition-based [43], [44], modulation of polymer [45], [46], and lever mechanism [47]. However, the current variable stiffness mechanisms have complex structure which is very difficult to scale down to satisfy the spatial constraint of minimally invasive surgery. For example, the tendon-pulley mechanism or conventional wrist structure is not easy to scale down because the length of the moment arm is too short to provide sufficient force and assembly is difficult for smaller dimensions. Also, some mechanisms use heat or high voltage stimulus to induce stiffness change which can lead to potential safety issue for medical usage. Additionally, shape memory polymers (SMP), conductive elastomers, low melting point alloy have relatively long response times due to heating and cooling time, for example, the response time takes more than 17 seconds to transform from rigid state to flexible state [33]. Moreover, the current mechanisms have binary or discrete stiffness states due to difficulties of precisely controlling heat or electric stimulus; jamming effect; pneumatic or fluidic pressure.

To overcome these limitations, we propose a variable stiffness mechanism using coaxial set of tubes with anisotropic flexural stiffness for continuum robots. The mechanism consists of two or more coaxial tubes with non-uniform through-hole patterns (material removal). The non-uniform patterning on each tube creates anisotropy in flexural stiffness ( $EI$ ). The stiffness of the mechanism respect to certain direction of load is changed by relative translation and rotation between the coaxial tubes. The proposed mechanism is distinguished from other variable stiffness mechanisms in terms of continuous variable stiffness, scalability, and response time.

## 1.2 Research Objectives and Contributions

The proposed variable stiffness mechanism can be utilized to control the motion for continuum surgical robots under interactions with nearby tissues in anatomically confined space. The mechanism demonstrates the following characteristics that are adequate for minimally invasive surgery.

First, the mechanism has continuous states of variable stiffness, instead of discrete states. Mechanisms based on electric, heat, or jamming stimulus mostly have discrete states of stiffness as it is difficult to precisely control their output from their input, or the input itself has binary or discrete states. However, the proposed mechanism precisely determines anisotropic distribution of the flexural stiffness by relative rotation and translation of the tubes. The flexural stiffness is well defined by relative rotational angle and longitudinal position in a continuous function form.

Secondly, the mechanism is scalable enough to be suitable for the dimension of minimally invasive surgery. The mechanism for changing the flexural stiffness is embedded in its structure and does not require bulky pneumatic lines or electrical wirings. As a result, in this study, it was possible to scale down the mechanism to 1.8mm-diameter, sufficiently small enough to be applied to minimally invasive surgery.

Third, the response time is much shorter than other mechanisms that relies on the phase change of the material. The stiffness of the mechanism can be changed by translational and rotational movement of the tubes in few microseconds.

Furthermore, using the variable stiffness mechanism, the stiffness-controlled needle is designed. Unlike the conventional steerable needles, it has stiffness as additional control variable. The needle has increased dexterity, reduce unreachable

area, increase safety by limiting the insertion speed, and minimize the damage to nearby tissue. Also, I built the customization process to adjust workspace and variable stiffness range of the steerable needle to targets. Finally, the proposed stiffness control needle is expected to be applied to various needlescopic applications such as radiofrequency ablation of liver and lung tumors, prostate brachytherapy, etc.

### **1.3 Research Overview**

The thesis is organized as follows. In chapter 2, the design and the modeling of the variable stiffness mechanism was demonstrated. I applied the non-uniform patterning method as a solution to variable stiffness mechanism without using bulky actuators or accessories. The flexural stiffness of the mechanism was modeled as a continuous function according to the rotational configuration of the multiple tubes. I suggested the control method to independently control the flexural stiffnesses along principal axes. In addition, I performed the finite element method simulation on the flexural stiffness of the mechanism. The UV laser machining system was used to engrave fine patterning on the nitinol or stainless steel tubes with the diameter of 3mm or less and the three point bending test was performed. To verify the variation of the flexural stiffness, the analytic modeling results, the simulation results, and the experimental results of the three-point bending test were compared each other to verify the variable stiffness mechanism. It also demonstrates how the mechanism was assembled and controlled by the motorized control system. A load test was performed to demonstrate the continuous stiffness variation of the mechanism. The

preliminary needle insertion test presented that the stiffness control varies the curvature of the needle's trajectory.

In chapter 3, using topology optimization method, the pattern shape was determined to maximize its variable stiffness range. The design parameters are able to be customized according to buckling map and target applications. The design process was built to satisfy the required variable stiffness range and the constraints while avoiding torsional/twist buckling.

In chapter 4, the variable stiffness mechanism was applied to the steerable needle, and the stiffness-controlled steerable needle provides an additional degree of freedom to control its trajectory. I modeled kinematic modeling for the proposed stiffness-controlled steerable needle. Using bi-cycle nonholonomic modeling, I studied the relationship between the flexural stiffness of the needle and the curvature of the needle's trajectory. Based on the kinematic model, the obstacle avoiding test was performed with the stiffness-controlled needle. The proposed needle varied the curvature of its trajectory to avoid the obstacles and demonstrated the wider workspace compared to conventional steerable needles.

In chapter 5, I discussed the characteristics of this variable stiffness mechanism, the theoretical and experimental results through chapter 2~4, and the contribution of the thesis in the context of continuum robot and minimally invasive surgical instruments.

## **Chapter 2 Continuously Variable Stiffness Mechanism using Asymmetric Patterns on Coaxial Tubes**

### **2.1 Design and Modeling of the Mechanism**

#### **2.1.1 The Concept and the Design of the Mechanism**

The proposed variable stiffness mechanism consists of two or more coaxial tubes with non-uniform through-hole patterns as shown in Fig. 2.2. The cross section of the tube consists of arc-shaped units with (shaded) and without (unshaded) patterns as shown in Fig. 2.2. Averaging along the longitudinal direction, the patterning has an effect of decreasing the flexural stiffness ( $EI$ ) of the unit, leading to anisotropic distribution of the flexural stiffness ( $EI$ ) within its cross sections. As a result, the flexural stiffness of the tube with respect to the fixed load direction changes with the rotation of the tube.

The pattern design parameters determine the stiffness range— $m_1$  and  $l_1$  are the radial and the longitudinal distance between the patterns, respectively;  $m_2$  and  $l_2$  stand for width and height of an unit pattern, respectively;  $\theta$  for the angle of the arc unit;  $n$  for the number of units.

In the previous study [48], the prototype of the mechanism was fabricated with 3d printer (Objet Connex 260 Stratasys, USA) with 18mm diameter. In the prototype, anisotropic distribution of the flexural stiffness was built by printing each units with different materials. In this research, to minimize the dimension of the structure and

satisfy biocompatibility for applications in minimally invasive surgery, the structure was built using thin nitinol tubes. Nitinol is characterized by biocompatibility, superelasticity, and shape memory effect, so it is suitable for surgical instruments [49].

To create anisotropic distribution of flexural stiffness on nitinol tubes, the surface of the tube was partially slit patterned. We researched various types of patterns and chose dog-bone shape pattern to prevent failure [50]. Two types of non-uniform patterns, type A and B of Fig. 2.2 were patterned on the tubes for comparison. In type A, one  $60^\circ$  arc unit was patterned on half, and in type B, two  $60^\circ$  arc units were patterned on half. The specification of the inner/outer tube and the design parameters of the pattern were given as Table 2.1. The partial patterning of the tube surface grant non-uniform flexural stiffness to each tube, and the coaxial arrangement of the tubes results in variable stiffness mechanism. Thus, the mechanism does have embodied intelligence that controls variable stiffness by non-uniform flexural stiffness.

Table 2.1. The specification of the inner and outer tubes

Tube	$d_i$ (mm)	$d_o$ (mm)	E (GPa)	$l_1$ ( $\mu\text{m}$ )	$l_2$ ( $\mu\text{m}$ )	$m_1$ ( $\mu\text{m}$ )	$m_2$ ( $\mu\text{m}$ )	$\theta$ ( $^\circ$ )	n
Outer	1.60	1.80	62.8	250	110	385	372	60	90
Inner	1.27	1.47	60.3	250	110	471	372	60	90

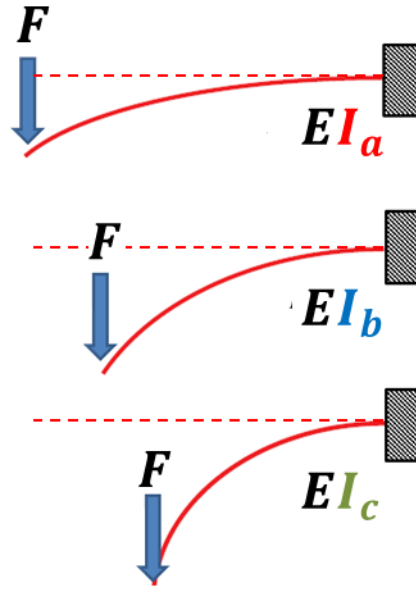


Fig. 2.1. Variable stiffness is able to assist motion control of continuum robots in anatomically confined space. Under the same external force,  $F$ , the deflection of the given structure increases as the stiffness decreases as  $EI_a > EI_b > EI_c$ .



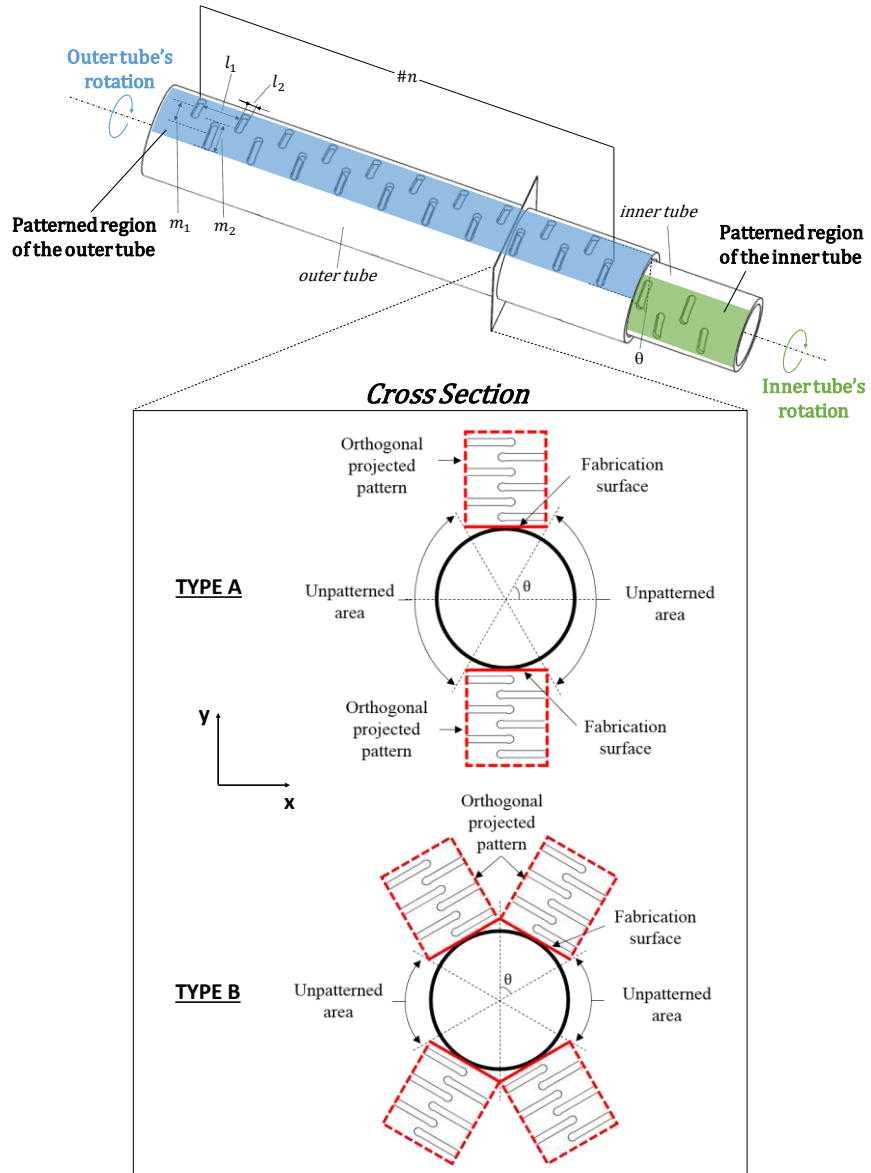


Fig. 2.2. The principles and the design parameters ( $l_1$ ,  $l_2$ ,  $m_1$ ,  $m_2$ ,  $\theta$ ,  $n$ ) of the pattern for variable stiffness mechanism. The inner and outer tubes are assembled coaxially, and each tube rotates and translates independently. The cross section view demonstrates how the through-hole patterns are engraved on the tubes of type A (60° per half) and B (120° per half).

There are two major ways to control the stiffness of the mechanism: relative rotational and translational movement between the coaxial tubes. Translating one tube from the other changes the flexural stiffness of the mechanism as shown in Fig. 2.3. At the flexible state, each patterned segment (the darker segments in Fig. 2.3) of the inner tube exactly overlaps with that of the outer tube. At the rigid state, each patterned segment of the inner tube positions at the middle of rigid segment of the outer tube. The rigid segment of the outer tube holds the patterned segment of the inner tube from bending more. To change neighboring segments is the key to achieve variable stiffness in this mechanism. Thus, by translating the inner tube, the mechanism reconfigures from flexible state to rigid state.

The other way to control the stiffness is to rotate one tube from the other. The rotational configuration difference also varies the stiffness of the mechanism. In Fig. 2.4, we consider that a tube rotates by  $\omega$  along counter-clockwise from the initial state and dashed area represents patterned area. The combination of relative translational and rotational motion between the non-uniform tubes provides various stiffness controls in the form of continuous functions rather than discrete ones. This paper more focuses on the stiffness variation by relative rotation through modeling, simulation, and experiments.



State	Relative Translational Configuration
<b>a) Rigid state</b>	
<b>b) Flexible state</b>	

Fig. 2.3. The flexural stiffness change according to translational configuration of the inner and outer tubes. The black parts stand for the patterned region while the grey parts stand for the unpatterned region. a) In view of the longitudinal direction, when the patterned parts of the outer tube overlap with the unpatterned of the inner tube. The structure is relatively rigid. b) On the other hand, when the patterned parts of the outer tube overlap the patterned of the inner tube. The structure is relatively flexible.

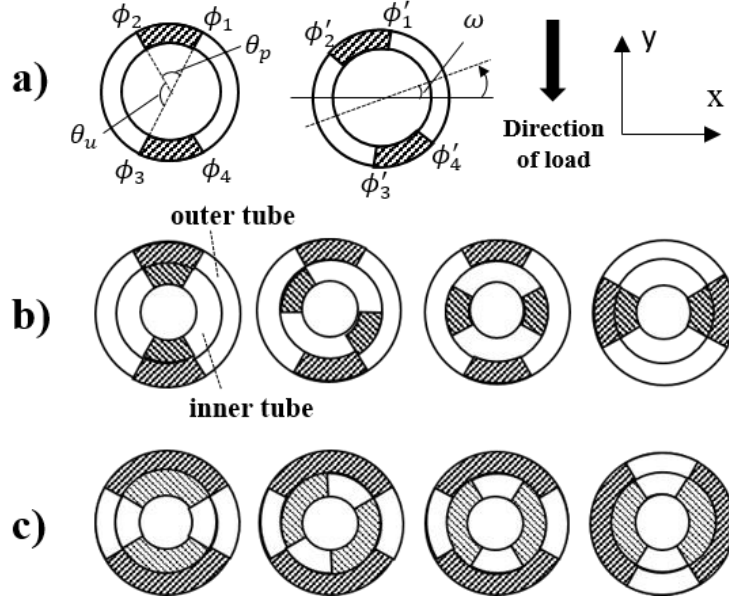


Fig. 2.4. a) The cross section of the single patterned tube at the initial state (left) and rotated by  $\omega$  from the initial state (right) where the dashed represents the patterned and the non-dashed represents the unpatterned. The relative rotation configuration of the inner and outer tubes results in the continuously variable stiffness of the structure. The inner and outer tubes are assembled coaxially and each tube rotates independently.  $\omega_1$  and  $\omega_2$  are the rotational angle for inner and outer tube, respectively, and  $(\omega_1, \omega_2)$  is an element of  $\{(0^\circ, 0^\circ), (60^\circ, 0^\circ), (90^\circ, 0^\circ), (90^\circ, 90^\circ)\}$  from the left for b) Type A and c) Type B.

### 2.1.2 Analytic Modeling of the stiffness of the Mechanism

The flexural stiffness of the mechanism is 2x2 symmetric matrix and changes with the rotational angle  $\omega$  of the inner and outer tube as in equation (1). Assume that the tube is radially divided into  $n$  sections as shown in Fig 2. If a section is patterned, it has lower flexural stiffness; if unpatterned, it has higher flexural stiffness. The flexural stiffness of the tube can be modeled as the sum of the stiffness of all sections,

$$K(\omega) = EI(\omega) = \begin{bmatrix} \sum_{i=1}^n (EI_{xx}(\omega))_i & \sum_{i=1}^n (EI_{xy}(\omega))_i \\ \sum_{i=1}^n (EI_{yx}(\omega))_i & \sum_{i=1}^n (EI_{yy}(\omega))_i \end{bmatrix} \quad (1)$$

where  $I_{xy} = I_{yx}$ ,  $EI_{xx}(\omega) = EI_{yy}\left(\omega + \frac{\pi}{2}\right)$ , and  $i$  indicates the number of the sections. Notice that  $I_{xx}$  is the lowest and  $I_{yy}$  is the highest at the initial state like Fig. 2.5 and  $I_{xx}(\omega) = I_{yy}\left(\omega + \frac{\pi}{2}\right)$ . The  $I_{xy}$  of the tube is zero at the initial state because it is symmetric to x axis.

The flexural stiffness of each section is product of its second moment of area ( $I_{xx}, I_{yy}, I_{xy}$ ) and its Young's modulus ( $E$ ). The second moment of area of the section changes with the rotation of the tube and its variation can be plotted using Mohr's circle as shown in Fig. 2.5. The reduction of the flexural stiffness by patterning can be modeled as the change of the “effective” Young's modulus of the section.

Each section is either patterned or unpatterned. Let  $E_p$  and  $E_u$  stand for “effective” Young's modulus of the patterned and unpatterned section, respectively. The

effective Young's modulus is defined by the averaging Young's modulus over the longitudinal length of the section. The effective Young's modulus  $E_u$  was measured by three-point bending test for the given nitinol tube as Table 2.1;  $E_p$  was measured by three-point bending test for the  $360^\circ$  patterned nitinol tube. The measured values  $E_p$  for the outer tube and the inner tube are 6.3 GPa and 6.0 GPa, respectively. Alternatively, in the previous study [51], based on the design variables of the pattern, we constructed a lumped analysis model of the effective Young's modulus of the patterned.

At first, consider  $K_{xx}$  when  $\omega$  is zero;  $r_o$  and  $r_i$  are the outer and the inner radius of tube, respectively;

$$\begin{aligned}
K_{xx}(0) &= \sum_{i=1}^n (EI_{xx}(0))_i \\
&= (EI_{xx}(0))_1 + (EI_{xx}(0))_2 + \cdots + (EI_{xx}(0))_{n-1} + (EI_{xx}(0))_n \\
&= E_1(I_{xx}(0))_1 + \cdots + E_{n-1}(I_{xx}(0))_{n-1} + E_n(I_{xx}(0))_n \\
&= E_p \int_{r_i}^{r_o} \int_{\phi_1}^{\phi_2} (r \sin \theta)^2 r d\theta dr + E_u \int_{r_i}^{r_o} \int_{\phi_2}^{\phi_3} (r \sin \theta)^2 r d\theta dr \\
&\quad + E_p \int_{r_i}^{r_o} \int_{\phi_3}^{\phi_4} (r \sin \theta)^2 r d\theta dr + E_u \int_{r_i}^{r_o} \int_{\phi_4}^{\phi_1+2\pi} (r \sin \theta)^2 r d\theta dr \quad (2)
\end{aligned}$$

$$\text{where } \phi_2 = \phi_1 + \theta_p, \phi_3 = \phi_1 + \pi, \phi_4 = \phi_1 + \pi + \theta_p \quad (3)$$

Define  $G(\phi', \phi, r_o, r_i)$  as

$$\begin{aligned}
G(\phi', \phi, r_o, r_i) &= \int_{r_i}^{r_o} \int_{\phi}^{\phi'} (r \sin \theta)^2 r d\theta dr \\
&= \int_{r_i}^{r_o} \int_{\phi}^{\phi'} r^3 \sin^2 \theta d\theta dr = \frac{r_o^4 - r_i^4}{4} \int_{\phi}^{\phi'} \sin^2 \theta d\theta \\
&= \left( \frac{r_o^4 - r_i^4}{4} \right) [(\phi' - \phi) - \sin(\phi' - \phi) \cos(\phi' + \phi)] \quad (4)
\end{aligned}$$

Using (4), solve (2)

$$\begin{aligned}
K_{xx}(0) &= E_p G(\phi_1, \phi_2, d_o, d_i) + E_u G(\phi_2, \phi_3, d_o, d_i) + E_p G(\phi_3, \phi_4, d_o, d_i) + \\
&E_u G(\phi_4, \phi_1 + 2\pi, d_o, d_i) \\
&= \left( \frac{r_o^4 - r_i^4}{4} \right) \left[ E_p (2\theta_p - 2\sin \theta_p \cos(2\phi_1 + \theta_p)) \right. \\
&\left. + E_u (2\pi - 2\theta_p + 2\sin(\theta_p) \cos(2\phi_1 + \theta_p)) \right] \quad (5)
\end{aligned}$$

For type A, , as  $\phi_1 = \frac{\pi}{3}$  and  $\theta_p = \frac{\pi}{3}$ , (5) becomes

$$K_{A_{xx}}(0) = \left( \frac{r_o^4 - r_i^4}{4} \right) \left[ E_p \left( \frac{2\pi}{3} + \sqrt{3} \right) + E_u \left( \frac{4\pi}{3} - \sqrt{3} \right) \right] \quad (6)$$

Similarly,

$$K_{A_{yy}}(0) = \left( \frac{r_o^4 - r_i^4}{4} \right) \left[ E_p \left( \frac{2\pi}{3} - \sqrt{3} \right) + E_u \left( \frac{4\pi}{3} + \sqrt{3} \right) \right] \quad (7)$$

For type B, as  $\phi_1 = \frac{\pi}{6}$  and  $\theta_p = \frac{2\pi}{3}$ , (5) becomes

$$K_{B_{xx}}(0) = \left( \frac{r_o^4 - r_i^4}{4} \right) \left[ E_p \left( \frac{4\pi}{3} + \sqrt{3} \right) + E_u \left( \frac{2\pi}{3} - \sqrt{3} \right) \right] \quad (8)$$

$$K_{B_{yy}}(0) = \left( \frac{r_o^4 - r_i^4}{4} \right) \left[ E_p \left( \frac{4\pi}{3} - \sqrt{3} \right) + E_u \left( \frac{2\pi}{3} + \sqrt{3} \right) \right] \quad (9)$$

The change of the flexural stiffness due to the rotation of the tube can be calculated by the transformation law of the flexural stiffness tensor. When  $R$  represents the rotational matrix by  $\omega$ , the 2 by 2 flexural stiffness,  $K(\omega)$  is determined by (10).

$$K(\omega) = RK(0)R^T \quad (10)$$

$$\begin{bmatrix} K_{xx}(\omega) & K_{xy}(\omega) \\ K_{yx}(\omega) & K_{yy}(\omega) \end{bmatrix}$$

$$= \begin{bmatrix} \cos(\omega) & \sin(\omega) \\ -\sin(\omega) & \cos(\omega) \end{bmatrix} \begin{bmatrix} K_{xx}(0) & 0 \\ 0 & K_{yy}(0) \end{bmatrix} \begin{bmatrix} \cos(\omega) & -\sin(\omega) \\ \sin(\omega) & \cos(\omega) \end{bmatrix}$$

$$= \begin{bmatrix} \cos^2(\omega)K_{xx}(0) + \sin^2(\omega)K_{yy}(0) & \cos(\omega)\sin(\omega)(K_{yy}(0) - K_{xx}(0)) \\ \cos(\omega)\sin(\omega)(K_{yy}(0) - K_{xx}(0)) & \sin^2(\omega)K_{xx}(0) + \cos^2(\omega)K_{yy}(0) \end{bmatrix} \quad (11)$$

As  $K_{xx}(0)$  and  $K_{yy}(0)$  are calculated in (6)~(9), the 2 by 2 flexural stiffness can be determined by (11). Expanding (11) for the type A.

$$\begin{aligned} K_{xx}(\omega) &= \cos^2(\omega)K_{xx}(0) + \sin^2(\omega)K_{yy}(0) \\ &= \left( \frac{r_o^4 - r_i^4}{4} \right) \left[ E_p \left( \frac{2\pi}{3} + \sqrt{3} \cos 2\omega \right) + E_u \left( \frac{4\pi}{3} - \sqrt{3} \cos 2\omega \right) \right] \quad (12) \end{aligned}$$



$$\begin{aligned}
K_{xy}(\omega) &= K_{yx}(\omega) = \cos(\omega) \sin(\omega) (K_{yy}(0) - K_{xx}(0)) \\
&= \left( \frac{r_o^4 - r_i^4}{4} \right) \cos(\omega) \sin(\omega) [E_p(-2\sqrt{3}) + E_u(2\sqrt{3})] \quad (13)
\end{aligned}$$

$$\begin{aligned}
K_{yy}(\omega) &= \sin^2(\omega) K_{xx}(0) + \cos^2(\omega) K_{yy}(0) \\
&= \left( \frac{r_o^4 - r_i^4}{4} \right) \left[ E_p \left( \frac{2\pi}{3} + \sqrt{3} (\cos(2\omega - \pi)) \right) \right. \\
&\quad \left. + E_u \left( \frac{4\pi}{3} - \sqrt{3} (\cos(2\omega - \pi)) \right) \right] \quad (14)
\end{aligned}$$

Similarly, the flexural stiffness for type B can be calculated. Notice (3), and it is enough to study for  $0 \leq \omega \leq \frac{\pi}{2}$  because the pattern is symmetric respect to the origin of the tube's circle at the cross section. The flexural stiffness of the multiple tube structure is the summation of those of the single tubes.

In Fig. 2.6., we plotted the change of the flexural stiffness  $K_{xx}$  of the double tube mechanism of type A and B based on (12) ~ (14). As the rotational angle changes from  $0^\circ$  to  $90^\circ$ , the figures show the change of the flexural stiffness ratio. The flexural stiffness was found to increase in the order of  $(0^\circ, 0^\circ)$ ,  $(60^\circ, 0^\circ)$ ,  $(90^\circ, 0^\circ)$ , and  $(90^\circ, 90^\circ)$  as illustrated in Fig. 2.6. The maximum difference is 2.10 times for type A; 4.27 times for type B. The detail results are summarized in Table 2.2.

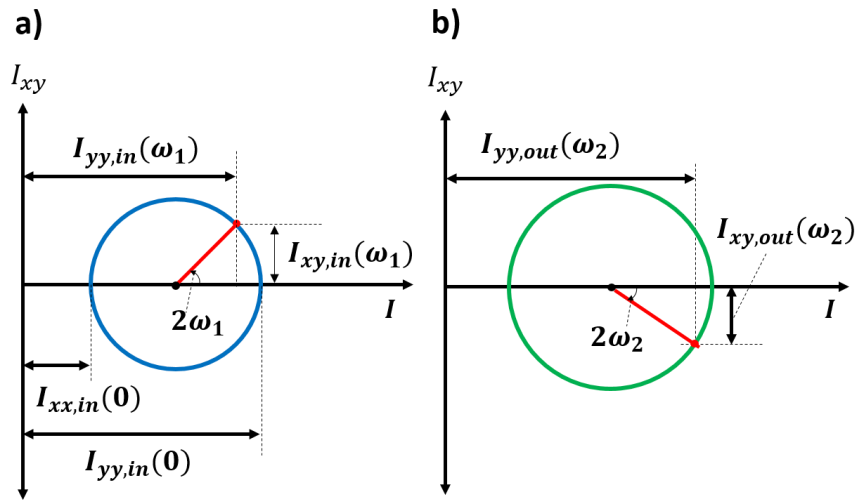
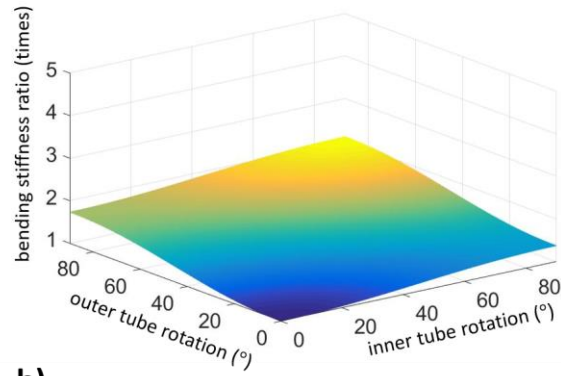


Fig. 2.5. a) The Mohr's circle (blue) for the inner tube for the rotated angle,  $\omega_1$ , b) the Mohr's circle (green) for the outer tube for the rotated angle,  $\omega_2$ .

**a)**



**b)**

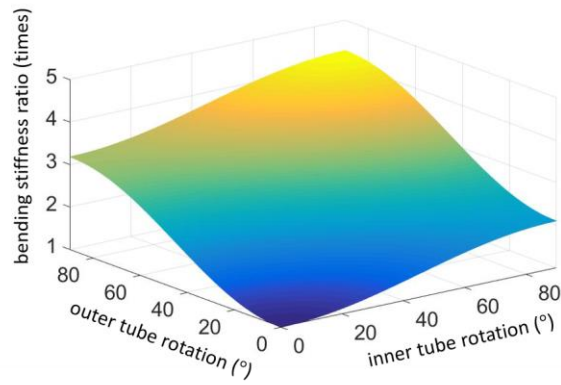


Fig. 2.6. As the inner and outer tubes rotate, the graph describes the change in the flexural stiffness ( $K_{xx}$ ) ratio of a) Type A and b) Type B structure according to the analytic modeling.

### 2.1.3 Decoupling $I_{xx}$ and $I_{xy}$

In Fig. 2.5, Mohr's circle demonstrates the relationship between  $I_{xx}$  and  $I_{xy}$  for the rotational angle  $\omega$  as (15).

$$\left(\frac{I_{yy}(0)-I_{xx}(0)}{2}\right)^2 = \left(I_{xy}(\omega)\right)^2 + \left(\frac{2I_{yy}(\omega)-I_{yy}(0)+I_{xx}(0)}{2}\right)^2 \quad (15)$$

The single tube rotation have coupled  $I_{xx}$  and  $I_{xy}$ . In other words, not only  $I_{xx}$  but also  $I_{xy}$  varies simultaneously while the tube rotates. When  $I_{xy}$  is not zero, the structure has out-of-plane deflection to the load, resulting in undesired motion. To cancel out  $I_{xy}$ , the counter-rotation of the outer tube is utilized. For instance, inner tube's rotation is given with  $I_{xy,in}$ . Then, one is always possible to have  $\omega_2$  to satisfy (16) when the radius of outer tube's Mohr's circle is same or larger than that of the inner.

$$I_{xy,in}(\omega_1) + I_{xy,out}(\omega_2) = 0 \quad (16)$$

In other words, contrast to the single tube mechanism, the multiple tube mechanism enables decoupling  $I_{xx}$  and  $I_{xy}$ , and it controls both independently. It explains why the multiple tubes are required to prevent out-of-plane deflection to load. In double tube structure, if we design the Mohr's circle of the inner and the outer tube to have the same radius, it achieves continuously variable stiffness of  $K_{xx}$  for all stiffness range while keeping  $K_{xy} = 0$ . To have the same radius of Mohr's circle for the both tubes, (16) should be satisfied.

Considering (6) ~ (9), (16) becomes (17). It means that  $\theta_p$  for the outer tube should be larger than that of the inner tube to satisfy (16) because the radius of the inner tube is smaller than that of the outer tube. Considering the geometry of the pattern, (17) can be expressed as (18).

$$\left( \frac{K_{yy}(0) - K_{xx}(0)}{2} \right)_{inner} = \left( \frac{K_{yy}(0) - K_{xx}(0)}{2} \right)_{outer} \quad (17)$$

$$\frac{R_o^4 - R_i^4}{r_o^4 - r_i^4} = \frac{E_{p,in} - E_u}{E_{p,out} - E_u} \quad (18)$$

where  $R_o$  and  $R_i$  stand for the outer and inner radius of the outer tube, respectively; in and out subscript represent the inner tube and the outer tube, respectively. When the radiuses of Mohr's circle are same each other,  $\omega_1$  is simply equal to  $-\omega_2$  to satisfy (16). Alternatively, the structure is able to consist of three or more coaxial tubes to control  $I_{xx}$  and  $I_{xy}$  independently.

#### 2.1.4 Pattern Design to Customize the Stiffness Range

Set the ratio of  $K_{xx}(90^\circ)$  to  $K_{xx}(0^\circ)$  to compare the maximum and minimum stiffness of a single tube. Using (12) and  $\phi_1 = \frac{\pi - \theta_p}{2}$  in our design as Fig. 2.4, the ratio becomes (19).

$$K_{xx\_ratio} = \frac{K_{xx}(90^\circ)}{K_{xx}(0^\circ)} = \frac{(2\theta_p - 2\sin\theta_p) + (E_u/E_p)(2\pi - 2\theta_p + 2\sin\theta_p)}{(2\theta_p + 2\sin\theta_p) + (E_u/E_p)(2\pi - 2\theta_p - 2\sin\theta_p)} \quad (19)$$

It means the ratio is the function of the central angle for the patterned area,  $\theta_p$  and  $E_u/E_p$ . The value  $E_u/E_p$  is determined by the pattern shape. Fig. 2.7 demonstrates the variation of stiffness ratio for  $0^\circ \leq \theta_p \leq 180^\circ$  where  $E_u/E_p$  are given according to our pattern design. In the result, the ratio shows the maximum value, 4.378 times at  $\theta_p = 128.9^\circ$ . The angle of patterned area for the maximum ratio depends on the value of  $E_u/E_p$ . On the other hand, it is trivial that the ratio has the minimum value of 1 at  $\theta_p = 0^\circ$  and  $180^\circ$ . Thus, by tuning  $\theta_p$  and  $E_u/E_p$ , we can optimize the desired range of the stiffness.

Also, we set the ratio of  $EI(90^\circ, 90^\circ)$  to  $EI(0^\circ, 0^\circ)$  to compare the maximum to the minimum stiffness of the double tube mechanism as (20).

$$\frac{EI(90^\circ, 90^\circ)}{EI(0^\circ, 0^\circ)} = \frac{EI(90^\circ)_{inner} + EI(90^\circ)_{outer}}{EI(0^\circ)_{inner} + EI(0^\circ)_{outer}} \quad (20)$$

Let  $t$  be the thickness of the tube, then  $d_i = d_o - 2t$ .  $d_i^4 = (d_o - 2t)^4 = d_o^4 - 2td_o^3 + 4t^2d_o^2 - 8t^3d_o + 16t^4 \approx d_o^4 - 2td_o^3$ . When  $t_i$  and  $t_o$  are the thickness of the inner and outer tube, respectively, expands (20) to (21).

$$\begin{aligned}
& (1/64)(t_i d_o^3 [E_{p_i}(2\theta_p - 2\sin \theta_p) + E_{u_i}(2\pi - 2\theta_p + 2\sin \theta_p)] + \\
& t_o D_o^3 [E_{p_o}(2\theta_p - 2\sin \theta_p) + E_{u_o}(2\pi - 2\theta_p + 2\sin \theta_p)]) \div \\
& (t_i d_o^3 [E_{p_i}(2\theta_p + 2\sin \theta_p) + E_{u_i}(2\pi - 2\theta_p - 2\sin \theta_p)] + t_o D_o^3 [E_{p_o}(2\theta_p + \\
& 2\sin \theta_p) + E_{u_o}(2\pi - 2\theta_p - 2\sin \theta_p)]) \quad (21)
\end{aligned}$$

Finally, (20) shows that the stiffness ratio is determined by the tube dimension, pattern shape, and the angle for the patterned area,  $\theta_p$ . The relationship helps to establish the stiffness range of the mechanism to fulfill target requirements.

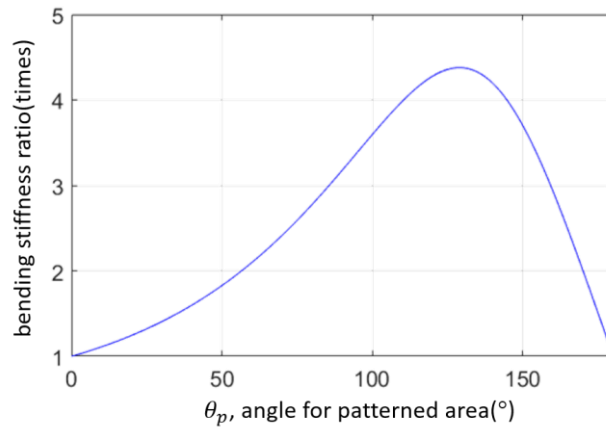


Fig. 2.7. The flexural stiffness ratio of the single patterned tube according to the central angle for the patterned area,  $\theta_p$ . The stiffness ratio is the maximum when  $\theta_p = 128.9^\circ$



## 2.2 Finite Element Method Simulation

To verify the variation of the stiffness predicted from the model, three-point bending test like Fig. 6a was simulated for different relative rotations between the coaxial tube set. The FEM simulation was performed using Abaqus 6.14. (Dassault Systèmes, Vélizy-Villacoublay, France). There is a study to perform Finite element method (FEM) simulation on superelastic nitinol [52]. Since the sample and the load is symmetric with respect to the middle point, only the half of the three-point bending point test was simulated as in Fig. 2. 8c to reduce the computational load.

In the FEM simulation, the middle point was displaced 2 mm downwards and the bearings had surface to surface contact with the coaxial tube structure. The length between the two lower supporters is 40mm. Force-displacement relationship of the middle point was computed. The simulation was performed for the selected configurations shown in Fig. 2.4b and 2.4c of  $\{(0^\circ, 0^\circ), (60^\circ, 0^\circ), (90^\circ, 0^\circ), (90^\circ, 90^\circ)\}$  for type A and B. The load-deflection relationships are plotted in Fig. 2.9. The flexural stiffness was calculated by fitting the linear trend line to the load-deflection curve and substituting the slope of the trend line into (12). In Fig. 2.9, the flexural stiffness was found to increase in the order of  $(0^\circ, 0^\circ)$ ,  $(60^\circ, 0^\circ)$ ,  $(90^\circ, 0^\circ)$ , and  $(90^\circ, 90^\circ)$ . The results are listed in Table 2.2.

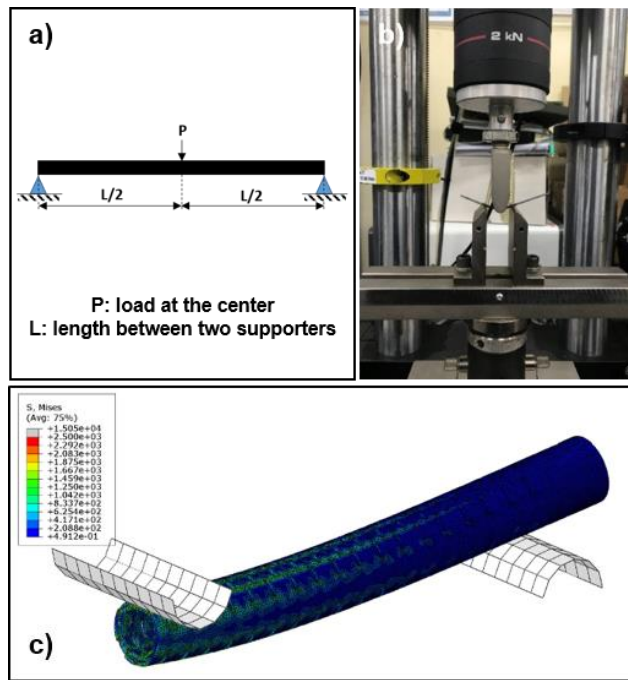


Fig. 2.8. Three-point bending test by a) the diagram, b) the experimental set-ups using Instron 5900 series, and c) FEM simulation results of three-point bending test by Abaqus 6.14.

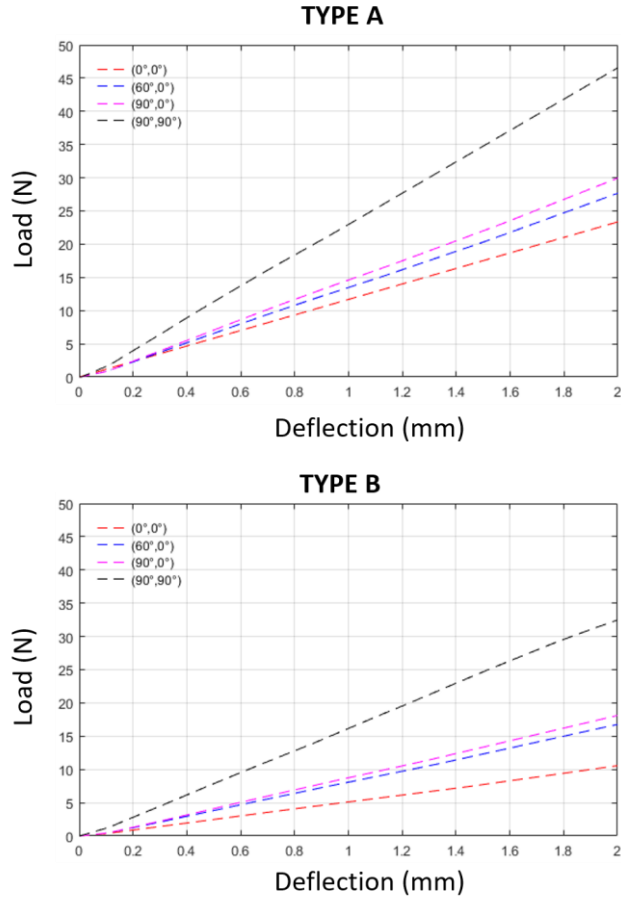


Fig. 2.9. The FEM simulation results of Type A (upper) and Type B (lower) structure when  $(\omega_1, \omega_2) \in \{(0^\circ, 0^\circ), (60^\circ, 0^\circ), (90^\circ, 0^\circ), (90^\circ, 90^\circ)\}$

## **2.3 Fabrication and 3-point Bending Experiment**

The through-hole patterns were engraved on the nitinol tube by nanosecond UV laser machining. To verify the stiffness variability of the mechanism and the feasibility of the model, the variation of the flexural stiffness predicted from the model in Section II and simulation in Section III was compared with the experimental results. Then, we set up a robotic system to control the stiffness of the mechanism. Using the system, continuous variation of the stiffness was demonstrated by simple load test. Also, an experiment on potential application of the mechanism in stiffness-controlled needle steering was performed.

### **2.3.1 Ultra Violet Laser Machining**

Based on the proposed mechanism, the tubes should have non-uniform flexural stiffness to accomplish variable stiffness. We engraved patterns on the nitinol tubes by ultra violet (UV) laser. Owing to its mechanical strength, superelasticity, and excellent biocompatibility, nitinol is regarded as an outstanding material for biomedical applications, and intensive study of nitinol fabrication has been conducted [53], [54]. In our study, we employed Nd:YVO<sub>4</sub> laser system (wavelength of 355 nm, line-width of 20  $\mu\text{m}$ , pulse duration of 30 ns, repetition rate of 100 kHz) to engrave the patterns on the tubes. Due to the surface curvature of the tubes, the maximum cutting depth of the tube was approximately 150  $\mu\text{m}$  with a maximum laser power of 3.1 W, scanner speed of 40 mm/s, and 50 repetitions.

The desired pattern, illustrated in Fig. 2.2, spanned the tube's surface along the radial and axial directions. A specialized system was required to cut the pattern into

the curved surface with minimum distortion. Ideally, the rotation of the tube would be synchronized with the laser scanner movement to allow for continuous patterning along the perimeters of the tube, but this is technically demanding. To simplify the procedure while minimizing the error caused by the curvature of the tube surface, the surface of the tube was divided into six equal regions and each region was patterned at a time. The tube was then rotated  $60^\circ$  and patterned again, for a total of two (type A) or four (type B) processing repeats according to its design. The surface can be divided into smaller regions depending on the pattern design. Also, the cooling system and enough cooling time to reduce heat affect near laser engraving spots.

Fig. 2.10a demonstrates the machining set-up for the tubes. A rotary motor stage (Unice E-O Service Inc., Taiwan) was installed to rotate the tube precisely. The tube was fixed by a collet chuck, a linear guide set various lengths of the tubes, and a cone-shaped bearing support prevented bending and twisting of the tube. A CCD camera (Color 5MP CMOS camera, Mightex Systems, Pleasanton, CA, USA) was placed above the specimen tube to monitor its dislocations after rotation, and an optoelectronic displacement measurement system (Micro- Epsilon, opto-NCDT 1402) was used to calibrate the vertical position of the tube to match the focal length of the laser beam. Fig. 2.10b demonstrates the enlarged image of the engraved surface. Due to heat affection, the set-up laser system engraves the pattern larger than its original design. Twenty tests confirmed that the length increased by an average of  $29\mu\text{m}$  over the design. We designed the pattern to compensate for  $29\mu\text{m}$  to obtain more accurate fabrication results. Fig. 2.10c and 2.10d show the fabrication results for type A and B, respectively. Type B has wider patterned area than Type A. The pictures were taken by a microscope (SZ61, Olympus, Tokyo, Japan) with digital camera (acqucam2, jnoptic Co. ltd, Seoul, Korea).

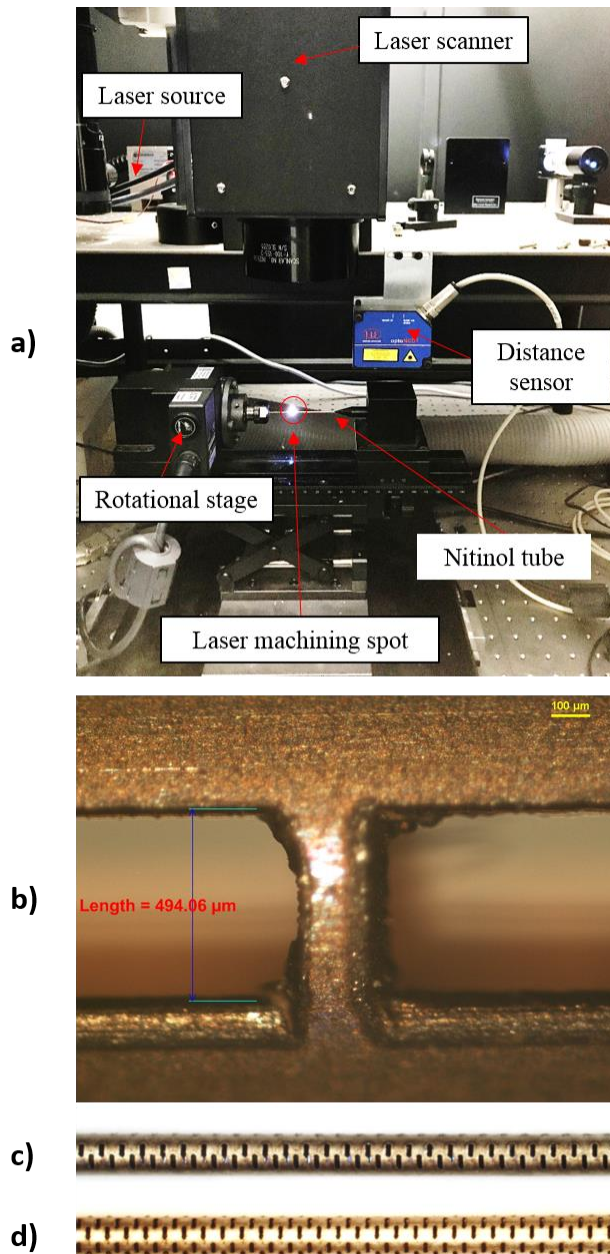


Fig. 2.10. a) The UV laser machining set-ups, b) the microscopic image of the engraved tube surface, c) the laser patterned nitinol tube of Type A and d) Type B

### 2.3.2 Three-point Bending Test

To experimentally verify the stiffness variation of the mechanism, we performed a bending rigidity test. The result was compared with that from the simulation. The mechanism with two types of pattern, as shown in Fig. 2.2 and 2.4, were prepared for bending tests.

The three-point bending method was chosen to examine the bending rigidity of tubes. In this research, we tested specimens with the Instron 5900 series, a high precision system of measurement. Fig. 2.8a and 2.8b show how the bending test set-ups were installed and a 2 kN load cell was connected. The system measured the applied force and the vertical displacement to calculate the flexural stiffness.

The test was repeated three times per specimen to check its repeatability. The length between the two lower supporters is 38mm ( $L=38\text{mm}$ ) and a concentrated load  $P$  was applied to the center;  $I$  was the second moment of tube, and  $\omega_0$  was the deflection at the center of the tube. Then, the flexural stiffness,  $(EI)$ , is given by (22), where  $P/\omega_0$  is the slope of the load-deflection curve.

$$K_{xx} = EI = \left(\frac{P}{\omega_0}\right)\left(\frac{L^3}{48}\right) \quad (22)$$

For the relative rotational movement, the three-point bending test was performed for each of type A and B. The inner and outer tubes were tested at  $0^\circ$  and  $90^\circ$  to test flexural stiffness. The mechanism was tested for the selected configurations of Fig.2.4b and 2.4c where  $(\omega_1, \omega_2)$  is an element of  $\{(0^\circ, 0^\circ), (0^\circ, 60^\circ), (0^\circ, 90^\circ), (90^\circ, 90^\circ)\}$  and the results are shown in Fig. 2.11. The load-deflection curve for each test

was obtained in the three-point bending test. The flexural stiffness was calculated by fitting the linear trend line to the load-deflection curve and substituting the slope of the trend line into (21). As with the analytical modeling results, type B exhibits more changes in flexural stiffness than type A; type A showed the 2.17 times difference and type B showed 4.44 times difference. The detail results are summarized in Table 2.2.



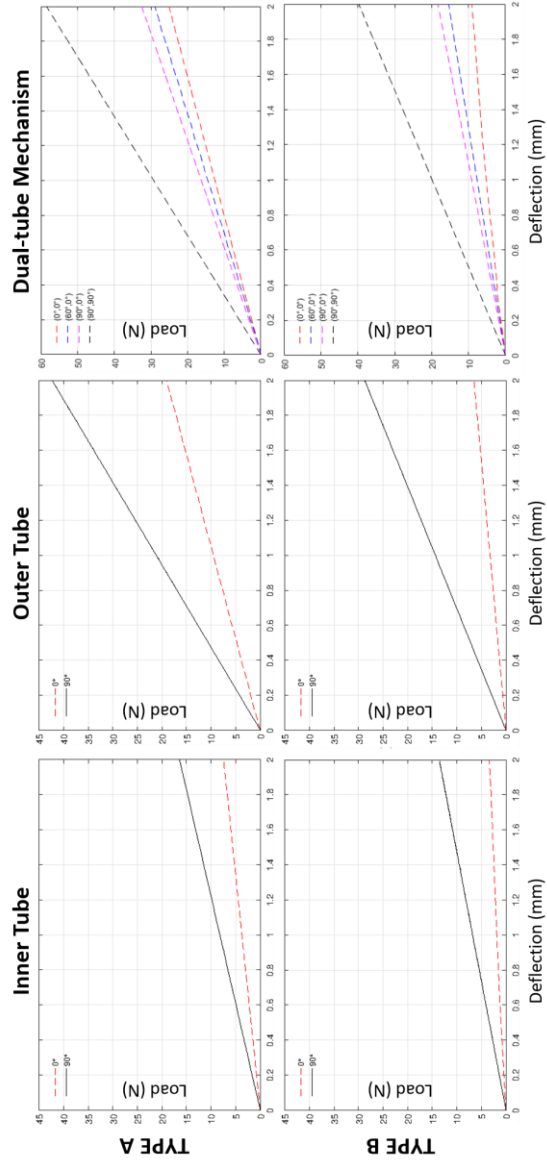


Fig. 2.11. The load-deflection plots from three-point bending experiment. The plots of the first column (the inner tube) and the second column (the outer tube) compare the flexural stiffnesses between the rotated angles of  $0^\circ$  and  $90^\circ$ . The third column plots compare the stiffness of the structure where  $(\omega_1, \omega_2) \in \{(0^\circ, 0^\circ), (60^\circ, 0^\circ), (90^\circ, 0^\circ), (90^\circ, 90^\circ)\}$ .

### 2.3.3 Comparison of the Flexural Stiffness Change

We obtained the flexural stiffness of the mechanism through analytical modeling, FEM simulation, and three-point bending experiments. For all three methods, the flexural stiffness changes when  $(\omega_1, \omega_2)$  is an element of  $\{(0^\circ, 0^\circ), (0^\circ, 60^\circ), (0^\circ, 90^\circ), (90^\circ, 90^\circ)\}$  are compared in Table 2.2. In the table, the value in parenthesis indicates the ratio compared to the value at  $(0^\circ, 0^\circ)$ . We set the minimum value  $(0^\circ, 0^\circ)$  to the standard value and compared the trends of flexural stiffness change. In the results, three methods have the consistency in the tendency of flexural stiffness: the flexural stiffness increases in the order of  $(0^\circ, 0^\circ)$ ,  $(0^\circ, 60^\circ)$ ,  $(0^\circ, 90^\circ)$  and  $(90^\circ, 90^\circ)$  where  $(0^\circ, 0^\circ)$  is the minimum and  $(90^\circ, 90^\circ)$  is the maximum. Type B showed more flexural stiffness change compared to type A. Comparing the maximum and minimum experimental values, type A showed 2.10 times increase of stiffness and type B showed 4.23 times for analytic modeling and similar increasing for other methods as Table 2.2. It demonstrates that the range of stiffness is wider as more sections are patterned. Three-point bending experiment results are relatively lower than other results. The fabrication. Overall, the results show the consistency of the trend of stiffness change by all three methods.

Table 2.2. The flexural stiffness change and its ratio (times) comparison among the analytic modeling, the FEM simulation, and the three point bending experiment

	$\omega_1, \omega_2$	$K_{xx} \text{ (kNmm}^2\text{)}$		
		Analytic Modeling	FEM Simulation	3pt bending Experiment
Type A	$0^\circ, 0^\circ$	16.6 (1.00)	15.6 (1.00)	14.4 (1.00)
	$60^\circ, 0^\circ$	21.1 (1.27)	18.6 (1.19)	16.6 (1.16)
	$90^\circ, 0^\circ$	22.6 (1.37)	20.1 (1.29)	18.6 (1.30)
	$90^\circ, 90^\circ$	34.7 (2.10)	31.5 (2.02)	33.4 (2.33)
Type B	$0^\circ, 0^\circ$	5.61 (1.00)	7.07 (1.00)	5.12 (1.00)
	$60^\circ, 0^\circ$	10.2 (1.81)	11.3 (1.60)	8.83 (1.72)
	$90^\circ, 0^\circ$	11.7 (2.08)	12.2 (1.74)	10.5 (2.05)
	$90^\circ, 90^\circ$	23.7 (4.23)	22.0 (3.12)	22.7 (4.44)

### 2.3.4 Demonstration of Continuously Variable Stiffness

A robotic system is built to vary the stiffness of the mechanism. The system has four degrees of freedom: translation along and rotation about the insertion axis for each tube. The collet chucks connected with motors hold the tubes; each tube rotates or translates as each motor operates. The cantilever load test was performed while the stiffness of the mechanism varied. A weight was hung at the distal end of the mechanism and vertical deflection of the distal tip was measured. The flexural stiffness was calculated from the measured deflection. The design parameter of the tube used in the load test was (200 $\mu\text{m}$ , 400 $\mu\text{m}$ , 800 $\mu\text{m}$ , 1500 $\mu\text{m}$ , 60°, 90) of type B patterning. Fig. 2.12 compares deflections and flexural stiffness when 10g and 20g loads are applied to the mechanism with different rotational configuration,  $(\omega_1, \omega_2) = (0^\circ, 0^\circ), (90^\circ, 90^\circ)$ . The deflection at  $(0^\circ, 0^\circ)$  is the maximum while, that of  $(90^\circ, 90^\circ)$  is the minimum. The flexural stiffness increases from 1490.8  $\text{Nmm}^2$  to 10766  $\text{Nmm}^2$  (about 7.2 times) when  $(0^\circ, 0^\circ)$  and  $(90^\circ, 90^\circ)$  are compared. The complimentary video shows the change of deflection while both the inner and outer tubes have rotational angles that vary with continuous sinusoidal wave. It demonstrates the continuously variable stiffness change by relative rotational movement. Additionally, the response time is only few microseconds as the motors directly rotates the coaxial tubes. In the experiment, snapping is not observed. In addition, using counter rotation method introduced in Section II-D, we observed that the out-of-plane deflection is negligible (less than a few tens of micrometers).

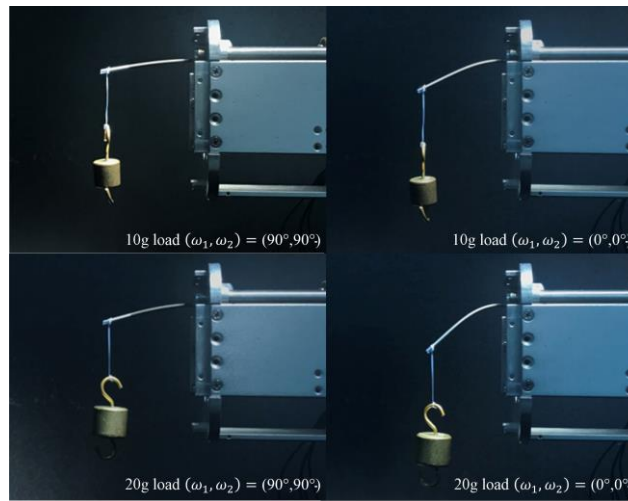


Fig. 2.12. The cantilever load test was performed for the variable stiffness structure. The tip position demonstrated the continuously changed deflection while both the inner and outer tubes had rotational angles that varied with continuous sinusoidal waves.

## **2.4 The Feasibility of Stiffness-Controlled Steerable**

### **Needle**

One of possible applications of the mechanism is steering bevel tip needle. As a flexible needle with a bevel tip is pushed through soft tissue, the asymmetry of the tip causes the needle to bend. The tissue imposes a reaction force on the bevel that deflects the needle tip, causing it to follow an arc [55], [56]. As our variable stiffness mechanism enables the steerable needles to change its directional flexural stiffness, it can control the curvature of the bending, and, in other words, vary the radius of the arc that needle follows. Thus, the mechanism grants additional input to the steerable needle system. We proceeded the demo test to control the curvature of the needle using the mechanism.

The experimental setup used for inserting a stiffness-controlled steerable needle into phantom tissue is shown in Fig. 2.13a and 2.13b. The inner tube has a bevel tip of 45 degrees at the distal end and uniformly patterned. The outer tube is non-uniform patterned as type B. Alternatively, the needle can consist of a bevel-tipped outer tube and a non-uniform patterned inner tube. It is also possible to have three or more coaxial tubes.

The controller controls 2R-2T motion of the steerable needle. The rotational and translational movement of each tube (the inner and the outer) is controlled independently. The rotational movement is controlled by Dynamixel using CAN communication and the translational movement is controlled by Maxon motor using RS-485 communication. Each Maxon motors' rotational movement transits into translational movement through lead screw while Dynamixel rotates each tube held by collet chuck. Telecentric lens or camcorder is set to capture the motion of the

distal tip of the needle. The phantom tissue is prepared with elastic properties similar to human tissues [57]. The needle is inserted in the homogenous phantom prepared with a mixture of 83% water, 12% gelatin, and 5% sugar. The control system with four degrees of freedom inserts the needle with a velocity of 1 mm/s and the needle stops when inserted 50mm. For the rotational configurations of  $(0^\circ, 0^\circ)$  and  $(0^\circ, 90^\circ)$ , the needle was inserted into the phantom and compared the position of the distal tip. The needle tip deflected 11.6mm along x-direction at  $(0^\circ, 0^\circ)$  while it deflected 3.5mm along x-direction at  $(0^\circ, 90^\circ)$  from the insertion point as illustrated in Fig. 2.13c and 2.13d. The radii of curvature are 89.7mm and 327mm for  $(0^\circ, 0^\circ)$  and  $(0^\circ, 90^\circ)$ , respectively. The complementary video shows how the needle bends depending on its stiffness. The smaller the stiffness of the mechanism is, the smaller the radius of curvature of the arc that needle follows becomes.

Thus, the variable stiffness mechanism adds the additional degree of freedom to control the trajectory of the needle. The current steerable needles use insertion speed change [1] or duty cycle method [58] to change its curvature of trajectory. On the other hand, varying the stiffness of the needle allows one to change the radius of curvature while minimizing effects on nearby tissues. As a result, the reachable area of the steerable needle can be expanded without changing the insertion speed or constantly rotating the needle during insertion, as illustrated in Fig. 2.14.

The difference of the workspace between the needle with (case ii) and without (case i) the stiffness control is simulated in Fig. 2.14. In both cases, the insertion speed was constant and the bevel tip tube does not rotate after insertion started. In case i, the radius of curvature was fixed to 60 mm due to constant stiffness, and in case **ii**, the radius of curvature was variable from 25mm to 60 mm due to variable stiffness. For both cases, the needle is inserted for 35mm. The case i has the cone-

like workspace with no thickness while the case ii has the thick cone-like workspace like Fig. 2.14a and 2.14b. The cross section of the case i's workspace is only two curved line while that of the case ii's workspace has wider area as illustrated in Fig. 2.14c and 2.14d. The stiffness-controlled steerable needle was profoundly studied with kinematic modeling and obstacle avoiding test in chapter 4 after the optimization and the parametric study of the pattern were performed in chapter 3.



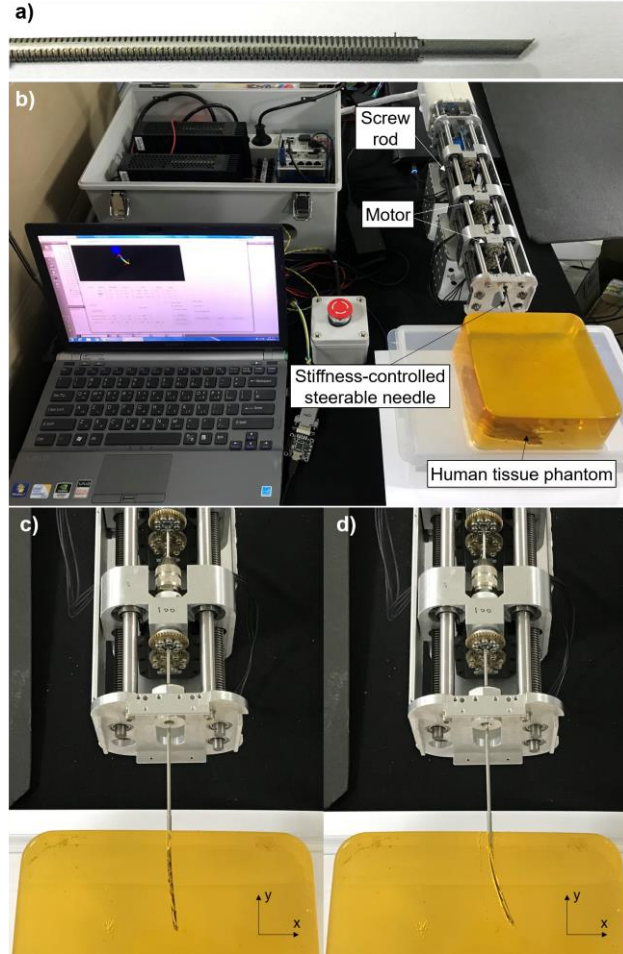


Fig. 2.13. a) The stiffness-controlled steerable needle consists of the bevel-tip inner tube and the non-uniform patterned outer tube, b) the experimental set-ups for the insertion of the stiffness-controlled steerable needle. The comparison of the needle's distal tip position at c)  $(\omega_1, \omega_2) = (0^\circ, 90^\circ)$  and d)  $(0^\circ, 0^\circ)$ .

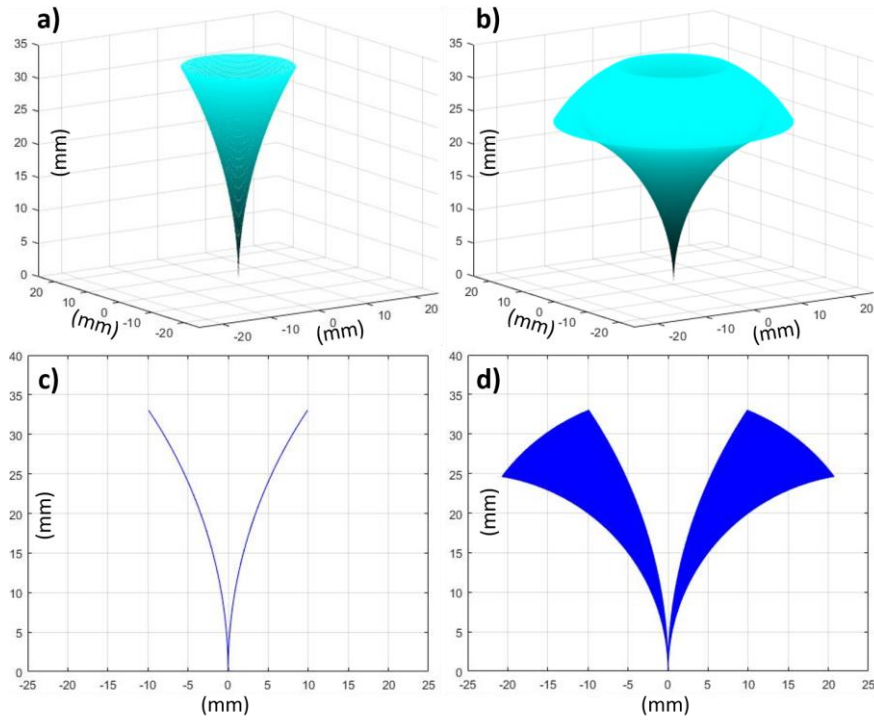


Fig. 2.14. The workspace comparison between a) the needle with constant insertion speed and b) the stiffness-controlled needle with the constant insertion speed. c) and d) demonstrate the cross section of a) and b), respectively.

## **Chapter 3 Parametric Study of the Patterns for Variable Stiffness**

In the previous chapter, I suggested the new mechanism for variable stiffness using anisotropic distribution of the flexural stiffness. In this chapter, the shape and the design parameters of the pattern were studied for variable stiffness mechanism. Using topology optimization, the pattern was optimized to maximize its variable stiffness capability while satisfying the given constraints. The design parameters of the pattern are able to be adjusted to have the desired variable stiffness range. Additionally, the design parameters were analyzed to avoid buckling.

### **3.1 The Topology Optimization of the Pattern**

In order to find an optimized pattern without using any predetermined shape, I used the topology optimization using Solid Isotropic Material with Penalization (SIMP) [59], which was a gradient based optimization method and uses finite element mesh based on an objective function by changing the density of every element in each iteration. It is a mathematical method that optimizes material layout within a given design space, for a given set of loads, boundary conditions and constraints with the goal of maximizing the performance of the system. Using topology optimization, the pattern was optimized to maximize its variable stiffness capability while satisfying the given constraints.

To maximize the variable stiffness capability of the mechanism, I analyzed pattern design providing a large stiffness ratio of the stiffnesses along principal axes.

The considered mechanism consisted of two concentric tubes. The total stiffness,  $I_{total}$  of two-tube set (inner tube, outer tube) is the linear summation of stiffness of each tube:

$$I_{total,xx} = I_{1,xx} + I_{2,xx} \quad (23)$$

$$I_{total,yy} = I_{1,yy} + I_{2,yy} \quad (24)$$

To maximize the variable stiffness capability of the mechanism, it is required to find pattern design with  $\min \left\{ \frac{I_{total, yy}}{I_{total, xx}} \right\}$ . The mechanism consists of two concentric tubes and  $I_{total}$  of two tube set is equal to the linear summation of two tubes.

As the inner and outer tube have the same anisotropic distribution along the radial direction,  $\min \left\{ \frac{I_{total, yy}}{I_{total, xx}} \right\}$  is to find  $\min \left\{ \frac{I_{1, yy}}{I_{1, xx}} \right\}$  &  $\min \left\{ \frac{I_{2, yy}}{I_{2, xx}} \right\}$ , and consequently to find  $\min \left\{ \frac{I_{yy}}{I_{xx}} \right\}$  for the single tube. Thus, I set objet function as  $\min \left\{ \frac{I_{yy}}{I_{xx}} \right\}$  for a single tube. Additionally, there are two major constraints: 1) the stiffness should not be lower than a certain value to perform tissue operations,  $I_{xx} \geq \beta \cdot I_{xx0}$ , where  $\beta$  depends on the application and 2) it should avoid buckling to prevent the failure of the mechanism. Thus, the topology optimization for the pattern of the variable stiffness structure was studied under the following conditions:

$$\text{Object Function} = \min \left\{ \frac{I_{yy}}{I_{xx}} \right\} \quad (25)$$

Constraint:

$$1) \quad I_{xx} \geq \beta \cdot I_{xx0} \quad (26)$$

2) Bending & Torsional Buckling

At first, the topology optimization was performed to find the optimized shape of the patterns. For the topology optimization, a FE analysis software using Tosca structure was also utilized (Abaqus 6.14; Dassault Systems). I examined various object functions and constraints to ensure the optimization of the pattern. Table 3.1 shows examples of four representative cases among various cases.  $r_x$  and  $r_y$  stand for the rotation angle along x and y axis when a load is applied, respectively; V stands for volume and response operator indicates step mode in Abaqus Tosca. A constraint that the volume of the tube could be reduced by only up to 30% of the initial volume was imposed. At the same time, step operator was also considered as another option to calculate the design response, and step operator indicated the mode to be applied for each step. As results, in all cases, the optimized material-properties distribution converged to the “vertical” slits along longitudinal direction like Fig.3.1. Thus, the vertical slit shape was determined to  $\min \left\{ \frac{I_{yy}}{I_{xx}} \right\}$  through the topology optimization.

Table 3.1. The topology optimization cases for variable stiffness

case	design response	step operator	constraint	Geom. Restric.
1	$Min( r_x ), Min(- r_y )$	Sum	$V \leq 0.7$	member size range
2	$Min( r_x )$	Max.	$V \leq 0.7$	Max. member size
3	$Max( r_y )$	Max.	$V \leq 0.7$	.
4	$Max( r_y )$	Max.	$V \leq 0.7$	.

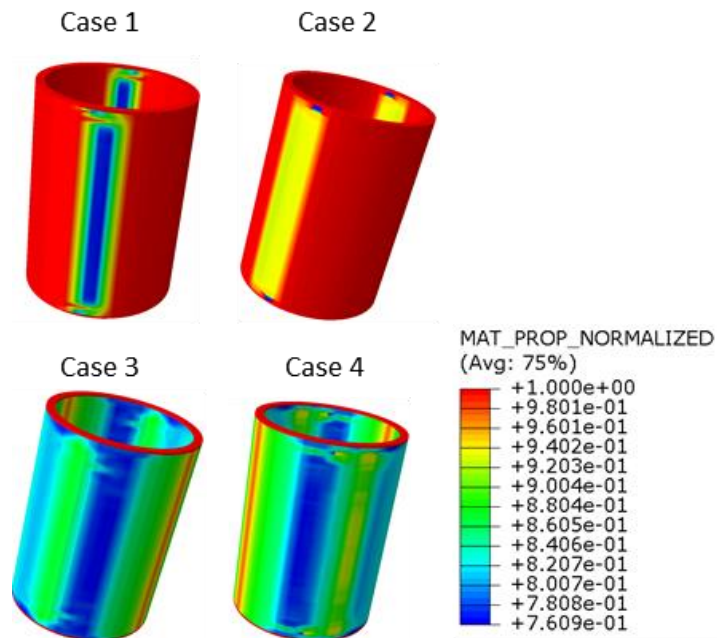


Fig. 3.1. The material-properties distribution of the topology optimized pattern for various cases of Table 3.1. The optimized pattern has the shape of rectangular shape along the longitudinal direction.

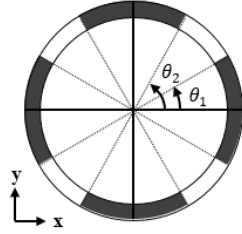
As the next step, I optimized the number of the vertical slits. I set different number of vertical slits at initial state. In Fig.3.2, type A represents one slit in quadrant 1, and type B represents two slits in quadrant 1. In the figures, the white section is the patterned while the black section is the non-patterned. The constraint  $I_{xx} \geq \beta \cdot I_{xx0}$  is given for  $\beta \in [0.2, 0.4, 0.6, 0.8]$ . Then, I performed topology optimization for type A and B under given constraints.

Fig. 3.3. demonstrated the  $I_{yy}/I_{xx}$  ratio change according to  $\theta_1$  and  $\theta_2$  value when  $\beta = 0.6$ . In graph, to minimize the object function, the optimized pattern should have  $\theta_1 = 0^\circ$  and  $\theta_2$  which is determined by the constraint condition. Table 3.2 represents the optimized results for type A and B, and the cross-sections of the optimized type A and B are demonstrated in Fig.3.2b. In results, both type A and B have only one pair of vertical slits that are symmetrical to the origin. In other words, even if there are several pairs of vertical slits at the initial state, the optimized pattern converges on a pair of vertical slits.



a)

**Type A : One slit in Quadrant 1**

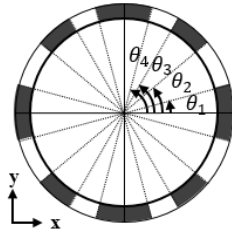


Object function :  $\min \left[ \frac{I_{yy}}{I_{xx}} \right]$

Constraint :

- 1)  $I_{xx} \geq \beta \cdot I_{xx0}$
- 2)  $I_{yy} < I_{xx}$
- 3)  $\pi/2 \geq \theta_2 > \theta_1 \geq 0$

**Type B : Two slits in Quadrant 1**



Object function :  $\min \left[ \frac{I_{yy}}{I_{xx}} \right]$

Constraint :

- 1)  $I_{xx} \geq \beta \cdot I_{xx0}$
- 2)  $I_{yy} < I_{xx}$
- 3)  $\pi/2 \geq \theta_4 > \theta_3 > \theta_2 > \theta_1 \geq 0$

b)

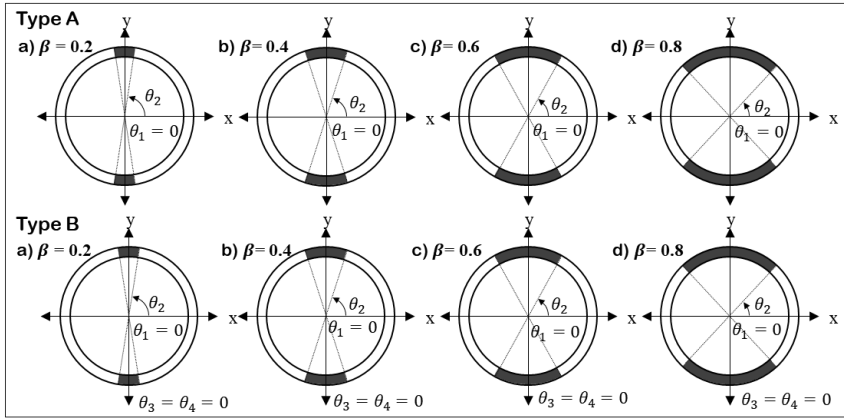


Fig. 3.2. a) The cross section of the patterned tubes of Type A and Type B, b) the optimized patterns according to the constraints where  $\beta \in \{0.2, 0.4, 0.6, 0.8\}$ . The white part stands for the non-patterned section while the black part stands for the patterned section.

Table 3.2. The optimized patterns for Type A and B

		a) $\beta = 0.2$	b) $\beta = 0.4$	c) $\beta = 0.6$	d) $\beta = 0.8$
Type A	$(\theta_1, \theta_2)$	$(0^\circ, 80.92^\circ)$	$(0^\circ, 71.36^\circ)$	$(0^\circ, 60.54^\circ)$	$(0^\circ, 46.60^\circ)$
	$\gamma = I_{xx}/I_{yy}$	119.1	27.95	10.96	4.866
Type B	$(\theta_1, \theta_2, \theta_3, \theta_4)$	$(0^\circ, 80.92^\circ, 0^\circ, 0^\circ)$	$(0^\circ, 71.36^\circ, 0^\circ, 0^\circ)$	$(0^\circ, 60.54^\circ, 0^\circ, 0^\circ)$	$(0^\circ, 46.60^\circ, 0^\circ, 0^\circ)$
	$\gamma = I_{xx}/I_{yy}$	119.1	27.95	10.96	4.866

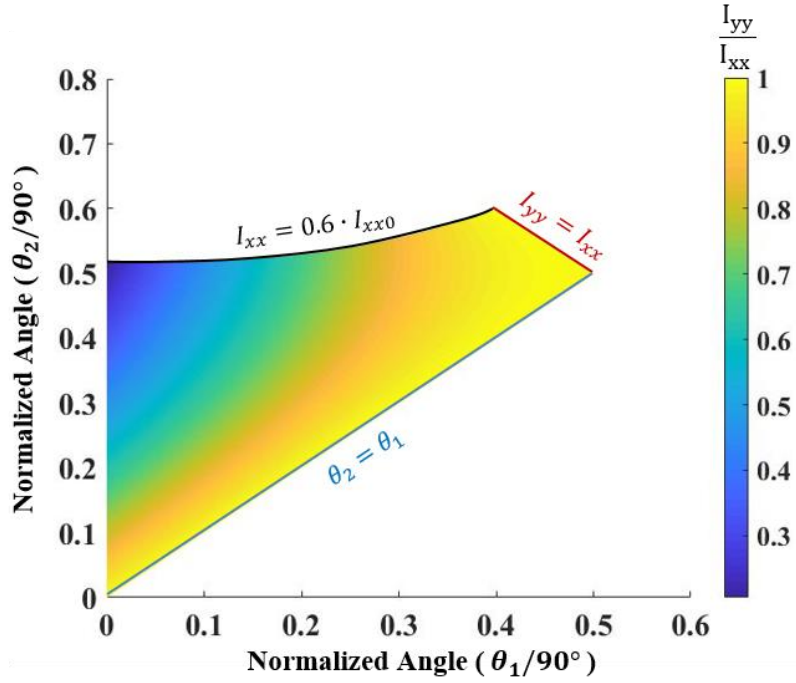


Fig. 3.3. The change of  $I_{yy}/I_{xx}$  ratio according to  $\theta_1$  and  $\theta_2$  values when  $\beta = 0.6$

## 3.2 Design Parameters of Pattern

Based on the results of chapter 3.1, the optimized pattern should have a pair of longitudinal slits that are symmetrical to the origin. As illustrated in Fig.3.4, I determined the design parameters for optimized pattern:  $\theta_h$  (angle of slit part)  $\theta_n$  (angle of non-slit part),  $L_s$  (segment length),  $L_h$  (slit length), and  $L_o$  (offset length), where  $\theta_h + \theta_n = \pi$  and  $L_s = 2L_o + L_h$ . Additionally,  $L_o$  was equal to  $0.1 \cdot L_s$  and if  $0.1 \cdot L_s$  is smaller than  $0.2\text{mm}$ ,  $L_o$  was set to have  $0.2\text{mm}$ . Thus, there are two major design parameters:  $\theta_h$  and  $L_h$ . They are significant to determine the ratio,  $I_{yy}/I_{xx}$ , and to avoid buckling, discussed in the section 3.4.

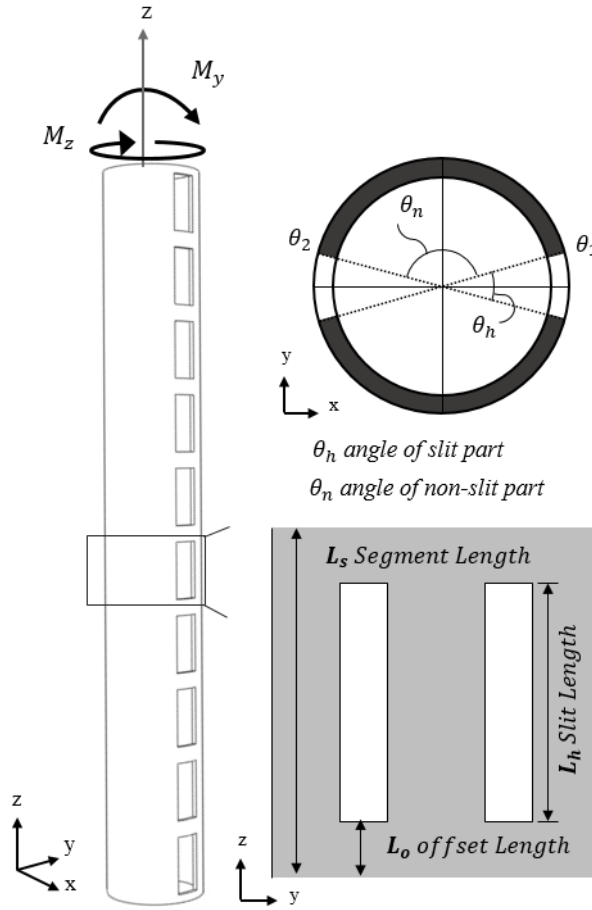


Fig. 3.4. The design parameters for the pattern of the variable stiffness mechanism

### 3.3 The Variation of Flexural Stiffness

#### 3.3.1 The Analytic Modeling for Flexural Stiffness

For given pattern design as Fig. 3.4, the analytic modeling of the cross-section for  $I_{xx}$  and  $I_{yy}$  are below. Consider the unpatterned section to model  $I_{xx}$  and  $I_{yy}$  where  $d_o$  and  $d_i$  stand for the outer and inner diameter, respectively. The stiffness of the mechanism is decided by the geometric configuration of the tubes. The stiffness of a tube can be modeled as the sum of the stiffness of each section radially divided by a specific central angle. Each section has second moment of area,  $I_{xx}$ , and it is a dominant factor to determine the flexural stiffness of the mechanism like section 2.1.2. Additionally, the patterned section has zero of young's modulus due to material removal. Assume that a tube is radially divided by patterned section ( $E_p = 0$ ) and non-patterned section ( $E_u = E$ ), the flexural stiffness of the tube can be represented as (27).

$$(EI)_{tube} = \sum(E_p I)_i + \sum(E_u I)_i = \sum(EI)_i \quad (27)$$

The second moment of area along x and y axes,  $I_{xx}$  and  $I_{yy}$ , and their ratio can be expanded as follows.

$$\begin{aligned} I_{xx} &= \int y^2 dA = \int_{\frac{d_i}{2}}^{\frac{d_o}{2}} 2 \cdot \int_{\theta_1}^{\theta_2} (r \sin \theta)^2 r d\theta dr \\ &= \frac{d_o^4 - d_i^4}{32} \left[ \theta_2 - \theta_1 - \frac{1}{2} (\sin(2\theta_2) - \sin(2\theta_1)) \right] \quad (28) \end{aligned}$$

$$\begin{aligned}
I_{yy} &= \int x^2 dx = \int_{\frac{d_i}{2}}^{\frac{d_o}{2}} 2 \cdot \int_{\theta_1}^{\theta_2} (r \cos \theta)^2 r d\theta dr \\
&= \frac{d_o^4 - d_i^4}{32} \left[ \theta_2 - \theta_1 + \frac{1}{2} (\sin(2\theta_2) - \sin(2\theta_1)) \right] \quad (29)
\end{aligned}$$

$$\frac{I_{xx}}{I_{yy}} = \frac{\theta_2 - \theta_1 - \frac{1}{2} (\sin(2\theta_2) - \sin(2\theta_1))}{\theta_2 - \theta_1 + \frac{1}{2} (\sin(2\theta_2) - \sin(2\theta_1))} \quad (30)$$

For double or multiple tubes mechanism,  $I_{xy}$  becomes zero when (16) in section 2.1.4 is satisfied. Then, from (28)~ (30) should be satisfied to have  $I_{xy} = 0$ . To have pure in-plane deformation,  $\theta_h$  for the inner and outer tube should be determined to satisfy (31).

$$\frac{D_o^4 - D_i^4}{d_o^4 - d_i^4} = \frac{\sin(\theta_{h, inner})}{\sin(\theta_{h, outer})} \quad (31)$$

### 3.3.2 The FEM Simulation for Flexural Stiffness

The FEM simulation is studied according to design parameters. The load test was performed in Abaqus 6.14 as  $\theta_h$  and  $L_h$  change for the dual tube structure of 150mm length. The load-deflection plot was demonstrated for  $\theta_h$  of 30, 60, 90, 120 degree and  $L_h \in \{0.1, 0.2, 0.3 \dots 5mm\}$ . The offset,  $L_0$ , was given as 0.5mm. Fig. 3.5 demonstrates the stiffness max/min ratio while changing the design parameters of the pattern. The ratio increased when  $\theta_h$  increased. It needs to find optimized  $L_h$  to

have maximum value of the ratio  $I_{xx}/I_{yy}$  . To consider only linear deformation region, the load of 80g, 50g, 30g, and 10g is weighted at the tip of the structure which  $\theta_h$  is 30, 60, 90, and 120 degree, respectively.

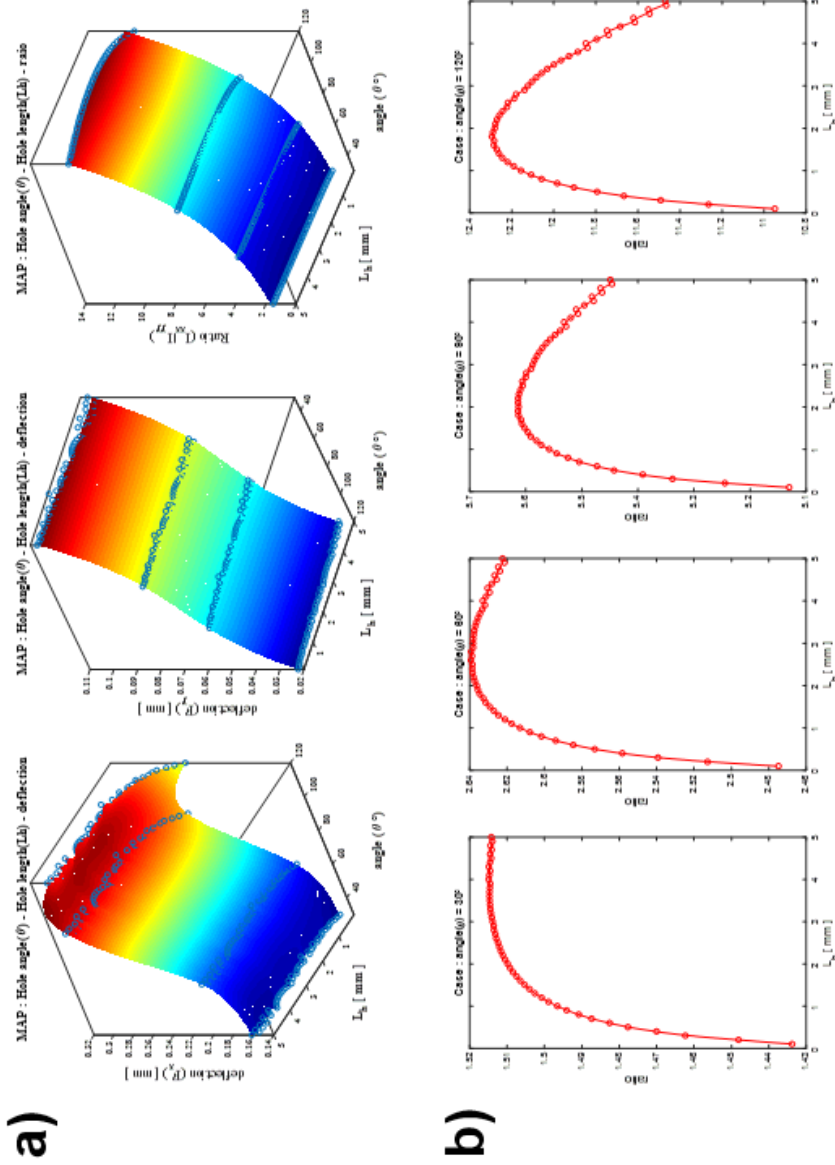


Fig. 3.5. a) From the left, the deflection map along x direction, the deflection map along y direction, and the stiffness ratio  $I_{xx}/I_{yy}$  map according to the design parameters,  $L_h$  and  $\theta_h$ , b) The stiffness ratio  $I_{xx}/I_{yy}$  according to  $L_h$  when  $\theta_h \in \{30^\circ, 60^\circ, 90^\circ, 120^\circ\}$  from the left.



## 3.4 Buckling Analysis

### 3.4.1 Mechanics Model of the Steerable Needle

A steerable needle with asymmetric bevel tip follows along an arc when it invades into elastic tissue with constant insertion speed. When considering the energy during insertion without rotation, there are energies associated with needle bending and needle-tissue interaction like Fig. 3.6. [60], [61] Needle bending energy consists of pure needle bending energy and bending energy due to axial load. The tube has very small cross section normal to axial load, so (32)>>(33).

$$\text{Pure Needle Bending: } U_B = \frac{EI}{2} \int_0^{l_i} \left( \frac{d^2 y_i}{dx^2} \right)^2 dx \quad (32)$$

$$\text{Bending due to axial load: } U_p = \frac{1}{AE} \int_0^{l_i} P^2 dx \quad (33)$$

The needle-tissue interaction energy consists of the energy due to compression of the elastic medium at the needle tip ( $U_c$ ) and the energy due to interaction of the elastic medium along the needle shaft ( $U_T$ ).

$$U_c = (\text{bulk modulus}) * \left( \frac{\Delta V}{V} \right)^2 \quad (34)$$

$$U_T = \frac{1}{2} \int_0^{l_1} K_T (y_1 - y_{c_i})^2 dx \quad (35)$$

The amount of the elastic medium at the need tip is relatively very small to the amount of compressed elastic medium along the needle shaft, so (34)<<(35).

The work done to the system can be divided by three. The work done by transverse tip load,  $W_Q$ , as (36), the work done by axial tip load,  $W_P$ , as (37), and the work done to rupture the elastic medium,  $W_R$ , as (38) where the amount effective rupture toughness is  $G_C$ , and the amount of tear or rupture is  $a$ .

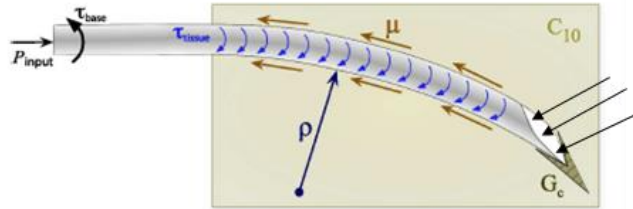
$$W_Q = Qy(l_i) \quad (36)$$

$$W_P = \int_0^{l_i} \frac{P}{2} \left( \frac{dy_i}{dx} \right)^2 dx \quad (37)$$

$$W_R = aG_C l_i \quad (38)$$

Misra et al. demonstrated that the (32) and (35) were the major contribution to the system energy [60]. Especially, from 0 to 60mm of the insertion, pure needle bending weighted more than 80% of the total energy.

a)



b)

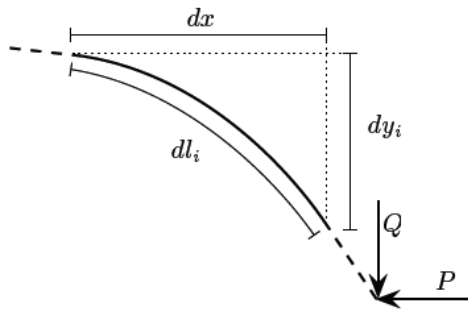


Fig. 3.6. a) The mechanics of steerable needle inserting into elastic medium, b) the free body diagram at the distal tip [50]

### 3.4.2 Bending and Torsional Buckling Analysis

As 3.4.1., in the steerable needle insertion system, the pure bending energy of the needle contributes most. Also, in vitro test using duty cycle method [62], the needle's rotational speed of 120rpm is applied. The substantial friction forces to the needle shaft, resulting in a lag of over  $45^\circ$  for a 10 cm insertion depth in some phantoms and during a prostate brachytherapy, it is reported that torsion causes a  $10\text{--}15^\circ$  discrepancy in human tissues.[63]

Partial material removal reduces both bending and torsional stiffness so that it is required to have reference of buckling condition of bending and torsional direction. Especially, it is significant to avoid buckling in surgical procedures since single undesired motion may cause fatal injury to patients.

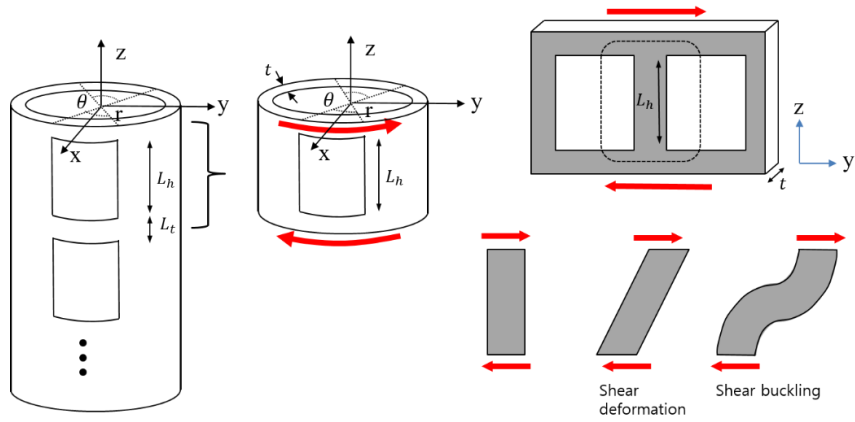
As the steerable needle's circumstance is under high torsional friction and high bending moment, the two types of buckling are studied. One is the buckling caused by twist moment( $M_z$ ) as Fig. 3.7a. and the other is caused by bending moment( $M_y$ ) as Fig. 3.7b. In the simulation, to find buckling threshold,  $M_y$  and  $M_z$  are incrementally increased until the energy suddenly drops. The structure becomes extremely unstable if  $\theta_h$  is larger than  $120^\circ$  or  $L_h$  is too long. Thus, the study is performed for  $\theta_h \in \{0^\circ, 5^\circ, 10^\circ, \dots 120^\circ\}$  and  $L_h \in \{0.5\text{mm}, 1.0\text{mm}, 1.5\text{mm}, \dots 9\text{mm}\}$ . In order to map the buckling thresholds according to the design parameters, 450 ( $25 \times 18$ ) cases are examined per specimen. As they are most used materials for surgical instruments, I chose stainless steel and nitinol tubes for the analysis.

The stainless steel tube has  $d_0 = 1.83$  mm,  $d_i = 1.51$  mm, tube thickness = 0.16 mm, and  $E = 188\text{GPa}$ . Two types of the nitinol tubes were analyzed. Type I has  $d_0$

= 2.0 mm,  $d_i = 1.8$  mm, tube thickness = 0.1 mm, and  $E = 67.6$  GPa. Type II has  $d_0 = 2.40$  mm,  $d_i = 2.20$  mm,  $t = 0.1$  mm, and  $E = 51.3$  GPa.

Fig. 3.8 demonstrates the map of  $M_y$  and  $M_z$  buckling thresholds as  $\theta_h$  and  $L_h$  change. Finally, Fig. 3.9. plots the stable and unstable area according to  $M_y$  and  $M_z$  value. For example, in the graph,  $M_{y,400}$  means  $M_y=400$ Nmm. On the border line of  $M_{y,400}$  , the left side is the stable area and the right side is the unstable area when 400Nmm  $M_y$  is applied. Thus, from Fig. 3.9, the range of design parameters are determined to avoid buckling. The buckling map for the design parameters can be used to design the stiffness range for safety consideration to prevent buckling.

**a)**



**b)**

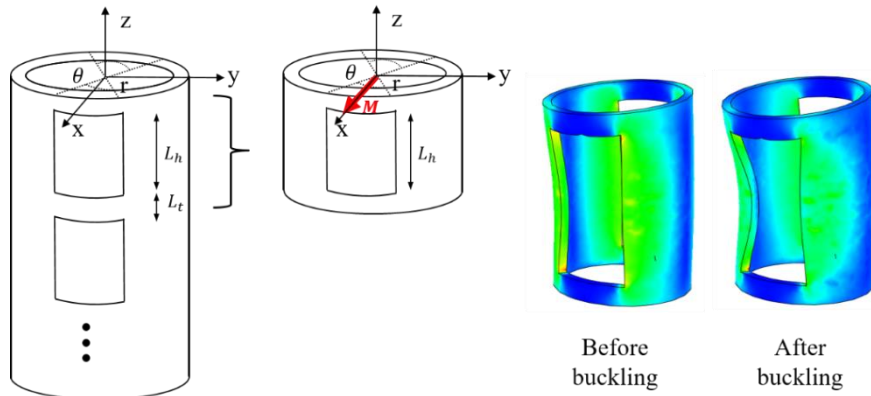


Fig. 3.7. The buckling of the patterned tube caused by a) twist moment ( $M_z$ ) and b) bending moment ( $M_y$ )

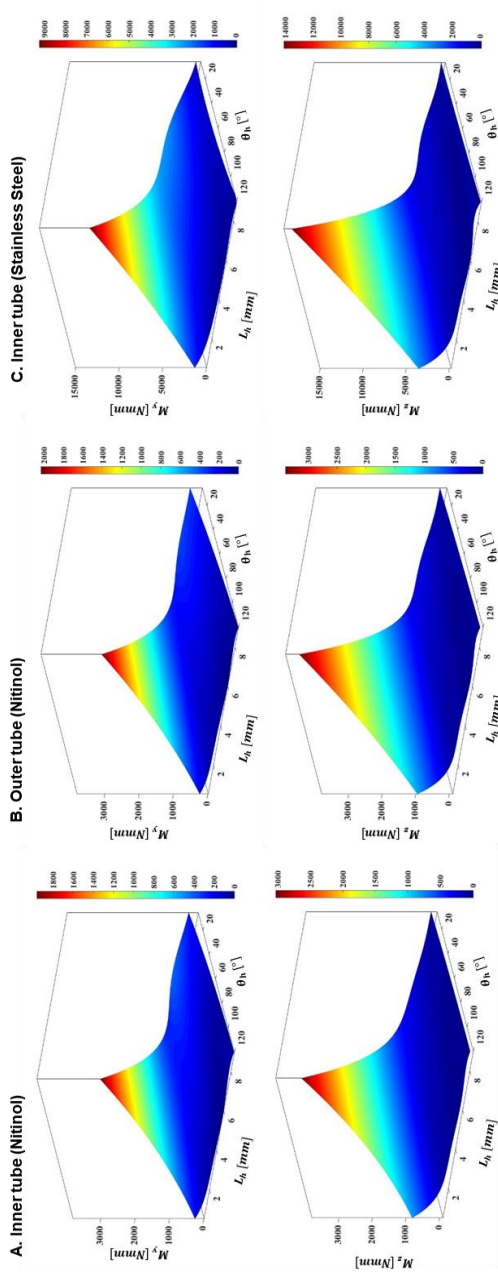


Fig. 3.8. The map of  $M_y$  (bending moment) and  $M_z$  (twist moment) thresholds to avoid buckling according to  $\theta_h$  and  $L_h$  for A) the nitinol inner tube, B) the nitinol outer tube, and C) the stainless steel inner tube.

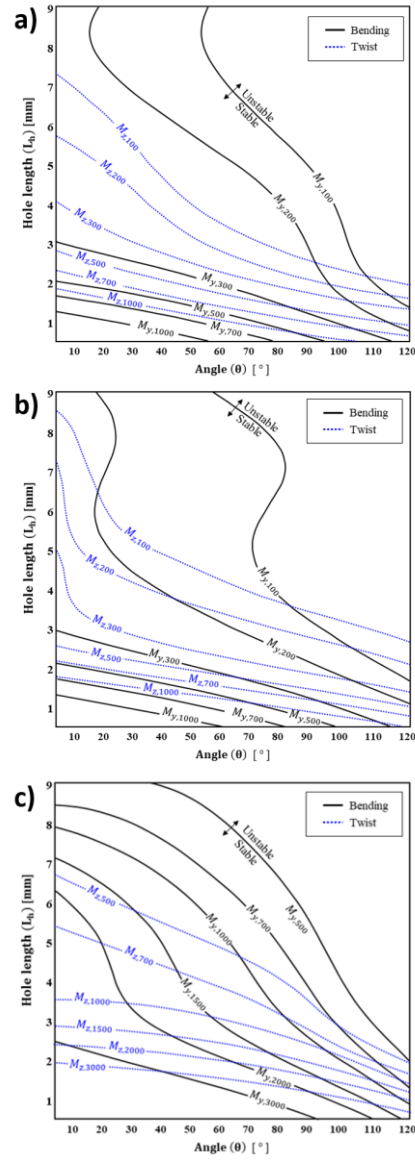


Fig. 3.9. The stable and unstable area of the design parameters,  $\theta_h$  and  $L_h$ , according to the given bending/twist moment values for a) the nitinol inner tube, b) the nitinol outer tube, and c) the stainless steel inner tube



### 3.5 Experimental Verification

To find the consistency between experiment and simulation, I fabricated ten types of patterned stainless steel tube as Table 3.3. using UV laser machining. For precise manufacturing, picosecond UV laser is employed rather than nanosecond UV laser. Picosecond pulse width UV laser has higher intensity and less heat affected zone compared to nanosecond pulse width laser. The manufacturing system is similar to section 2.2. The rotational stage holds tube specimen while laser scanner controls the laser spot as Fig. 3. 10a. Also, the glass zig is utilized to enhance the alignment between laser spot and tube as Fig 3.10b. The tubes were engraved with pulse width 7ps, 355nm wavelength, repetition rate of 15kHz, scanner speed of 100mm/s, and path repetitions of 30 times. As results, the patterned tube is manufactured as Fig. 3.11. The photos were taken by telecentric lens with monochrome image sensor for better resolution.

The patterned tubes were examined by three point bending test at rotational angle 0 and 90 degree by using Instron 5966 series (Fig. 3.12a). Also, the three point bending test was also performed by FEM simulation using Abaqus (Fig. 3.12b). The comparison between simulation and experiment is listed in Table 3.4. The average error is 3.01% and its standard deviation is 9.21. The results show the consistency between simulation and experiment.

Table 3.3. The pattern design parameters for the experiment

$\theta_h$	30°			60°			90°		120°	
$L_h$ (mm)	1	2	4	1	2	4	1	2	1	2
$L_o$ (mm)	0.2	0.25	0.5	0.2	0.25	0.5	0.2	0.25	0.2	0.25
$L_s$ (mm)	1.4	2.5	5	1.4	2.5	5	1.4	2.5	1.4	2.5

a)



b)

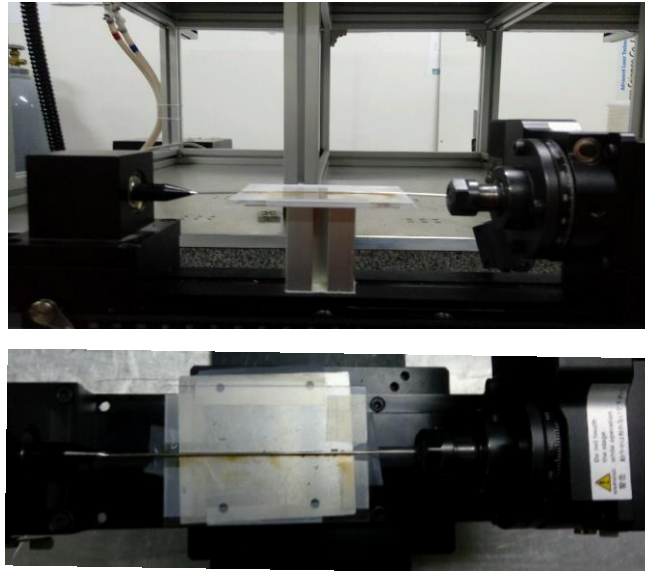


Fig. 3.10. a) The picosecond UV laser machining system to manufacture the patterned tubes, b) the glass jig installation for precise alignment during the manufacturing process of the tubes with diameters of 1 *mm* or less

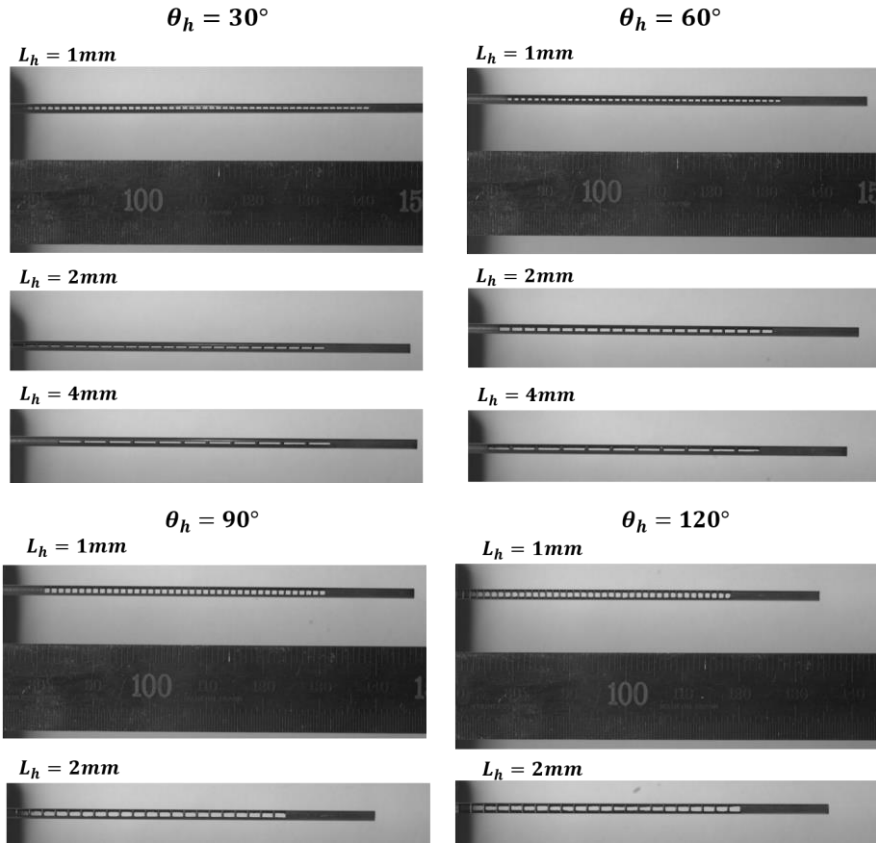


Fig. 3.11. The patterned tubes by picosecond UV laser machining according to design parameters,  $\theta_h$  and  $L_h$

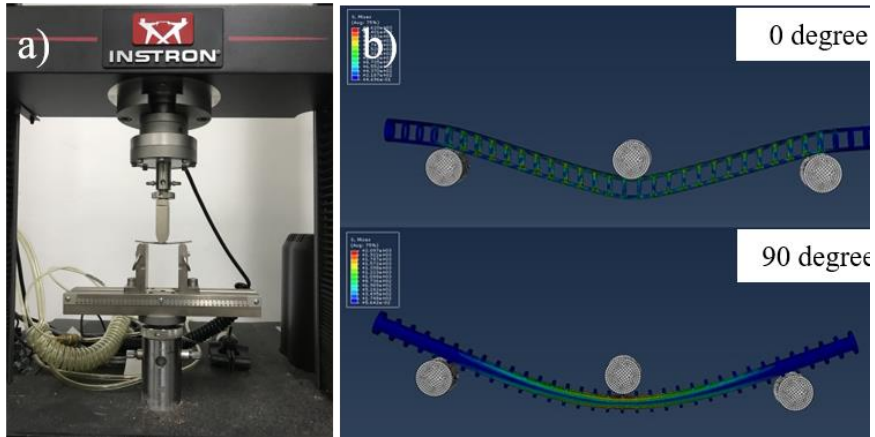


Fig. 3.12. a) The experiment on three point bending test using Instron 5900 series and b) the FEM simulation of three point bending test using Abaqus 6.14.

Table 3.4. The comparison of three point bending test  
between the FEM simulation and the experiment

#	1	2	3	4	5	6	7	8	9	10
$\theta_h, L_h(^{\circ}, mm)$	(30, 1)	(30, 2)	(30, 4)	(60, 1)	(60, 2)	(60, 4)	(90, 1)	(90, 2)	(120, 1)	(120, 2)
Ixx/Iyy (FEM)	1.327	1.244	1.209	1.578	1.475	1.504	2.209	1.968	4.164	3.524
Ixx/Iyy (Experiment)	1.313	1.189	1.255	1.628	1.486	1.515	2.160	2.206	4.286	3.539

### 3.6 Pattern Optimization Process according to Application

Using topology optimization and analysis, the pattern shape and design parameters were determined as Fig. 3.4. The pattern can be optimized according to the requirements of the target application. 1) At first, the target application determines the required minimum stiffness and the maximum bending/torsional moments during target application. 2) Based on the minimum stiffness, the constraint coefficient  $\beta$  for  $I_{xx} \geq \beta \cdot I_{xx0}$  is determined, and the condition for the angle of slit,  $\theta_h$ , is given accordingly. 3) Additionally, depending on the buckling analysis map like Fig. 3.8 and Fig. 3.9, one can determine the conditions of  $\theta_h$  and  $L_h$  to avoid buckling for given bending/torsional moments. 3) Lastly, one can determine the design parameters,  $\theta_h$  and  $L_h$  to have desired variable stiffness range while satisfying the constraints. The determined parameters are able to be examined by FEM simulation. Fig 3.13. demonstrates the flow chart to determine the pattern design parameters according to target application and constraints.

The variable stiffness mechanism utilizes physically embodied intelligence [64] and is applicable to continuum robot with smaller dimension ( $\phi 3\text{mm}$  or less). Furthermore, the analytic model was built for stiffness control in chapter 2 and 3 and the pattern optimization process was established in chapter 3. The variable stiffness mechanism can be integrated to various minimally invasive surgical instruments. In chapter 4, the pattern design optimization is applied to steerable needle.

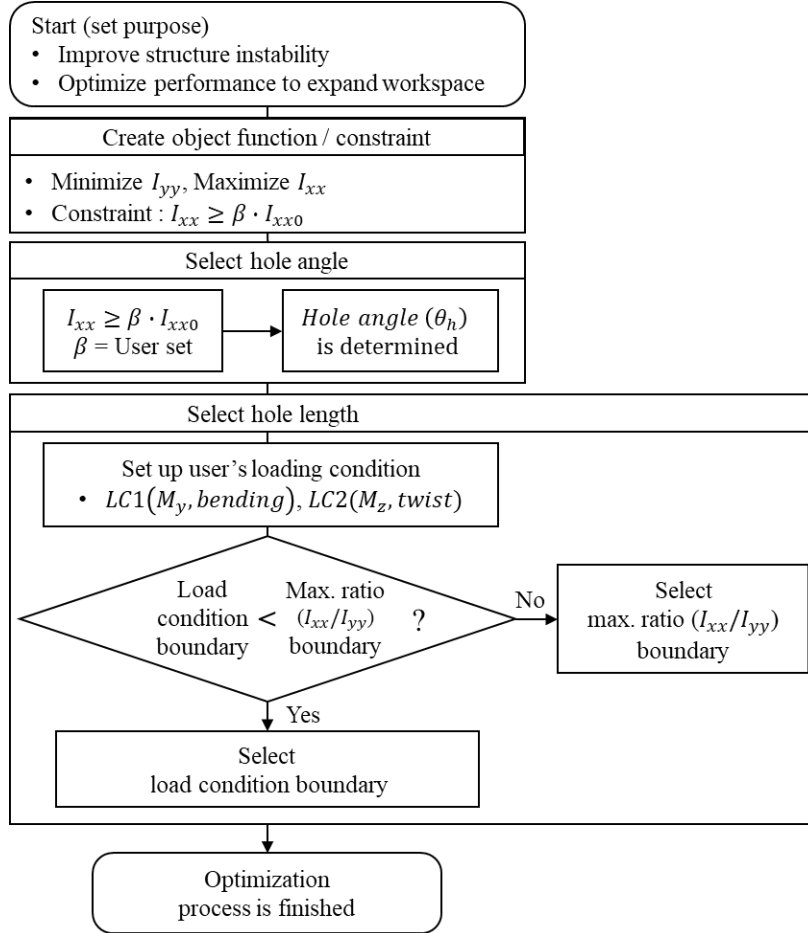


Fig. 3.13. The flow chart to determine pattern design parameters for the variable stiffness mechanism according to the target application and the constraints

## **Chapter 4 Stiffness-controlled Steerable Needle**

The proposed variable stiffness mechanism was applied to the steerable needle to provide an additional degree of freedom to control the needle's trajectory. I modeled kinematic modeling for the stiffness-controlled steerable needle and the relationship between the flexural stiffness of the needle and the curvature of the needle's trajectory. Based on the kinematic model, the stiffness-controlled needle can control its trajectory to avoid anatomic obstacles, and can reduce unreachable area compared to conventional steerable needles.

### **4.1 The Current Steerable Needle Mechanisms**

Needle-based interventions have been one of the most general invasive surgical procedures used for tissue sample removal as well as drug delivery from deep within the body. The needle's small dimension enables itself to access subsurface targets while inflicting minimal damage to nearby tissues. Furthermore, its lumen provides a conduit through which to deliver a wide variety of therapeutic deliveries and diagnostic instruments such as brachytherapy, thermal ablation, and biopsy. As sensors, manipulators, and end-effector instruments get smaller, applications for needle-based interventions have been expanding.

Most of all, the distal tip's targeting accuracy is significant for needle-based interventions. For example, inaccurate needle placement causes malignancies not being detected during biopsy, radioactive seeds to destroy healthy instead of cancerous tissues during brachytherapy [65], and traumatic effects while performing anesthesia. To improve the accuracy of the needle-based interventions, the image-



guided robotic systems are currently used with magnetic resonance imaging [66], [67], ultrasound imaging [57], [68]–[71], or multi-imaging modalities [72]. Nevertheless, there are still many components to deviate the needle from its intended path: the inhomogeneity of tissue, the deformation of organs, respiration, and flow of fluids in human body. A robotically steered needle can be a solution to mitigate such targeting errors during the intervention to subsurface targets.

The robotically steered flexible needles through tissue have been researched in various groups [1], [56], [73]–[78]. Planning such procedures requires an accurate model of the needle-tissue interaction. The needle with standard bevel tips causes itself to bend when interacting with soft tissue. The asymmetry of the bevel edge results in bending forces at the distal tip [1], [56], [79]. By rotating the needle about its axis, the needle re-orientes the direction of subsequent bending. The airfoil tips are utilized to increase the area of a bevel tip to control the degree of the curvature [80]. The pre-bent [64] or curved [73] needles vary with the length and angle of the asymmetry to vary the curvature. Alternatively, several studies have demonstrated lateral manipulation [74], [76] that is moving the base of needle perpendicular to the insertion axis, and manipulating the tissue in order to move the target into the needle's trajectory [81], [82].

The needle's behavior is also based on the geometries and material properties of the interacting tissue. Researchers have studied the physics-based interaction models between needle and soft tissue [83]–[89] to render simulation of the interaction for real-time applications. Additionally, researchers have performed the observation and the experimental measurement for the forces due to puncture, cutting, and friction against nearby tissue during needle intervention procedures [90], [91].

Overall, researchers have studied various methods to enhance the accuracy of the steerable needle control. The needle trajectory is generally controlled by two input

variables, the insertion speed and the rotation speed of needle. The needle insertion speed is changed to control the degree of curvature [1]. The faster the needle insertion speed, the larger the curvature becomes. However, the faster the insertion speed is, the more likely the needle causes injury to the patient. Because the insertion speed change cannot be performed discretely, there is an acceleration area that degrades the accuracy of the distal tip control. Furthermore, in most cases, the needle insertion distance is less than 150 mm, so it is difficult to change the curvature of the needle trajectory much. Also, the needle's rotating speed is able to be duty cycled in order to control the curvature of the needle's trajectory [92], [93]. However, the duty-cycle algorithm using frequent rotation of the bevel-tip needle causes relatively large damage to nearby tissues. Thus, to ensure safety and minimize invasiveness, it is required to have curvature-controlled algorithm while limiting the insertion and rotation speed of the needle.

To fulfill such requirements, I applied the proposed variable stiffness mechanism in chapter 2 and 3 for the steerable needle. The stiffness-controlled steerable needle can vary the curvature of the needle's trajectory while limiting the insertion and rotation speed of the needle. Also, the mechanism can be used to reduce unreachable area during needle intervention. The curvature is inherently limited by the combined mechanical properties of the needle and tissue. On the other hand, the proposed stiffness controlled needle has an anisotropic distribution of bending stiffness along the radial direction, so the range of curvature is widened and the curvature can be controlled by changing its configuration. The following sections explain the mechanism and its control.

## **4.2 The Mechanism of Stiffness-Controlled Steerable Needle**

The variable stiffness mechanism of chapter 2 and 3 is able to enhance the functionality of steerable needle: 1) steering the needle's direction with less damage to surrounding tissues, 2) widens the curvature range of the needle's trajectory to reduce unreachable area, and 3) increasing safety by limiting the low insertion/rotation speed of the needle.

By applying the variable stiffness mechanism to steerable needle, I added the stiffness control as an additional control input for the needle's trajectory. As the mechanism varies the needle's stiffness continuously with instantaneous response time, the curvature of the needle trajectory can be controlled. It is possible to use the inner tube rotation to change the stiffness, so it minimizes damage to surrounding tissues compared to the current steerable needles.

Furthermore, it is expected to increase safety as the curvature of trajectory can be changed while limiting the insertion speed. In the proposed mechanism, the curvature can be controlled by stiffness change rather than insertion speed change. As mentioned in section 4.1, insertion speed is not efficient variable because high speed can cause a fatal injury to patients and insertion distance is not long enough.

The proposed stiffness-controlled steerable needle was composed of two coaxially assembled tubes. The outer tube was unpatterned tube with bevel-tip of 45 degrees. The inner tube was asymmetric patterned tube. The outer tube rotation determined the direction of the bevel tip while the inner tube rotation determined the stiffness of the needle along certain direction.

For both inner and outer tube, the material type and thickness can be chosen to optimize variable stiffness capabilities and, at the same time, to be stiff enough to endure loads during operation and avoid buckling. The pattern for the inner tube can be determined through the optimization process by section 3.5.

In this study, the outer tube was nitinol ( $E = 51.3 \text{ GPa}$ ) having an outer diameter of 2.0 mm and an inner diameter of 1.8 mm. The inner tube was stainless steel ( $E = 188 \text{ GPa}$ ) having an outer diameter of 1.65mm and an inner diameter of 1.35mm. The inner tube was laser patterned to have the anisotropic distribution of the flexural stiffness according to radial direction. Fig. 4.1 represent the bevel-tip outer tube and the patterned inner tube. Since the outer tube was nitinol (low rigidity) and the inner tube was stainless steel (high rigidity), the variable stiffness effect became large. The range of variable stiffness can be customized according to material selection, the inner and the outer tube's dimension (diameter, thickness), pattern of the inner tube.

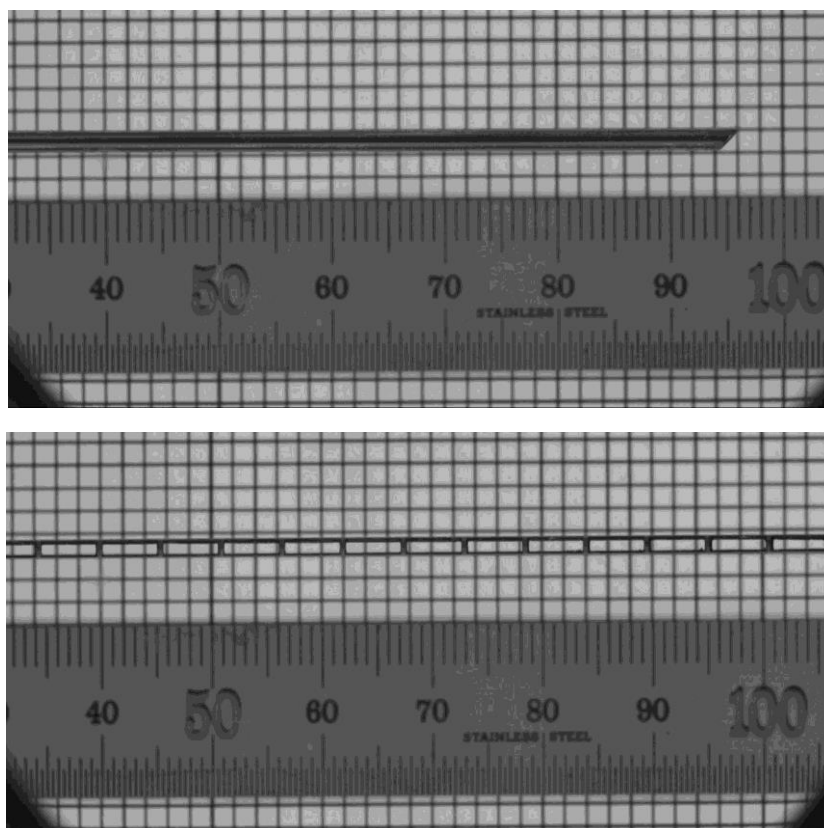


Fig. 4.1. The outer tube with the bevel-tip (upper) and the inner tube with the patterns (lower) of the steerable needle

## 4.3 Steerable Needle Control

### 4.3.1 The Radius of Curvature of Needle's Trajectory

According to the needle-tissue interaction model in [60]. The curvature of a bevel-tip needle is a function of the following parameters.

$$\kappa = f(E, I, \alpha, C_{10}, G_c, \mu, u_1) \quad (39)$$

At first,  $E$ , the needle's Young's modulus,  $I$ , second moment of inertia, and  $\alpha$ , tip bevel angle are the properties of the needle. Secondly,  $C_{10}$ , the tissue's nonlinear material property,  $G_c$ , rupture toughness, and  $\mu$ , and coefficient of friction are the properties of the tissue. Lastly,  $u_1$  is the needle insertion speed. Different from general steerable needle, not only  $u_1$  but also  $I$  can be a control variable in this stiffness-controlled steerable needle.

$E$  and  $\alpha$  are constant over time and  $C_{10}$ ,  $G_c$ ,  $\mu$  are given by circumstances.  $I(t)$  and  $u_1(t)$  can be expressed by the function of time. High speed of  $u_1(t)$  is dangerous and  $u_1(t)$  has acceleration region when changing its speed to cause errors of kinematic model. Plus, a steerable needle is used in prostate brachytherapy, which distance to surgical site is less than 150mm. In this context,  $I(t)$  can be more safe and provide wider workspace rather than  $u_1(t)$ .

### 4.3.2 Bi-cycle Nonholonomic Model for Steerable Needle

In the steerable needle system, the final state of the system depends on the intermediate values of its trajectory. The steerable needle is the system whose state

depends on the path taken and cannot be represented by a conservative potential function. Thus, let kinematic nonholonomic system represent the steerable needle system. Webster et al. fits the trajectory of the steerable needle using nonholonomic modeling with the needle insertion speed and rotation speed as control variables [1]. I model the stiffness-controlled needle's trajectory with additional control input, stiffness, by nonholonomic modeling.

At first, consider a bevel-tip needle driven with two velocity inputs and one stiffness input: insertion speed and rotation speed; the flexural stiffness of the needle along the bevel-tip direction. I propose a variant of the standard kinematic bicycle, with constant front wheel angle,  $\phi$ , and wheel base,  $l_1$ , as depicted in Fig. 4.2. The curvature,  $\kappa$ , of the needle path, is determined by the stiffness along bending direction. A second parameter,  $l_2$ , determines the location along the bicycle that is attached to the needle tip,  $n(t)$ .

There are assumptions in Fig. 4.2. Frame A is the global coordinate; Frame B and C represent for the first and the second wheels, respectively; The center of the frame C and the needle tip are on the z axis of frame B; The z-axis of frame C has  $\phi$  difference against the z-axis of frame B; Frame B and C have constant location each other during pure needle insertion;  $\mathbf{u}_1$  =pure needle insertion speed along z axis of frame B;  $\mathbf{u}_2$  =pure shaft rotation along z axis of frame B;  $\kappa$  =curvature of needle trajectory at  $\mathbf{u}_1=1\text{mm/s}$ ;  $l_1 \neq 0$  and  $\phi \in \left(0, \frac{\pi}{2}\right)$ . Notice that  $\kappa$  changes as stiffness varies according to the rotational configuration of the inner tube.

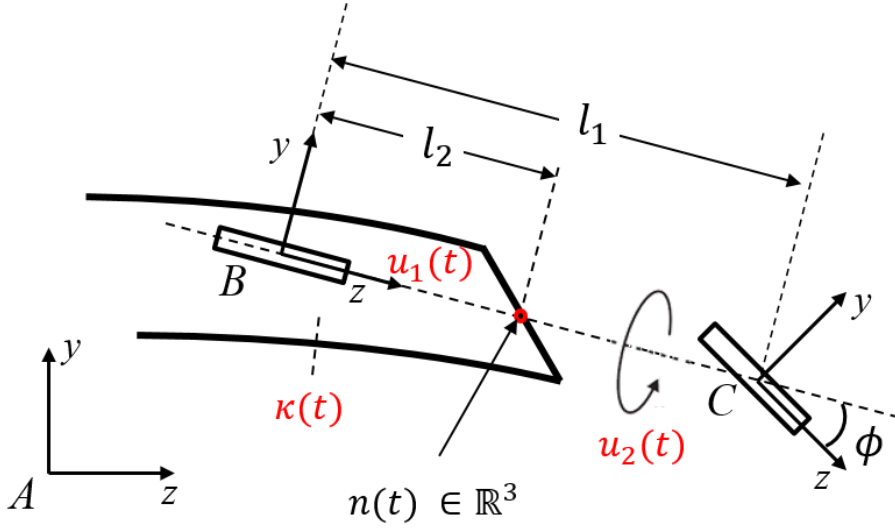


Fig. 4.2. The diagram of the bi-cycle nonholonomic modeling for the trajectory of the stiffness-controlled steerable needle, derived from [1]

Additionally, consider Pfaffian constraints of the system. The velocity of the origin of frame B cannot have a projection along the  $x$  and  $y$  axes of frame C.

$$e_1^T v_{ab} = 0 \quad (40)$$

$$e_2^T v_{ab} = 0 \quad (41)$$

The velocity of the origin of frame C cannot have a projection along the  $x$  and  $y$  axes of frame C.

$$e_1^T v_{ac} = 0 \quad (42)$$

$$e_2^T v_{ac} = 0 \quad (43)$$

The frame B and C are fixed with respect to each other  $\Rightarrow V_{bc} = 0$

Then,  $V_{ac} = Ad_{g_{bc}^{-1}} V_{ab} + V_{bc} = Ad_{g_{bc}^{-1}} V_{ab}$



$$Ad_{g_{bc}} = \begin{bmatrix} R_{bc} & \hat{P}_{bc} R_{bc} \\ 0 & R_{bc} \end{bmatrix} = \begin{bmatrix} e^{\hat{e}_1 \phi} & l_1 \hat{e}_3 e^{\hat{e}_1 \phi} \\ 0 & e^{\hat{e}_1 \phi} \end{bmatrix} \quad , \quad Ad_{g_{bc}^{-1}} = \begin{bmatrix} R_{bc}^T & -R_{bc}^T \hat{P}_{bc} \\ 0 & R_{bc}^T \end{bmatrix} =$$

$$\begin{bmatrix} e^{\hat{e}_1(-\phi)} & e^{\hat{e}_1(-\phi)} l_1 \hat{e}_3 \\ 0 & e^{\hat{e}_1(-\phi)} \end{bmatrix} \quad (44)$$

Convert Equation (40)

$$[e_1^T \ 0] V_{ac} = [e_1^T \ 0] Ad_{g_{bc}^{-1}} V_{ab} = 0 \Leftrightarrow [1 \ 0 \ 0 \ 0 \ -1 \ 0] V_{ab} = 0 \quad (45)$$

Convert Equation (41)

$$[e_2^T \ 0] Ad_{g_{bc}^{-1}} V_{ab} = 0 \Leftrightarrow [0 \ \cos \phi \ -\sin \phi \ l_1 \cos \phi \ 0 \ 0] V_{ab} = 0 \quad (46)$$

Summing up Pfaffian constraint equations (40), (41), (45), (46)

$$\begin{bmatrix} 1 & 0 & 0 & 0 & 0 & 0 \\ 0 & 1 & 0 & 0 & 0 & 0 \\ 1 & 0 & 0 & 0 & -1 & 0 \\ 0 & \cos \phi & -\sin \phi & l_1 \cos \phi & 0 & 0 \end{bmatrix} V_{ab} = 0$$

$$\Rightarrow \begin{bmatrix} 1 & 0 & 0 & 0 & 0 & 0 \\ 0 & 1 & 0 & 0 & 0 & 0 \\ 0 & 0 & 1 & -l_1/\tan \phi & 0 & 0 \\ 0 & 0 & 0 & 0 & 1 & 0 \end{bmatrix} V_{ab} = \begin{bmatrix} 1 & 0 & 0 & 0 & 0 & 0 \\ 0 & 1 & 0 & 0 & 0 & 0 \\ 0 & 0 & 1 & -1/\kappa & 0 & 0 \\ 0 & 0 & 0 & 0 & 1 & 0 \end{bmatrix} V_{ab} = 0 \quad (47)$$

Finally, Pfaffian constraints are summarized in (47).

Now, in the bi-cycle nonholonomic model, consider that spatial velocity  $V_1$  corresponds to pure needed insertion and  $V_2$  corresponds to pure shaft rotation.  $V_1$  and  $V_2$  are basis for  $V_{ab}$

$$V_1 = \begin{bmatrix} v_1 \\ \omega_1 \end{bmatrix} = \begin{bmatrix} e_3 \\ \kappa e_1 \end{bmatrix} = \begin{bmatrix} e_3 \\ 0_{3 \times 1} \end{bmatrix} + \kappa \begin{bmatrix} 0_{3 \times 1} \\ e_1 \end{bmatrix} = \begin{bmatrix} e_3 \\ 0_{3 \times 1} \end{bmatrix} + \kappa(t) \begin{bmatrix} 0_{3 \times 1} \\ e_1 \end{bmatrix} \quad (48)$$

$$V_2 = \begin{bmatrix} v_2 \\ \omega_2 \end{bmatrix} = \begin{bmatrix} 0_{3 \times 1} \\ e_3 \end{bmatrix} \quad (49)$$

Then, the kinematic model becomes

$$V_{ab} = u_1 V_1 + u_2 V_2 = u_1(t) \begin{bmatrix} e_3 \\ 0_{3 \times 1} \end{bmatrix} + u_1(t) \kappa(t) \begin{bmatrix} 0_{3 \times 1} \\ e_1 \end{bmatrix} + u_2(t) \begin{bmatrix} 0_{3 \times 1} \\ e_3 \end{bmatrix} \quad (50)$$

In other words, the kinematic model is

$$\dot{g}_{ab}(t) = g_{ab}(t)(u_1(t)\hat{S}_1 + u_1(t)\kappa(t)\hat{S}_2 + u_2(t)\hat{S}_3) \quad (51)$$

where  $S_1 = \begin{bmatrix} e_3 \\ 0_{3 \times 1} \end{bmatrix}$ ,  $S_2 = \begin{bmatrix} 0_{3 \times 1} \\ e_1 \end{bmatrix}$ ,  $S_3 = \begin{bmatrix} 0_{3 \times 1} \\ e_3 \end{bmatrix}$  and the needle tip vector

$$n(t) = R_{ab}(t)l_2 e_3 + p_{ab}(t) \quad (52)$$

Notice that the kinematic model has three control variables, insertion speed,  $u_1$ , rotation speed,  $u_2$ , and the curvature of needle's trajectory due to stiffness,  $\kappa$ . In previous literatures, Webster et al. studies the effect of insertion speed,  $u_1$ , rotation speed,  $u_2$  [1]. In this study, to observe the variable stiffness effect, let  $u_1(t) = \text{constant}$  and  $u_2(t) = 0$ . Then, the bending of needle happens in a plane.

Then, the kinematic model becomes

$$\dot{V}_{ab} = u_1 S_1 + u_1 \kappa(t) S_2 \quad (53)$$

$$\text{where } S_1 = \begin{bmatrix} e_3 \\ 0_{3 \times 1} \end{bmatrix}, S_2 = \begin{bmatrix} 0_{3 \times 1} \\ e_1 \end{bmatrix} \quad (54)$$

Set up a discrete-time model and use the experimental data to fit the parameters of the model.

In the discrete-time model, consider the homogeneous transformation,  $g_{ab}$ , along  $V_{ab}^b$  for T seconds for each time step,  $k = 0, 1, 2, \dots$

$$g_{ab}(k+1) = g_{ab}(k)e^{(u_1 \hat{S}_1 + u_1 \kappa(k) \hat{S}_2)T} \quad (55)$$

$$n(k) = R_{ab}(k)l_2 e_3 + p_{ab}(k) \quad (56)$$

Let  $T = 1$  second and  $u_1 = 6mm/s$ , then the model and needle tip vector become

$$g_{ab}(k+1) = g_{ab}(k)e^{(6\hat{S}_1+6\kappa(k)\hat{S}_2)} \quad (57)$$

$$n(k) = R_{ab}(k)l_2e_3 + p_{ab}(k) \quad (58)$$

Recall (43), Pffafian constraints for the system is

$$\begin{bmatrix} 1 & 0 & 0 & 0 & 0 & 0 \\ 0 & 1 & 0 & 0 & 0 & 0 \\ 0 & 0 & 1 & -1/\kappa & 0 & 0 \\ 0 & 0 & 0 & 0 & 1 & 0 \end{bmatrix} V_{ab} = 0 \quad (59)$$

To fit the coefficients for the nonholonomic model, the experiment was set-up with controller and observation system as Fig.4.3. The controller controls 2R-2T motion of the steerable needle. The rotational and translational movement of each tube (the inner and the outer) was controlled independently. The rotational movement was controlled by Dynamixel using RS-485 communication and the translational movement was controlled by Maxon motor using CAN communication. Each Maxon motors' rotational movement transited into translational movement through lead screw while Dynamixel rotated each tube held by collet chuck. Telecentric lens or camcorder was set to capture the motion of the distal tip of the needle.

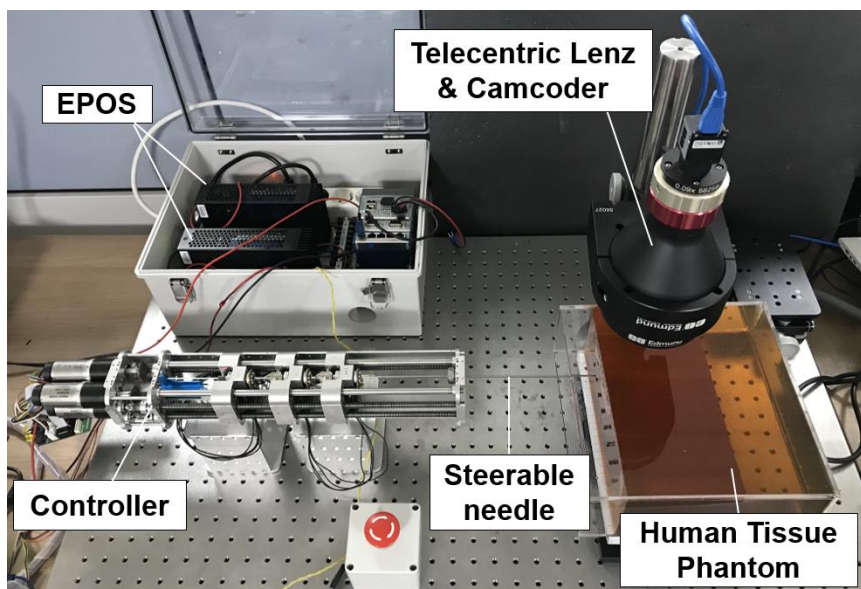


Fig. 4.3. The insertion experiment set-ups for the stiffness-controlled steerable needle

For the human tissue phantom, 80% water, 19% gelatin, 1% silica, ( $E \approx 90 \text{ kPa}$ ) to have similar elasticity as cancerous prostate ( $E \approx 96 \text{ kPa}$ ) which was one of major applications of steerable needle [57]. The composition can be changed to have different elasticity in order to test diverse material-properties phantoms [94]. Alternatively, Ultrasound-based Acoustic Radiation Force Impulse (ARFI) imaging technique is able to estimate the elasticity of the phantom tissue.

Based on the pattern design, the rotation angle  $\theta_R$  has the same configuration of  $-\theta_R$  and  $(\theta_R + 180^\circ)$ . Thus, in the experiment, steerable needle was inserted as much as 100mm when the rotational configuration of the inner tube was  $\theta_R \in \{0^\circ, 30^\circ, 60^\circ, 90^\circ\}$ . The insertion speed was constant,  $u_1 = 6 \text{ mm/s}$ , and the rotational speed was zero,  $u_2 = 0 \text{ mm/s}$  during the experiment.  $T = 1 \text{ s}$  for the discrete-time model. The needle insertion experiment was performed 10 times per rotational configuration to fit  $l_2$  and  $\kappa$ . When changing the rotational configuration to vary the stiffness, assume that only  $\kappa$  changes while  $l_2$  does not. The distal tip position of needle was tracked and the least-square method was applied.  $l_2$  is 2.374mm and  $\kappa$  is given as Table 4.1. The results of the needle insertion experiment were shown in Fig. 4.4. As expected, the lower stiffness along the bending direction was, the higher curvature became. The rotational configuration of the inner tube determined the flexural stiffness, and the tendency of  $\kappa$  can be induced from the energy-based model formulation incorporating tissue interactions, needle geometric and material properties. Additionally, Fig. 4.5. represents the bicycle model trajectory and the standard deviation bar from the experiment. The noise to input parameters can be considered using the stochastic model [95], [96]. Thus, from the rotational configuration of the stiffness-controlled steerable needle, the curvature of the needle trajectory can be controlled.

Table 4.1. The coefficients for bi-cycle nonholonomic kinematic model

Rotated angle, $\theta_R$	0°	30°	60°	90°
Needle Stiffness, EI ( $kN \cdot mm^2$ )	20.6	31.9	54.5	65.8
The Curvature of the Trajectory, $\kappa$ ( $mm^{-1}$ )	0.00330	0.00251	0.00197	0.00169

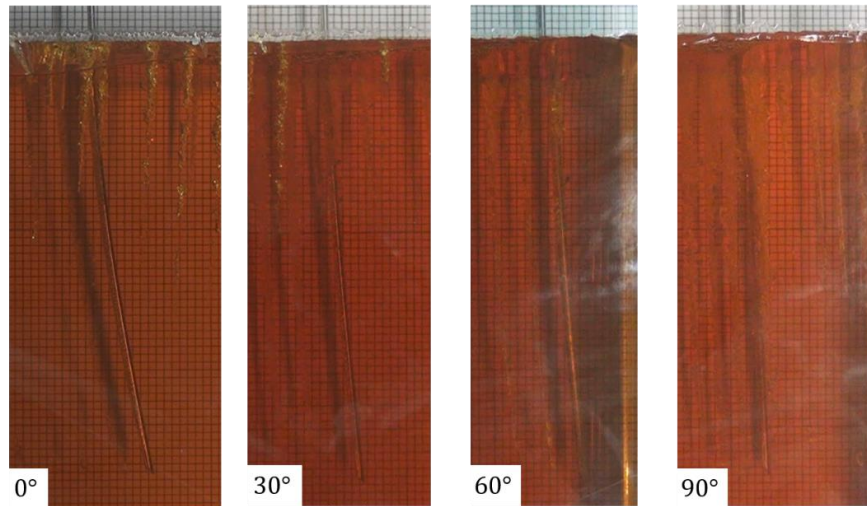


Fig. 4.4. The results of the stiffness-controlled steerable needle's insertion with variable stiffness. The rotational configuration of the inner tube is 0°, 30°, 60°, and 90° to vary the needle's flexural stiffness along its bending direction

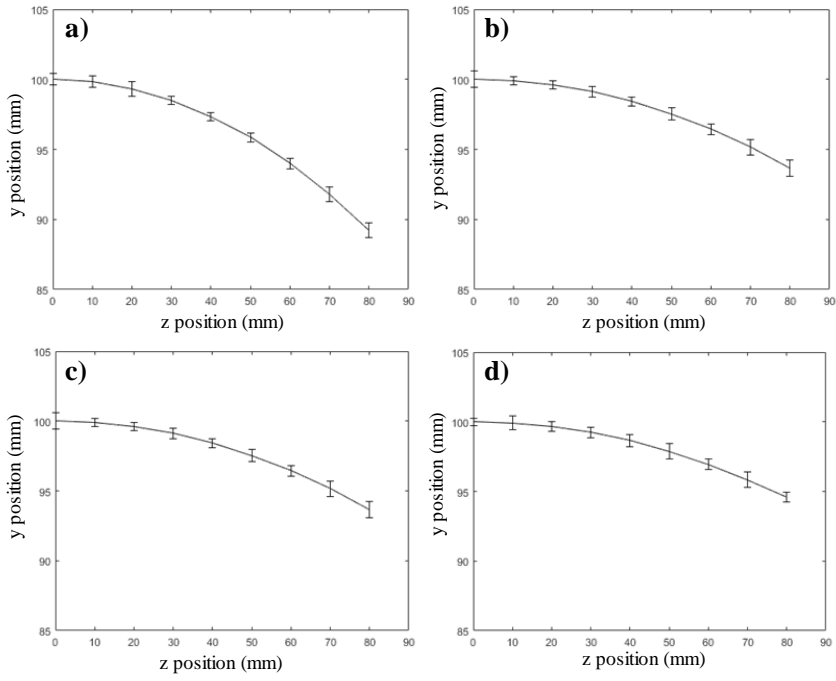


Fig. 4.5. The needle's trajectory from the bi-cycle nonholonomic model and the standard deviation bar of the experimental results when  $\theta_R$  is a)  $0^\circ$ , b)  $30^\circ$ , c)  $60^\circ$ , and d)  $90^\circ$

## 4.4 The Customization on Stiffness and the Range of Variable

### Stiffness

In section 2.1.3 and 3.3, the analytic model for the patterned tube was studied. Using the model, I built an analytic model to design the range of stiffness for the proposed steerable needle. The design parameters are the dimension of the inner and outer tubes (thickness and diameter), material selection of the tubes, and  $\theta_h$  for the pattern of the inner tube.

$$\begin{aligned}
 EI_{steerable\ needle} &= EI_{outer\ tube} + EI_{inner\ tube} \\
 &= E_o \cdot \frac{\pi}{64} (D_o^4 - D_i^4) + E_i \cdot \int_{\frac{d_i}{2}}^{\frac{d_o}{2}} 2 \cdot \int_{\theta_1}^{\theta_1 + (\pi - \theta_h)} (r \sin \theta)^2 r d\theta dr \\
 &= E_o \cdot \frac{\pi}{64} (D_o^4 - D_i^4) + E_i \cdot \frac{d_o^4 - d_i^4}{32} \left[ \pi - \theta_h - \frac{1}{2} (\sin(2\theta_1 + 2\pi - 2\theta_h) - \sin(2\theta_1)) \right] \quad (60)
 \end{aligned}$$

where  $E_o$  and  $E_i$  are the elastic modulus for outer tube and inner tube, respectively;  $D_o$  and  $D_i$  are the outer and inner diameter of outer tube, respectively;  $d_o$  and  $d_i$  are the outer and inner diameter of the inner tube, respectively;  $\theta_h$  is the central angle for the pattern defined in chapter 3;  $\theta_1$  is determined by the rotational configuration of the inner tube.

The outer tube was nitinol ( $E = 51.3\text{ GPa}$ ) having an outer diameter of  $2.0\text{ mm}$  and an inner diameter of  $1.8\text{ mm}$ . The inner tube was stainless steel ( $E = 188\text{ GPa}$ ) having an outer diameter of  $1.65\text{ mm}$  and an inner diameter of  $1.35\text{ mm}$ .



According to the model, the maximum and minimum values of the flexural stiffness of the steerable needle occurred at  $\theta_1 = \frac{\theta_h}{2}$  and at  $\theta_1 = \frac{\theta_h - \pi}{2}$ , respectively, as the inner tube rotated.

$\max (EI_{steerable\ needle})$

$$= E_o \cdot \frac{\pi}{64} (D_o^4 - D_i^4) + E_i \cdot \frac{d_o^4 - d_i^4}{32} [\pi - \theta_h + \sin \theta_h] \quad (61)$$

$\min (EI_{steerable\ needle})$

$$= E_o \cdot \frac{\pi}{64} (D_o^4 - D_i^4) + E_i \cdot \frac{d_o^4 - d_i^4}{32} [\pi - \theta_h - \sin \theta_h] \quad (62)$$

To maximize the ratio  $\frac{EI_{max}}{EI_{min}}$ , 1)  $E_i$  should be larger than  $E_o$ ,  $\maximize(\frac{E_i}{E_o})$ , and 2) the thickness of the inner tube should be larger than that of the outer tube,  $\maximize(\frac{T_i}{T_o})$ , as much as possible. In the experiment, to widen the variable stiffness range,  $E_o$  was chosen as nitinol ( $E = 51.3GPa$ ) while  $E_i$  was chosen as stainless steel ( $E = 188GPa$ ). Therefore, according to its application and constraints, the steerable needle was able to be customized.

Reminding the section 3.4.1, as Misra et al. built the energy-based model formulation [60], [97], the major energy contribution is the summation of the pure bending energy of the needle (32) and the energy due to interaction of the elastic medium along the needle shaft (35). Then, the summation of (32) and (35) is close to the total work done on the system. The reference results indicated that the energy associated with  $U_B$  (32) and  $U_T$  (35) dominate the total potential of the system, and

the energy due to compression and work done due to rupture and tip loads are less significant.

$$\frac{EI}{2} \int_0^{l_i} \left( \frac{d^2 y_i}{dx^2} \right)^2 dx + \frac{1}{2} \int_0^{l_1} K_T (y_1 - y_{c_i})^2 dx \approx P_{input} l_i \quad (63)$$

Note that  $\frac{EI}{2} \int_0^{l_i} \left( \frac{d^2 y_i}{dx^2} \right)^2 dx \gg \frac{1}{2} \int_0^{l_1} K_T (y_1 - y_{c_i})^2 dx$  for  $l_i \in [0mm, 8mm]$  from the results in [60]. Because  $P_{input}$  does not change much when  $l_i$  is short, roughly assume that in the first 8mm, the relationship  $EI \propto \frac{1}{\kappa^2}$  is valid based on that  $U_B$  consists of the most energy of the system. Then, like Fig. 4.6, fitting the results of the rotated angle of  $0^\circ$ ,  $30^\circ$ ,  $60^\circ$ , and  $90^\circ$  from Table 4.1 to have (64).

$$\kappa = (5.00 \cdot 10^3 \cdot EI - 9.08 \cdot 10^3)^{-1/2} \quad (64)$$

$$\begin{aligned} EI &= E_o \cdot \frac{\pi}{64} (D_o^4 - D_i^4) + E_i \cdot \frac{d_o^4 - d_i^4}{32} \left[ \pi - \theta_h - \frac{1}{2} (\sin(2\theta_1 + \pi - 2\theta_h) - \right. \\ &\quad \left. \sin(2\theta_i - \pi)) \right] \\ &= 13.86 + 24.03 [(\pi - 1.22 - 0.5(\sin(2\theta_1 + \pi - 2\theta_h) - \sin(2\theta_i - \pi)))] \quad (65) \end{aligned}$$

Thus,  $\kappa$  can be expressed as the function of  $\theta_i$  like Fig.4.7,

$$\begin{aligned} I &= f(\theta_i) = 13.86 \\ &\quad + 24.03 [(\pi - 1.22 - 0.5(\sin(2\theta_1 + \pi - 2\theta_h) \\ &\quad - \sin(2\theta_i - \pi)))] \quad (66) \end{aligned}$$

$$\kappa = (5.00 \cdot 10^3 \cdot f(\theta_i) - 9.08 \cdot 10^3)^{-1/2} \quad (67)$$

Finally, the inner tube rotational configuration determined the trajectory of the needle. Notice that  $\theta_i$  has the same rotational configuration as  $-\theta_i$  and  $\theta + \pi$ . Thus,  $\theta_i \in [0^\circ, 90^\circ]$  is enough for the whole rotational angle.

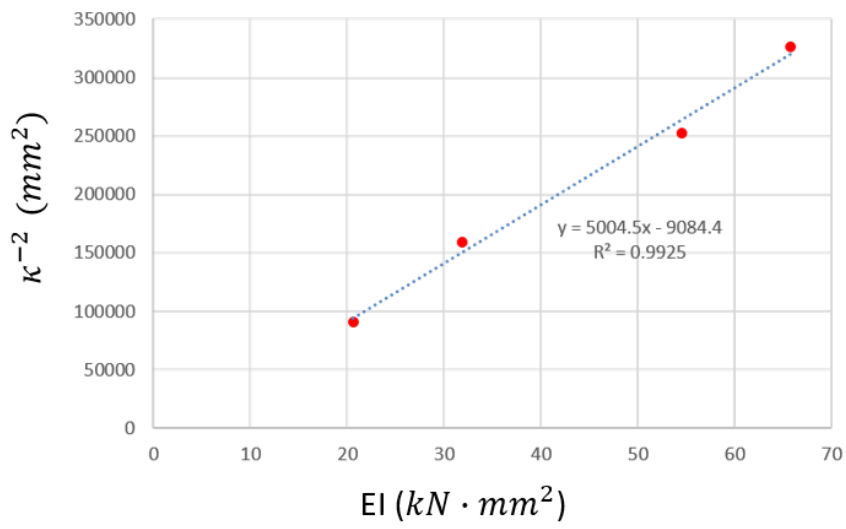


Fig. 4.6. The linearly fitting graph between the needle's flexural stiffness and the reciprocal of the square of the curvature of the needle's trajectory

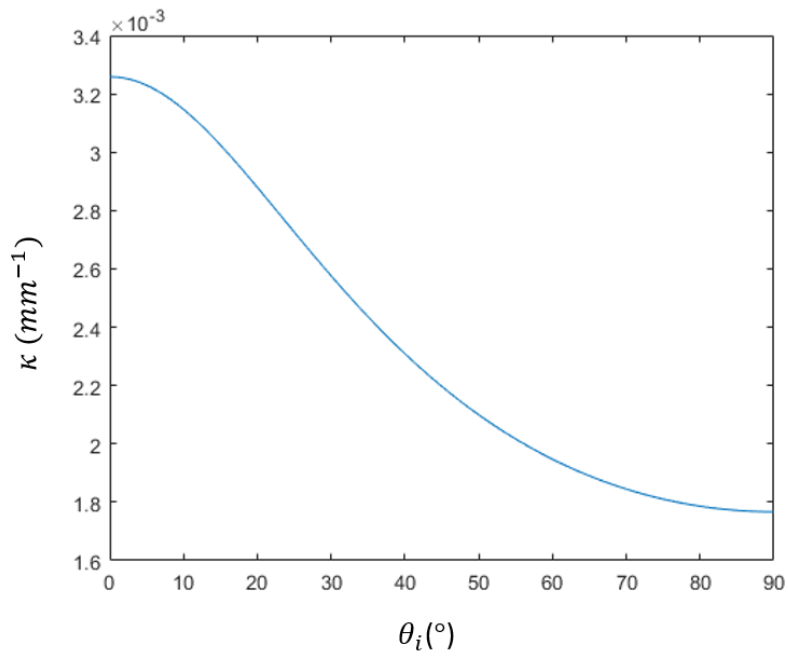


Fig. 4.7. The relationship between the inner tube rotation,  $\theta_i$ , and the curvature of the needle's trajectory,  $\kappa$

## 4.5 Stiffness-controlled Steerable Needle's Applications

The stiffness-controlled steerable needle demonstrates increased safety, wider workspace, minimized invasiveness, and the hollow channel compared to conventional steerable needle.

The proposed steerable needle is possible to keep insertion speed low while having variable curvature trajectory. It avoids high speed that is possible to cause fatal injury to patients. Additionally, changing the insertion speed requires a much longer acceleration time compared to variable stiffness mechanism, resulting in inaccuracy of tip position. Duty cycle method has too much friction against nearby tissue, so the tissue gets damaged easily.

The stiffness change in this mechanism depends only on the inner tube rotation that occurs inside the instrument. It minimizes invasiveness during operation. Other mechanisms using tendon or sheath translating mechanism [98] interacts with nearby tissues when changing its curvature of the trajectory. Table 4.2 compares the benefits of the proposed stiffness-controlled steerable needle over the other methods.

Under the same speed limit, its workspace is much wider compared to the steerable system with two control variables. Fig. 2.14 compares the workspace between the conventional and the proposed steerable needle when the insertion speed is constant. From the plots, the proposed steerable needle demonstrated wider workspace and more capabilities to avoid obstacles with increased dexterity.

Researchers have studied path planning of the steerable needle to avoid obstacles [99]–[102]. Especially, the proposed variable stiffness provides the wider scope of the curvature of the needle's trajectory, so it is expected to ease the difficulties to avoid anatomical obstacles during needle intervention. In Fig. 4.8, the mission was

that the needle addresses the yellow point from the green point without contacting the red zone. The needle cannot reach the green point through a path of constant curvature without passing through the red area. However, the continuously variable stiffness needle was possible to adjust its trajectory shorter while avoiding given obstacles. At first, the needle was inserted by 60mm with  $0^\circ$  of the rotational angle of the inner tube. Secondly, the bevel tip outer tube was rotated for  $180^\circ$  to orient the bending direction. Then, the needle was inserted by 55mm with  $60^\circ$  of the rotated angle of the inner tube. Finally, the distal tip of the needle reached the target without passing the red area. Because the curvature of the needle's trajectory can change continuously, the mechanism has more flexible choices for path planning. Moreover, the proposed variable stiffness mechanism, using physically embodied intelligence, can be combined with other methods [30], [31] if necessary.

During prostate brachytherapy or radiofrequency ablation for liver, the needle should avoid tissues that cannot be cut by the needle, such as bone, or sensitive tissues that should not be damaged, such as nerves or arteries. Based on the motion planning of the stiffness-controlled needle, it can reduce unreachable area during prostate brachytherapy or liver tumor ablation. Additionally, the mechanism has hollow space that can provide a conduit through which to deliver a wide variety of therapies, e.g. drugs, radioactive seeds, and thermal ablation. The further obstacle avoiding test in the in-vitro environment will be studied in future work.

Table 4.2. The comparison of stiffness-controlled needle  
with other steering methods

Method	Description	Safety Issue	etc
Insertion Speed Change [57]	Changing the speed of the needle insertion	High insertion speed	Acceleration zone hinders precise control
Duty Cycle Algorithm [62, 92, 93]	Using much higher rotational speed than insertion speed	Too much friction with nearby tissues	Nearby tissues are easily damaged
Translating Sheath Method [98]	Sheath compensates the degree of bending	Interaction with tissues when translating sheath	Not hollow structure
Stiffness-Controlled Needle	Continuously varying stiffness	Stiffness determined by the inner tube's rotation	Stiffness change happens in microseconds

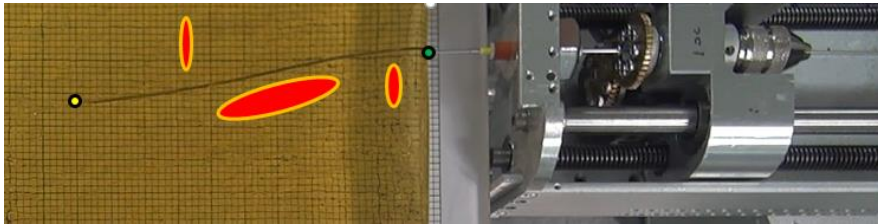


Fig. 4.8. The obstacle avoiding test using continuously stiffness-controlled steerable needle. The needle started from the green circle and approached the yellow circle while avoiding red regions by varying the curvature of the needle's trajectory.



## Chapter 5 Discussion and Conclusion

I presented a mechanism for varying the stiffness of a tubular structure by relative rotation and translation among a set of tubes with anisotropic distribution of the flexural stiffness ( $EI$ ). In the presented mechanism, the anisotropy was created by machining through-hole patterns on selected surfaces of the nitinol tubes. Alternatively, it is able to use localized annealing to induce the phase transition of nitinol from martensite to austenite. In the research, to have bigger difference in flexural stiffness, the variable stiffness is primarily achieved by material removal rather than phase transition.

An analytical model was formulated that describes the change in stiffness as a function of rotation of two coaxial tubes. Also the relationship between the design parameters and the range of stiffness variation was modeled. Using the relationship in (6) ~ (20), design parameters can be selected to adjust the range of stiffness variation according to target applications.

The directional flexural stiffness of the mechanism is a continuous function of relative rotational angle and translational displacements between the tubes. This characteristic is distinguished from other previous variable stiffness mechanisms with binary or discrete stiffness control. The flexural stiffness of the mechanism can be set to any values between the maximum ( $90^\circ, 90^\circ$ ) and the minimum ( $0^\circ, 0^\circ$ ) through the relative rotation between two coaxial tubes. The load test demonstrates the continuously variable stiffness of the mechanism.

Furthermore, the embodied intelligence of the mechanism leads to a simple and scalable structure. The mechanism only consists of two coaxial tubes without any bulky or complex external connections such as pneumatic lines or heating wires.

Therefore, the mechanism is suitable for applications in minimally invasive surgery and can be easily adapted to all types of tube continuum robot. In this study, I was able to reduce the diameter of the mechanism to 1.8mm or less, which is smaller than the current minimally invasive surgical robot generally using 5mm ~ 20mm diameter.

Additionally, unlike other variable stiffness mechanisms using heat, electric, pneumatic stimulus, the response time of the presented mechanism is immediate. The stiffness can be instantly varied by directly translating and rotating the coaxial tubes with motors. Fast response times are very useful in reducing operative time and in responding to immediate surgical conditions and intuitive control of operators.

The proposed mechanism has a relatively narrow range of stiffness variation compared to other mechanisms that utilizes phase change materials such as liquid metals. Also, the baseline of the range starts much higher than that using the phase change materials, so the proposed mechanism aims at surgical tasks that require relatively high stiffness.

The variation of the stiffness predicted from the model was verified through three-point bending experiments and FEM simulation. Overall, the model, the experiment and the simulation showed a consistent tendency of the flexural stiffness change. For type B, the FEM simulation results showed reduced flexural stiffness ratio compared to those of other methods. The FEM simulations demonstrate different results depending on the meshing method, and in terms of simulation, Type B is a more complex structure than Type A because of the increased number of patterns. This leads to the difficulties of contact constraints and meshing and possibly affected the simulation results.

The error between the modeling and experiments is mainly based on the limit of fabrication. Due to its heat affect, the laser cannot engrave the exactly same pattern as its design. Even though we compensated 29 $\mu$ m to obtain more accurate fabrication

results as chapter IV-a, the results still have errors. Because the pattern is micrometric in size, this error is caused by the limitations of the in-house manufacturing process itself. Using more precise machining and systems should reduce the error between theoretical and experimental results. For example, to reduce heat affected zone and to increase precision, pico or femto second UV laser is preferred rather than nano second one. In addition, fine finishing and polytetrafluoroethylene (PTFE) coatings reduce friction among the tubes and between the mechanism and contacting tissues.

In chapter 3, using topology optimization method, the pattern shape is determined to maximize its variable stiffness range. The design parameters are able to be customized according to buckling map and target applications. The design process is built to satisfy the required variable stiffness range and the constraints while avoiding torsional/twist buckling. The ability to vary stiffness of continuum robots expands the design flexibility of surgical instruments. Depending on patient-specific surgical sites, a surgical instrument is possible to use this mechanism to adjust the desired range of variable stiffness.

Using such programmable variable stiffness mechanism, one of the specific potential application is needle steering. The phantom experiment result in this study demonstrated that curvature of a needle insertion trajectory can be changed by varying the stiffness of the needle using the proposed mechanism. As its stiffness varies continuously, the mechanism grants additional degree of freedom (DOF) to the steerable needle system to control the curvature of bending.

Currently, the curvature of the steerable needle is controlled by changing the insertion speed [30] or by intermittent rotation of the needle during insertion [31]. Both methods may create high speed motion of the needle, leading to the damage to nearby tissues. On the other hand, by varying the stiffness, the curvature of the

steerable needle can be controlled while limiting the insertion and rotation speed. Additionally, if the needle consists of a non-patterned outer tube with a bevel tip and a non-uniform patterned inner tube, the flexural stiffness of the needle is determined by the rotational configuration of the inner tube. As the rotation of the inner tube happens inside of the instrument, the mechanism minimizes the interactions with nearby tissues. Thus, the variable stiffness mechanism can be less invasive compared to other mechanisms, increasing the safety. Also, the variable stiffness mechanism can be combined with other methods [30], [31] if necessary.

Since it is possible to vary the curvature of trajectory continuously, the stiffness-controlled steerable needle is expected to avoid obstacles and address deeper in more easiness. It is expected to provide advantages to optimize trajectories to be less traumatic during various applications such as radiofrequency ablation of liver tumors, prostate brachytherapy, etc. The path planning method will be studied to avoid obstacles and the in-vivo or cadaver test will be performed with medical teams.

Furthermore, the variable stiffness mechanism and its stiffness optimization method is expected to be applicable to various needlescopic instruments and enhance their performance. I also plan to apply the mechanism to variable stiffness backbones and combine them with the stiffness control algorithms for continuum robots [103] to develop other surgical instruments in minimally invasive surgery.

## Acknowledgement

The FEM simulation study in chapter 3 was co-worked with Soyeon Park and Gunwoo Noh in Kyungbook University.

## Bibliography

- [1] I. Robert J. Webster, J. S. Kim, N. J. Cowan, G. S. Chirikjian, and A. M. Okamura, “Nonholonomic Modeling of Needle Steering,” *Int. J. Robot. Res.*, vol. 25, no. 5–6, pp. 509–525, May 2006.
- [2] J. Abadie, N. Chaillet, and C. LExcellent, “Modeling of a new SMA micro-actuator for active endoscopy applications,” *Mechatronics*, vol. 19, no. 4, pp. 437–442, 2009.
- [3] T. P. Chenal, J. C. Case, J. Paik, and R. K. Kramer, “Variable stiffness fabrics with embedded shape memory materials for wearable applications,” in *2014 IEEE/RSJ International Conference on Intelligent Robots and Systems*, 2014, pp. 2827–2831.
- [4] J. Kim, D. Y. Lee, S. R. Kim, and K. J. Cho, “A self-deployable origami structure with locking mechanism induced by buckling effect,” in *2015 IEEE International Conference on Robotics and Automation (ICRA)*, 2015, pp. 3166–3171.
- [5] Y. Chen, J. Sun, Y. Liu, and J. Leng, “Variable stiffness property study on shape memory polymer composite tube,” *Smart Mater. Struct.*, vol. 21, no. 9, p. 094021, 2012.
- [6] W. Shan, T. Lu, and C. Majidi, “Soft-matter composites with electrically tunable elastic rigidity,” *Smart Mater. Struct.*, vol. 22, no. 8, p. 085005, Jul. 2013.
- [7] F. Gandhi and S.-G. Kang, “Beams with controllable flexural stiffness,” *Smart Mater. Struct.*, vol. 16, no. 4, pp. 1179–1184, Jun. 2007.
- [8] G. Mcknight, R. Doty, A. Keefe, G. Herrera, and C. Henry, “Segmented Reinforcement Variable Stiffness Materials for Reconfigurable Surfaces,” *J. Intell. Mater. Syst. Struct.*, vol. 21, no. 17, pp. 1783–1793, Nov. 2010.
- [9] Y. Shan *et al.*, “Variable stiffness structures utilizing fluidic flexible matrix composites,” *J. Intell. Mater. Syst. Struct.*, vol. 20, no. 4, pp. 443–456, 2009.

- [10] O. Tabata *et al.*, “Micro fabricated tunable bending stiffness devices,” *Sens. Actuators Phys.*, vol. 89, no. 1–2, pp. 119–123, 2001.
- [11] H. Kim, H. Park, J. Kim, K.-J. Cho, and Y.-L. Park, “Design of anisotropic pneumatic artificial muscles and their applications to soft wearable devices for text neck symptoms,” 2017, pp. 4135–4138.
- [12] Y.-J. Park, T. M. Huh, D. Park, and K.-J. Cho, “Design of a variable-stiffness flapping mechanism for maximizing the thrust of a bio-inspired underwater robot,” *Bioinspir. Biomim.*, vol. 9, no. 3, p. 036002, 2014.
- [13] A. Firouzeh and J. Paik, “Grasp Mode and Compliance Control of an Underactuated Origami Gripper Using Adjustable Stiffness Joints,” *IEEEASME Trans. Mechatron.*, vol. 22, no. 5, pp. 2165–2173, Oct. 2017.
- [14] G. Immega and K. Antonelli, “The KSI tentacle manipulator,” in *Proceedings of 1995 IEEE International Conference on Robotics and Automation*, 1995, vol. 3, pp. 3149–3154 vol.3.
- [15] W. McMahan, B. A. Jones, and I. D. Walker, “Design and implementation of a multi-section continuum robot: Air-Octor,” in *2005 IEEE/RSJ International Conference on Intelligent Robots and Systems*, 2005, pp. 2578–2585.
- [16] A. Stilli, H. A. Wurdemann, and K. Althoefer, “Shrinkable, stiffness-controllable soft manipulator based on a bio-inspired antagonistic actuation principle,” in *2014 IEEE/RSJ International Conference on Intelligent Robots and Systems*, 2014, pp. 2476–2481.
- [17] F. Maghooa, A. Stilli, Y. Noh, K. Althoefer, and H. A. Wurdemann, “Tendon and pressure actuation for a bio-inspired manipulator based on an antagonistic principle,” in *2015 IEEE International Conference on Robotics and Automation (ICRA)*, 2015, pp. 2556–2561.
- [18] Y. J. Kim, S. Cheng, S. Kim, and K. Iagnemma, “A Stiffness-Adjustable Hyperredundant Manipulator Using a Variable Neutral-Line Mechanism for Minimally Invasive Surgery,” *IEEE Trans. Robot.*, vol. 30, no. 2, pp. 382–395, Apr. 2014.
- [19] Y.-J. Kim, S. Cheng, S. Kim, and K. Iagnemma, “A novel layer jamming mechanism with tunable stiffness capability for minimally invasive surgery,” *IEEE Trans. Robot.*, vol. 29, no. 4, pp. 1031–1042, 2013.
- [20] J. L. C. Santiago, I. D. Walker, and I. S. Godage, “Continuum robots for space applications based on layer-jamming scales with stiffening capability,” in *Aerospace Conference, 2015 IEEE*, 2015, pp. 1–13.

- [21] J. Ou, L. Yao, D. Tauber, J. Steimle, R. Niiyama, and H. Ishii, “jamSheets: thin interfaces with tunable stiffness enabled by layer jamming,” in *Tangible and Embedded Interaction*, 2014.
- [22] Y. Kim, S. Cheng, S. Kim, and K. Iagnemma, “Design of a tubular snake-like manipulator with stiffening capability by layer jamming,” in *2012 IEEE/RSJ International Conference on Intelligent Robots and Systems*, 2012, pp. 4251–4256.
- [23] N. G. Cheng *et al.*, “Design and analysis of a robust, low-cost, highly articulated manipulator enabled by jamming of granular media,” in *Robotics and Automation (ICRA), 2012 IEEE International Conference on*, 2012, pp. 4328–4333.
- [24] A. J. Loeve, O. S. van de Ven, J. G. Vogel, P. Breedveld, and J. Dankelman, “Vacuum packed particles as flexible endoscope guides with controllable rigidity,” *Granul. Matter*, vol. 12, no. 6, pp. 543–554, 2010.
- [25] S. Hauser, M. Robertson, A. Ijspeert, and J. Paik, “JammJoint: A Variable Stiffness Device Based on Granular Jamming for Wearable Joint Support,” *IEEE Robot. Autom. Lett.*, vol. 2, no. 2, pp. 849–855, Apr. 2017.
- [26] T. Ranzani, M. Cianchetti, G. Gerboni, I. D. Falco, and A. Menciassi, “A Soft Modular Manipulator for Minimally Invasive Surgery: Design and Characterization of a Single Module,” *IEEE Trans. Robot.*, vol. 32, no. 1, pp. 187–200, Feb. 2016.
- [27] V. Wall, R. Deimel, and O. Brock, “Selective stiffening of soft actuators based on jamming,” in *Robotics and Automation (ICRA), 2015 IEEE International Conference on*, 2015, pp. 252–257.
- [28] Y. Chen, Y. Li, Y. Li, and Y. Wang, “Stiffening of soft robotic actuators—Jamming approaches,” in *Real-time Computing and Robotics (RCAR), 2017 IEEE International Conference on*, 2017, pp. 17–21.
- [29] L. Pournin, M. Tsukahara, and T. M. Liebling, “Particle Shape versus Friction in Granular Jamming,” *AIP Conf. Proc.*, vol. 1145, no. 1, pp. 499–502, Jun. 2009.
- [30] A. Jiang *et al.*, “Robotic Granular Jamming: Does the Membrane Matter?,” *Soft Robot.*, vol. 1, no. 3, pp. 192–201, Jun. 2014.
- [31] A. J. Loeve, O. S. van de Ven, J. G. Vogel, P. Breedveld, and J. Dankelman, “Vacuum packed particles as flexible endoscope guides with controllable rigidity,” *Granul. Matter*, vol. 12, no. 6, pp. 543–554, Dec. 2010.

- [32] J. Zhang, T. S. Majmudar, M. Sperl, and R. P. Behringer, “Jamming for a 2D granular material,” *Soft Matter*, vol. 6, no. 13, pp. 2982–2991, Jun. 2010.
- [33] R. Zhao, Y. Yao, and Y. Luo, “Development of a variable stiffness over tube based on low-melting-point-alloy for endoscopic surgery,” *J. Med. Devices*, vol. 10, no. 2, p. 021002, 2016.
- [34] B. E. Schubert and D. Floreano, “Variable stiffness material based on rigid low-melting-point-alloy microstructures embedded in soft poly (dimethylsiloxane)(PDMS),” *Rsc Adv.*, vol. 3, no. 46, pp. 24671–24679, 2013.
- [35] Rich Steven, Jang Sung-Hwan, Park Yong-Lae, and Majidi Carmel, “Liquid Metal-Conductive Thermoplastic Elastomer Integration for Low-Voltage Stiffness Tuning,” *Adv. Mater. Technol.*, vol. 2, no. 12, p. 1700179, Oct. 2017.
- [36] M. A. McEvoy and N. Correll, “Thermoplastic variable stiffness composites with embedded, networked sensing, actuation, and control,” *J. Compos. Mater.*, vol. 49, no. 15, pp. 1799–1808, Jun. 2015.
- [37] J. D. Carlson and M. R. Jolly, “MR fluid, foam and elastomer devices,” *Mechatronics*, vol. 10, no. 4, pp. 555–569, Jun. 2000.
- [38] Y. Li, J. Li, W. Li, and H. Du, “A state-of-the-art review on magnetorheological elastomer devices,” *Smart Mater. Struct.*, vol. 23, no. 12, p. 123001, Nov. 2014.
- [39] Y. Li, J. Li, T. Tian, and W. Li, “A highly adjustable magnetorheological elastomer base isolator for applications of real-time adaptive control,” *Smart Mater. Struct.*, vol. 22, no. 9, p. 095020, Aug. 2013.
- [40] G. Y. Zhou and Q. Wang, “Study on the adjustable rigidity of magnetorheological-elastomer-based sandwich beams,” *Smart Mater. Struct.*, vol. 15, no. 1, pp. 59–74, Dec. 2005.
- [41] Z. G. Ying and Y. Q. Ni, “Micro-vibration response of a stochastically excited sandwich beam with a magnetorheological elastomer core and mass,” *Smart Mater. Struct.*, vol. 18, no. 9, p. 095005, Sep. 2009.
- [42] V. Lara-Prieto, R. Parkin, M. Jackson, V. Silberschmidt, and Z. Kęsy, “Vibration characteristics of MR cantilever sandwich beams: experimental study,” *Smart Mater. Struct.*, vol. 19, no. 1, p. 015005, Jan. 2010.
- [43] A. Balasubramanian, M. Standish, and C. J. Bettinger, “Microfluidic Thermally Activated Materials for Rapid Control of Macroscopic Compliance,” *Adv. Funct. Mater.*, vol. 24, no. 30, pp. 4860–4866, 2014.



- [44] J. R. Capadona, K. Shanmuganathan, D. J. Tyler, S. J. Rowan, and C. Weder, “Stimuli-responsive polymer nanocomposites inspired by the sea cucumber dermis,” *Science*, vol. 319, no. 5868, pp. 1370–1374, Mar. 2008.
- [45] H. Dong and G. M. Walker, “Adjustable stiffness tubes via thermal modulation of a low melting point polymer,” *Smart Mater. Struct.*, vol. 21, no. 4, p. 042001, 2012.
- [46] A. Orita and M. R. Cutkosky, “Scalable Electroactive Polymer for Variable Stiffness Suspensions,” *IEEEASME Trans. Mechatron.*, vol. 21, no. 6, pp. 2836–2846, Dec. 2016.
- [47] N. Herzig, P. Maiolino, F. Iida, and T. Nanayakkara, “A Variable Stiffness Robotic Probe for Soft Tissue Palpation,” *IEEE Robot. Autom. Lett.*, vol. 3, no. 2, pp. 1168–1175, 2018.
- [48] J. Kim, C. Kim, S. Kang, and K.-J. Cho, “A novel variable stiffness mechanism for minimally invasive surgery using concentric anisotropic tube structure,” in *Hamlyn Symposium on Medical Robotics*, 2017, pp. 43–44.
- [49] T. Duerig, D. Stoeckel, and D. Johnson, “SMA: smart materials for medical applications,” in *European Workshop on Smart Structures in Engineering and Technology*, 2003, vol. 4763, pp. 7–16.
- [50] J.-S. Kim, D.-Y. Lee, K. Kim, S. Kang, and K.-J. Cho, “Toward a solution to the snapping problem in a concentric-tube continuum robot: Grooved tubes with anisotropy,” in *Robotics and Automation (ICRA), 2014 IEEE International Conference on*, 2014, pp. 5871–5876.
- [51] D.-Y. Lee *et al.*, “Anisotropic patterning to reduce instability of concentric-tube robots,” *IEEE Trans. Robot.*, vol. 31, no. 6, pp. 1311–1323, 2015.
- [52] P. Zhu, L. C. Brinson, E. Peraza-Hernandez, D. Hartl, and A. Stebner, “Comparison of three-dimensional shape memory alloy constitutive models: finite element analysis of actuation and superelastic responses of a shape memory alloy tube,” in *ASME 2013 Conference on Smart Materials, Adaptive Structures and Intelligent Systems*, 2013, p. V002T02A004–V002T02A004.
- [53] H. Huang, H. Y. Zheng, and G. C. Lim, “Femtosecond laser machining characteristics of Nitinol,” *Appl. Surf. Sci.*, vol. 228, no. 1–4, pp. 201–206, 2004.
- [54] A. K. Dubey and V. Yadava, “Experimental study of Nd: YAG laser beam machining—An overview,” *J. Mater. Process. Technol.*, vol. 195, no. 1–3, pp. 15–26, 2008.

- [55] N. J. van de Berg, D. J. van Gerwen, J. Dankelman, and J. J. van den Dobbelsteen, "Design Choices in Needle Steering—A Review," *IEEE/ASME Trans. Mechatron.*, vol. 20, no. 5, pp. 2172–2183, Oct. 2015.
- [56] R. J. Webster, J. Memisevic, and A. M. Okamura, "Design Considerations for Robotic Needle Steering," in *Proceedings of the 2005 IEEE International Conference on Robotics and Automation*, 2005, pp. 3588–3594.
- [57] P. Moreira, S. Patil, R. Alterovitz, and S. Misra, "Needle Steering in Biological Tissue using Ultrasound-based Online Curvature Estimation," *IEEE Int. Conf. Robot. Autom. ICRA Proc. IEEE Int. Conf. Robot. Autom.*, vol. 2014, pp. 4368–4373, 2014.
- [58] A. Majewicz, J. J. Siegel, A. A. Stanley, and A. M. Okamura, "Design and evaluation of duty-cycling steering algorithms for robotically-driven steerable needles," in *2014 IEEE International Conference on Robotics and Automation (ICRA)*, 2014, pp. 5883–5888.
- [59] "Design of multiphysics actuators using topology optimization – Part II: Two-material structures - ScienceDirect." [Online]. Available: <https://www.sciencedirect.com/science/article/pii/S0045782501002523> . [Accessed: 30-Jan-2019].
- [60] S. Misra, K. B. Reed, B. W. Schafer, K. T. Ramesh, and A. M. Okamura, "Observations and models for needle-tissue interactions," in *2009 IEEE International Conference on Robotics and Automation*, 2009, pp. 2687–2692.
- [61] S. Misra, K. B. Reed, B. W. Schafer, K. T. Ramesh, and A. M. Okamura, "Mechanics of Flexible Needles Robotically Steered through Soft Tissue," *Int. J. Robot. Res.*, vol. 29, no. 13, pp. 1640–1660, Nov. 2010.
- [62] D. Minhas, J. A. Engh, and C. N. Riviere, "Testing of neurosurgical needle steering via duty-cycled spinning in brain tissue in vitro," in *2009 Annual International Conference of the IEEE Engineering in Medicine and Biology Society*, Minneapolis, MN, 2009, pp. 258–261.
- [63] K. B. Reed, A. M. Okamura, and N. J. Cowan, "Modeling and Control of Needles with Torsional Friction," *IEEE Trans. Biomed. Eng.*, vol. 56, no. 12, pp. 2905–2916, Dec. 2009.
- [64] M. Amjadi, K.-U. Kyung, I. Park, and M. Sitti, "Stretchable, Skin-Mountable, and Wearable Strain Sensors and Their Potential Applications: A Review," *Adv. Funct. Mater.*, vol. 26, no. 11, pp. 1678–1698, 2016.

- [65] W. Bogdanich, "At V.A. Hospital, a Rogue Cancer Unit," *The New York Times*, 20-Jun-2009.
- [66] R. C. Susil *et al.*, "Transrectal Prostate Biopsy and Fiducial Marker Placement in a Standard 1.5T Magnetic Resonance Imaging Scanner," *J. Urol.*, vol. 175, no. 1, pp. 113–120, Jan. 2006.
- [67] A. Krieger *et al.*, "Design of a novel MRI compatible manipulator for image guided prostate interventions," *IEEE Trans. Biomed. Eng.*, vol. 52, no. 2, pp. 306–313, Feb. 2005.
- [68] G. Fichtinger *et al.*, "Robotic assistance for ultrasound-guided prostate brachytherapy," *Med. Image Anal.*, vol. 12, no. 5, pp. 535–545, Oct. 2008.
- [69] S. H. Okazawa, R. Ebrahimi, J. Chuang, R. N. Rohling, and S. E. Salcudean, "Methods for segmenting curved needles in ultrasound images," *Med. Image Anal.*, vol. 10, no. 3, pp. 330–342, Jun. 2006.
- [70] S. Cheung and R. Rohling, "Enhancement of needle visibility in ultrasound-guided percutaneous procedures," *Ultrasound Med. Biol.*, vol. 30, no. 5, pp. 617–624, May 2004.
- [71] M. Ding and A. Fenster, "A real-time biopsy needle segmentation technique using Hough transform," *Med. Phys.*, vol. 30, no. 8, pp. 2222–2233, Aug. 2003.
- [72] P. C. Mozer, A. W. Partin, and D. Stoianovici, "Robotic Image-Guided Needle Interventions of the Prostate," *Rev. Urol.*, vol. 11, no. 1, pp. 7–15, 2009.
- [73] N. Abolhassani and R. V. Patel, "Deflection of a flexible needle during insertion into soft tissue," *Conf. Proc. Annu. Int. Conf. IEEE Eng. Med. Biol. Soc. IEEE Eng. Med. Biol. Soc. Annu. Conf.*, vol. 1, pp. 3858–3861, 2006.
- [74] S. P. DiMaio and S. E. Salcudean, "Needle steering and motion planning in soft tissues," *IEEE Trans. Biomed. Eng.*, vol. 52, no. 6, pp. 965–974, Jun. 2005.
- [75] J. A. Engh, G. Podnar, S. Y. Khoo, and C. N. Riviere, "Flexible Needle Steering System for Percutaneous Access to Deep Zones of the Brain," in *Proceedings of the IEEE 32nd Annual Northeast Bioengineering Conference*, 2006, pp. 103–104.
- [76] D. Glozman and M. Shoham, "Image-Guided Robotic Flexible Needle Steering," *IEEE Trans. Robot.*, vol. 23, no. 3, pp. 459–467, Jun. 2007.
- [77] S. Okazawa, R. Ebrahimi, J. Chuang, S. E. Salcudean, and R. Rohling, "Hand-Held Steerable Needle Device," *IEEEASME Trans. Mechatron.*, vol. 10, no. 3, pp. 285–296, Jun. 2005.

- [78] P. Sears and P. Dupont, "A Steerable Needle Technology Using Curved Concentric Tubes," in *2006 IEEE/RSJ International Conference on Intelligent Robots and Systems*, 2006, pp. 2850–2856.
- [79] K. B. Reed, V. Kallem, R. Alterovitz, K. Goldberg, A. M. Okamura, and N. J. Cowan, "Integrated Planning and Image-Guided Control for Planar Needle Steering," *Proc. IEEE/RS-EMBS Int. Conf. Biomed. Robot. Biomechatronics IEEE/RS-EMBS Int. Conf. Biomed. Robot. Biomechatronics*, vol. 2008, pp. 819–824, Oct. 2008.
- [80] J. A. Engh, G. Podnar, D. Kondziolka, and C. N. Riviere, "Toward effective needle steering in brain tissue," *Conf. Proc. Annu. Int. Conf. IEEE Eng. Med. Biol. Soc. IEEE Eng. Med. Biol. Soc. Annu. Conf.*, vol. 1, pp. 559–562, 2006.
- [81] V. G. Mallapragada, N. Sarkar, and T. K. Podder, "Robot-Assisted Real-Time Tumor Manipulation for Breast Biopsy," *IEEE Trans. Robot.*, vol. 25, no. 2, pp. 316–324, Apr. 2009.
- [82] M. Torabi, K. Hauser, R. Alterovitz, V. Duindam, and K. Goldberg, "Guiding medical needles using single-point tissue manipulation," in *2009 IEEE International Conference on Robotics and Automation*, 2009, pp. 2705–2710.
- [83] H.- Nienhuys and A. F. van der Stappen, "A computational technique for interactive needle insertions in 3D nonlinear material," in *IEEE International Conference on Robotics and Automation, 2004. Proceedings. ICRA '04. 2004*, 2004, vol. 2, pp. 2061–2067 Vol.2.
- [84] S. P. DiMaio and S. E. Salcudean, "Needle insertion modeling and simulation," *IEEE Trans. Robot. Autom.*, vol. 19, no. 5, pp. 864–875, Oct. 2003.
- [85] R. Alterovitz, K. Goldberg, J. Pouliot, R. Taschereau, and I-Chow Hsu, "Needle insertion and radioactive seed implantation in human tissues: simulation and sensitivity analysis," in *2003 IEEE International Conference on Robotics and Automation (Cat. No.03CH37422)*, Taipei, Taiwan, 2003, pp. 1793–1799.
- [86] J. R. Crouch, C. M. Schneider, J. Wainer, and A. M. Okamura, "A Velocity-Dependent Model for Needle Insertion in Soft Tissue," in *Medical Image Computing and Computer-Assisted Intervention – MICCAI 2005*, 2005, pp. 624–632.
- [87] M. Heverly, P. Dupont, and J. Friedman, "Trajectory Optimization for Dynamic Needle Insertion," in *Proceedings of the 2005 IEEE International Conference on Robotics and Automation*, 2005, pp. 1646–1651.

- [88] J. T. Hing, A. D. Brooks, and J. P. Desai, "Reality-based needle insertion simulation for haptic feedback in prostate brachytherapy," in *Proceedings 2006 IEEE International Conference on Robotics and Automation, 2006. ICRA 2006.*, 2006, pp. 619–624.
- [89] S. Misra, K. T. Ramesh, and A. M. Okamura, "Modeling of Tool-Tissue Interactions for Computer-Based Surgical Simulation: A Literature Review," *Presence Camb. Mass*, vol. 17, no. 5, p. 463, Oct. 2008.
- [90] H. Kataoka, T. Washio, K. Chinzei, K. Mizuhara, C. Simone, and A. M. Okamura, "Measurement of the Tip and Friction Force Acting on a Needle during Penetration," in *Medical Image Computing and Computer-Assisted Intervention — MICCAI 2002*, 2002, pp. 216–223.
- [91] A. M. Okamura, C. Simone, and M. D. O’Leary, "Force Modeling for Needle Insertion Into Soft Tissue," *IEEE Trans. Biomed. Eng.*, vol. 51, no. 10, pp. 1707–1716, Oct. 2004.
- [92] D. S. Minhas, J. A. Engh, M. M. Fenske, and C. N. Riviere, "Modeling of Needle Steering via Duty-Cycled Spinning," in *2007 29th Annual International Conference of the IEEE Engineering in Medicine and Biology Society*, 2007, pp. 2756–2759.
- [93] M. C. Bernardes, B. V. Adorno, P. Poignet, N. Zemititi, and G. A. Borges, "Path planning for steerable needles using duty-cycled spinning," *BIO Web Conf.*, vol. 1, p. 00010, 2011.
- [94] I. V. Laguta, O. N. Stavinskaya, P. A. Kuzema, O. A. Kazakova, and D. B. Nasedkin, "Hybrid materials on the basis of gelatin and hydrophilic–hydrophobic silica," *Prot. Met. Phys. Chem. Surf.*, vol. 53, no. 5, pp. 807–811, Sep. 2017.
- [95] W. Park, J. S. Kim, Y. Zhou, N. J. Cowan, A. M. Okamura, and G. S. Chirikjian, "Diffusion-Based Motion Planning for a Nonholonomic Flexible Needle Model," in *Proceedings of the 2005 IEEE International Conference on Robotics and Automation*, 2005, pp. 4600–4605.
- [96] W. Park, Y. Liu, Y. Zhou, M. Moses, and G. S. Chirikjian, "Kinematic state estimation and motion planning for stochastic nonholonomic systems using the exponential map," *Robotica*, vol. 26, pp. 419–434, Apr. 2008.
- [97] S. Misra, K. B. Reed, A. S. Douglas, K. T. Ramesh, and A. M. Okamura, "Needle-tissue interaction forces for bevel-tip steerable needles," in *2008 2nd IEEE RAS & EMBS International Conference on Biomedical Robotics and Biomechatronics*, Scottsdale, AZ, USA, 2008, pp. 224–231.

- [98] V. K. Bui, S. Park, J.-O. Park, and S. Y. Ko, "A novel curvature-controllable steerable needle for percutaneous intervention," *Proc. Inst. Mech. Eng. [H]*, vol. 230, no. 8, pp. 727–738, Aug. 2016.
- [99] M. C. Bernardes, B. V. Adorno, P. Pognet, N. Zemiti, and G. A. Borges, "Adaptive path planning for steerable needles using duty-cycling," in *2011 IEEE/RSJ International Conference on Intelligent Robots and Systems*, 2011, pp. 2545–2550.
- [100] S. Patil and R. Alterovitz, "Interactive Motion Planning for Steerable Needles in 3D Environments with Obstacles," *Proc. IEEE/RSJ-EMBS Int. Conf. Biomed. Robot. Biomechatronics IEEE/RSJ-EMBS Int. Conf. Biomed. Robot. Biomechatronics*, pp. 893–899, 2010.
- [101] M. Khadem, C. Rossa, N. Usmani, R. S. Sloboda, and M. Tavakoli, "Robotic-Assisted Needle Steering Around Anatomical Obstacles Using Notched Steerable Needles," *IEEE J. Biomed. Health Inform.*, vol. 22, no. 6, pp. 1917–1928, Nov. 2018.
- [102] Jijie Xu, V. Duindam, R. Alterovitz, and K. Goldberg, "Motion planning for steerable needles in 3D environments with obstacles using rapidly-exploring Random Trees and backchaining," in *2008 IEEE International Conference on Automation Science and Engineering*, Arlington, VA, 2008, pp. 41–46.
- [103] M. Mahvash and P. E. Dupont, "Stiffness Control of Surgical Continuum Manipulators," *IEEE Trans. Robot.*, vol. 27, no. 2, pp. 334–345, Apr. 2011.

## 초 록

로봇 수술은 보다 정밀한 제어가 가능하며 도달 할 수 없는 영역을 줄일 수 있다. 특히 da Vinci 로봇의 도입 이후로 로봇을 활용한 최소침습수술은 보다 작은 절개를 활용함으로 전통적인 개방 수술에 비해 회복시간이 짧고 감염 위험이 적어 점점 널리 사용되고 있다. 이와 같은 최소침습수술에서 연속체 로봇은 소형화가 가능하여 널리 사용되지만 직경 3mm 이하의 환경에서는 모멘트 암이 작고 적합한 마이크로 액추에이터를 활용하기 어려워 연속체 로봇의 움직임을 제어하는 것이 어려워진다. 이처럼 공간이 제한되고 인접 조직과의 상호 작용이 있는 인체내부의 환경에서는 연속체 로봇의 강성을 조절함으로서 연속체 로봇의 움직임을 제어할 수 있다.

본 논문에서는 연속체 로봇을 위한 연속적인 가변 강성 메커니즘을 제안한다. 메커니즘은 여러 개의 동축으로 조립된 니티놀 또는 스테인리스강으로 이루어진 튜브들로 구성되며, 각 튜브는 비등방성 패터닝으로 생성된 굽힘강성의 비등방성 분포를 가지고 있다. 메커니즘의 강성은 튜브의 상대적 병렬 및 회전운동에 따라 달라지며, 하중 방향으로 최대 7.2 배 및 그 이상의 굴곡 강성 차이가 가능하다. 주축들에 대한 굴곡 강성들은 각각 독립적으로 제어 가능하며, 강성 변화는 해석 모델링, FEM 시뮬레이션 및 실험을 통해 검증 되었다. Physically embodied intelligence를 적용하여 메커니즘은 소형화 하기 쉽고, 모터로 회전을 제어하므로 즉각적인 응답시간을 갖는다.

위상최적화 방법을 통하여 가변강성 비율을 최대로 갖는 패턴의 형상 최적화를 연구하였으며, 가변강성의 정도와 범위에 대한 매개변수 연구를 수행하였다. 또한, 구부림 및 비틀림 좌굴 조건을 분석하여 좌굴을 방지하기 위한 패턴 디자인을 설계 가능하다.

본 가변강성 메커니즘을 스티어링 바늘에 적용하여, 강성을 변화 시키면서 바늘의 궤적을 제어 할 수 있도록 만들었다. 바늘의 강성 변화는 기존의 제어 변수인 삽입 및 회전 속도 외로 추가적인 자유도를 부여한다. 강성 변화에 따른 궤적의 곡률변화에 대해서 bi-cycle nonholonomic 운동학적 모델을 세워 장애물 회피를 위한 실험에 적용하였다. 강성 변화가 가능한 스티어링 바늘은 바늘의 삽입 및 회전 속도를 낮게 유지하면서 궤적의 곡률 변화가 가능하여 안전성이 높으며 현존의 스티어링 바늘들과 비교하여 도달 할 수 없는 영역이 줄어들었고 침습성이 감소 되었다. 또한, 튜브의 형태로서 빈 공간을 통하여 약물, 방사성 seeds 및 ablation 기구 등을 활용 가능하다. 특히 전립선 brachytherapy 또는 간 및 폐에 위치한 종양 조직 제거에 활용할 수 있다. 더불어, 본 메커니즘은 다양한 연속체 로봇에 적용되어 최소침습수술 로봇을 비롯한 미세한 로봇들에 활용될 수 있으리라 예상한다.

**주요어 :** 가변강성구조, 비등방성 패터닝, 조향가능바늘, 최소침습수술, physically embodied intelligence, 의료로봇과 시스템.

**학 번 :** 2013-20659